



**University of
Nottingham**

UK | CHINA | MALAYSIA

Design and Construction of An Optomechanical Coupler For Quantum Optical Experiments

Hayat Abbas

Thesis submitted to the University of Nottingham
for the degree of Doctor of Philosophy

January 2023

*“Our greatest glory is not in never falling, but in
rising every time we fall”*

-Confucius

Abstract

Hybrid quantum systems have received significant interest, especially with the goal of technological exploitation of complementary capabilities for quantum information processing and communication tasks. Quantum transducers can be used to couple the properties of one object or system to different properties of another system, thus combining, for example, the robust transmission of photonic quantum states with strong interactions between material quantum objects. In a room-temperature environment, a spin-polarized atomic ensemble and a micromechanical oscillator over a one-meter distance are coupled to a free-space laser beam. This experiment requires a stable interferometer, which is usually done actively. Stabilizing a large path separation interferometer is cumbersome. Thus, we investigate an alternative way to build a robust polarization interferometer characterised by its stability with no requirement for any adjustment. This thesis constructs a hybrid quantum system consisting of a quantum transducer that maps small position changes of a micro-mechanical membrane onto the polarization of a laser beam. This is done with an interferometric setup that has reduced the need for stabilization. Specifically, an oscillating silicon nitride membrane placed in the middle of an asymmetric optical cavity causes phase shifts in the reflected, near-resonant light field. A beam displacer is used to combine the signal beam with a mode-matched, orthogonally polarized reference beam for polarization encoding. Subsequent balanced homodyne measurement is used to detect thermal membrane noise. The high signal-to-noise ratio should allow for detecting motional quantum noise in the regime of high optomechanical coupling strength. This setup can provide a robust quantum link between a micro-mechanical oscillator and other systems such as atomic ensembles.

Acknowledgements

Words cannot express my gratitude to my supervisor Thomas Fernholz for his invaluable patience and feedback. I could not have undertaken this journey without my cohort members, who generously provided knowledge and expertise. Special thanks to Vilius Atkocius whose patience and professionalism inspire me. Many thanks to Bethany Foxon who was so generous with her time in helping me in the lab and reading my thesis. Thanks should also go to Fabio Gentile, Elisa da Ros, Jamie Johnson, Tadas Pyragius, Rhys Morrison, and Joshua New. I'd also like to thank the whole cold atom group, for being so supportive and always willing to help, and for making my time at Nottingham such a pleasure.

I would like to extend my sincere thanks to Andrew Kenton and Andrew Solomon for their manufacture of my cavity holder design in the workshop.

I would like to express my most profound appreciation to my husband Ghazi Redai whose love and support I daily take for granted through this long journey. Many thanks to my little angels Anmar and Lana for being around me and giving me lovely moments.

Lastly, I would be remiss in not mentioning my family, especially my parents, sisters, and brother. Their belief in me has kept my spirits and motivation high during this process. I would also like to thank you for all the entertainment and emotional support.

List of Publications

1. An Interferometrically Robust Opto-Mechanical Coupler to Beam Polarisation (Submitted on 11 Jan 2023 by Hayat Abbas and Thomas Fernholz)

List of Abbreviations

MIM	Membrane in the middle
RTM	Ray transfer matrix
FSR	Free spectral range
FWHM	Full width at half maximum
BHD	Balanced homodyne detection
PDH	Pound Drever Hall
PZT	Piezoelectric actuator
HWP	Half waveplate
QWP	Quarter waveplate
BPD	Balanced Photo-detector
PD	Photo-detector
BPD	Balanced photodetector
LO	Local oscillator
EOM	Electro-optical modulator
PID	Proportional–integral–derivative controller
LPF	Low pass filter

List of symbols

c	Speed of the light ($3 \times 10^8 m/s$)
λ	Wavelength of laser
ω	Beam waist
R	Radius of curvature of the mirror
q	Complex radius of curvature of the mirror
z_R	Rayleigh range
$\phi(z)$	Gouy phase
ω_0	Minimum beam waist at $z = 0$
θ	Divergence of the laser beam
f_n	Focal length of the n_{th} lens
L_{cavity}	Length of the cavity
g_1, g_2	Cavity stability parameters
k	Wavenumber
ε	The distance between the signal and reference beams
δ	The displacement along the optic axis between the optical cavity and laser waists
α	The angle between the direction of the laser and the cavity's optic axis
\mathcal{F}	Finesses
δ	Phase shift of light in the cavity
r	Reflectivity of the mirror

κ	linewidth of the peak
Q	Quality factor
f	Laser frequency
ω	The angular frequency of the laser
x_m	Displacement of the membrane
Δx_m	The position of the membrane with respect to the centre of the cavity
ω_m	Mechanical resonance frequency in angular unit
M	The effective mass of the membrane
γ_m	The energy damping rate of the oscillator
\mathcal{T}	Tensile stress
f_m	Frequency of membrane
ρ_m	Density of the membrane
d_m	Thickness of the membrane
l_m	Membrane length($l_m \times l_m$)
c_m	Speed of the wave in the membrane
k_B	Boltzmann constant($1.38 \times 10^{-23} m^2 kgs^{-2} K^{-1}$)
T_{bath}	Thermal bath
r_m	Amplitude membrane reflection
t_m	Amplitude membrane transmission
ω_{cav}	The cavity resonance frequency
x_{zp}	Ground state amplitude
ω_{ij}	The membrane frequency for i,j modes
$\hat{a}^\dagger \hat{a}$	Annihilation and creation operator for the light
$\hat{b}^\dagger \hat{b}$	Annihilation and creation operator for the membrane
G	Cavity frequency shift per mechanical displacement
g	Single photon optomechanical coupling
ε_{LO}	The amplitude of the LO beam
ε_S	The amplitude of the signal beam
ϕ_{LO}	The phase of the LO beam
Z_n	The reflection coefficients for the n_{th} element

Δk	Wavenumber difference
Δz	Interference spacing
d	Displacement to the lens
$\alpha_{material}$	Thermal expansion coefficient of the material
ΔT	Temperature difference
L_i	Initial length of the material
$\Delta\phi$	Signal relative phase
ϕ_0	Phase offset
E_i	Incident electric field
E_r	Reflected electric field
r_c	Reflection coefficient amplitude
Ω	Modulation frequency
J_0, J_1	Bessel function
P_s	Power of the sidebands
P_c	Power of the carrier
P_0	Total power
P_r	Power of the reflected beam
τ	Time delay
ϵ	Error signal
n_m	The refractive index of the membrane
r_m	The membrane reflectivity
V_c	Applied voltage to PZT of the cavity
V'_c	Output voltage of PZT of the cavity
G_c	Gain of PZT of the cavity
V_m	Applied voltage to PZT of the membrane
V'_m	Output voltage of PZT of the membrane
G_m	Gain of PZT of the membrane
$\Delta V'_c$	Free spectral range in volt unit

α_c	Cavity PZT expansion coefficient
α_m	Membrane PZT expansion coefficient
$\Delta V'_m$	The difference between the maximum and minimum resonance in volt
σ_f	Frequency sensitivity
σ_x	Position sensitivity
σ_{fm}	Thermal variance
G_e	Electronic gain
η_d	Quantum efficiency
r_d	Detector responsivity
e	Electron charge(1.6×10^{-19} C)

Contents

Abstract	i
Acknowledgements	ii
List of Publications	iii
List of Abbreviations	iv
List of symbols	v
1 Introduction	1
1.1 This Work	4
1.2 Thesis Outline	5
2 Theoretical model of the optomechanical system	7
2.1 Basics of the Optical Cavity	8
2.1.1 Paraxial Wave Equation and Gaussian beams	8
2.1.2 ABCD Matrices and Beam Propagation	14
2.1.3 Types of Optical Cavities and Their Stability	16
2.1.4 Fabry-Perot Cavity and its Properties	17
2.1.5 Coupling Laser Beam to the Optical Cavity	22

2.2	Mechanical Oscillator	27
2.2.1	Mode Function of Mechanical Oscillator	27
2.2.2	The Driven Damped Oscillator	31
2.2.3	Quantum Mechanical Harmonic Oscillator	34
2.3	Optomechanics System with Membrane	36
2.3.1	Basic Theory of Optomechanics system	36
2.3.2	Optomechanical Interaction Hamilton	37
2.4	Membrane in Asymmetric Optical Cavity	39
2.5	Polarization States of the Light	48
2.6	Quantum noise	51
2.6.1	Homodyne detection and quantum noise of light	51
2.6.2	Noise Readout From the Polarization Converter	55
3	A Position to Polarization Converter	60
3.1	Polarization In A Birefringent Crystal	60
3.2	Design of A Position to Polarization Converter	62
3.3	Beam Alignment and Mode Overlap	63
4	Opto-Mechanical Setup	70
4.1	Designing A Thermally Stable Cavity Holder	70
4.2	Membrane Holder Design	73
4.3	Vacuum System	74

4.4	Experimental Setup	75
4.4.1	Mode Matching and Cavity Considerations	77
4.4.2	Polarimetric measurement and phase adjustment	78
4.5	Theory of Pound Drever Hall Locking System	82
4.5.1	Locking Scheme	86
4.6	Theory of Feedback	88
4.6.1	Feedback For Noise Suppression	90
5	Measurement	94
5.1	Characterization of MIM optical Cavity	94
5.2	Characterization Of the Membrane	97
5.3	Calibration of the Cavity and Membrane PZTs	98
5.4	Estimating the Position Sensitivity	101
5.5	Finesses of the optomechanical system	103
5.6	Mechanical Motion of the Membrane	106
5.7	Noise Measurements	107
5.7.1	Measuring Photon Shot Noise	107
5.7.2	Measuring the Thermal Noise of the Membrane	110
5.8	Discussion of laser noise and improvement with filter cavity	115
6	Conclusion and future work	117
	Bibliography	119

Appendices	124
A Mathematical Tools	124
A.1 Fast Fourier Transformation	124
B Assembly Drawing of the Membrane Holder	126
C Schematic Of Fast PID Card	131
D Electronic circuits	132
D.1 Bias-T	132
D.2 Low Pass Filter	133

List of Tables

4.1	Electronics of locking system.	87
5.1	Frequency of the membrane for different mode numbers (i, j). .	106

List of Figures

1.1	Construction of hybrid system with a robust polarization interferometer. It shows light-membrane coupling via an optical cavity and the input beam interferes with the reference beam. QWP represents a quarter wave plate.	4
2.1	A Gaussian beam variation of the beam size $w(z)$ as a function of the distance z along the beam, which forms a hyperbola. . . .	11
2.2	A Gaussian beam matches the radii of curvature of the optical cavity mirrors.	12
2.3	The graphical representation of different cavity configurations depends on the stability parameters g_1 and g_2 . The grey area shows the stable regions. The most stable configuration is a symmetrical confocal cavity (yellow dot) and stability varies along the red line. The borderline cases (green dots) are the planar parallel and the spherical concentric cavities. Also, hemispherical cavities, which have one planar and one spherical mirror, are denoted by pink dots.	17
2.4	Schematic of a cavity transmission process. Laser light enters the optical cavity through M_1 and it will reflect multiple times between M_1 and M_2	18

- 2.5 A plot of single resonance feature of Fabry-Perot cavity with different mirror reflectivities. The resonance is sharp for $r = 0.99$ with high finesse. It becomes broader for $r = 0.95$ and $r = 0.80$ with low finesse. 20
- 2.6 The cavity transmission spectrum is plotted using Equation.2.48 with linewidth (FWHM) and free spectral range (FSR). 21
- 2.7 Optical cavity with length of $d_1 + d_2$, w_0 shows the smallest waist inside the cavity. The mirror on the left has a radius of curvature R_1 and the mirror on the right has a radius of curvature R_2 . . . 22
- 2.8 Different configurations of the misalignment between the laser beam (green dashed line) and cavity mode (red solid line). . . . 23
- 2.9 An arrangement of two lenses to achieve strong coupling between the laser and optical cavity. 25
- 2.10 a) Commercial membrane from Norcada [1]. b) Transverse amplitude along the z direction. 27
- 2.11 Simulated vibrations of the square membrane with different mode numbers (i,j). 30
- 2.12 Power spectral density is plotted using Equation 2.87. Assuming that a SiN membrane at room temperature $T_{bath} = 300\text{K}$, has $\omega_m = 2\pi \times 397\text{kHz}$, $M = 3.9 \times 10^{-11}\text{kg}$ and $Q = 10^6$ 34
- 2.13 Schematic of the basic optomechanical system. Laser light can change the position of the mechanical oscillators by the radiation pressure and the motion of mechanical oscillators with extremely high precision can be measured by sending the reflected beam by a detector. 37

- 2.14 Optical element with the incident, transmitted and reflected light fields. 40
- 2.15 A schematic representation of the membrane in the middle of the optical cavity. A thin dielectric membrane locates at Δx_m along the optical axis of the cavity. It divides the length of the cavity into two, on the left L_1 and on the right L_2 . A_0, B_0, A_3, B_3 are the incident, reflected, transmitted fields. $A_1, A'_1, A_2, A'_2, B_1, B'_1, B_2, B'_2$ are circulating fields. 41
- 2.16 The total reflection coefficient is plotted for a cavity has a length of $L_1 = L_2 = 15mm$ with wavelength $\lambda = 780nm$ and reflectivities of $r_1 = 0.99, r_2 = 0.995, r_m = 0.22$ at different values of Δx_m where $\eta_1^2 = 0.7$ 45
- 2.17 The total reflection coefficient is plotted with the same parameters as in Figure.2.16 but for several values of η_1^2 at different membrane positions Δx_m 45
- 2.18 Theoretical simulations show the total reflectance of the resonator as a function of the membrane position and laser frequency (a) or back mirror position (b). For clarity, an exaggerated optical instability loss with $\eta_1 = 0.7$ was used, resulting in low-finesse modes. Dashed lines indicate loss-less sub-cavity modes for 100% membrane reflectivity. 47

2.19 a)Types of photons polarization in a real space presentation for light travelling along the z-axis. Red arrows indicate the direction of the electric field oscillation. b) Polarisation is represented on the Poincaré sphere. Circularly polarized photons along S_z (here S_z is a classical component when we consider many photons in a pulse) and the grey disc represents Heisenberg uncertainty of the transverse components \hat{S}_x and \hat{S}_y . c)Top view of (b) where the field quadrature \hat{P}_L and \hat{X}_L are identical d)Squeezing of one quadrature. 48

2.20 Schematic of the balanced homodyne detection. 52

2.21 Schematic of the polarization of the beam in the converter. QWP refers to a quarter-wave plate and HWP refers to a half-wave plate 55

3.1 Birefringent crystal. a)Schematics of an unpolarized beam that is doubly refracted by birefringent crystal. The input beam splits into an ordinary beam (o-ray) and an extraordinary beam (e-ray). The ordinary beam will be linearly polarized and travels just like in an isotropic medium. The extraordinary beam will be polarized in the orthogonal direction and will be laterally displaced b) Photo of calcite crystal showing the effect of double refraction [2] 61

- 3.2 Design of the position-to-polarization converter. A stable polarization interferometer is formed between a beam displacer and an asymmetric, plano-convex optical cavity containing a transparent membrane. The input beam is split into the signal (red) and reference (green) beams of orthogonal polarization. The signal beam is mode-matched to a TEM_{00} mode of the cavity. Upon reflection from the entrance mirror, located in the focal plane of a lens, both beams are recombined by the displacer, thus closing the interferometer. A double-pass through a quarter-wave plate (QWP) provides the necessary exchange of horizontal and vertical polarization components for beam recombination. As a result, membrane motion causes phase shifts of the signal beam and thus variation of the output polarization. Resonator length and membrane position can be actively controlled. 62
- 3.3 Geometry of reference beam alignment. If the lens-cavity distance deviates from one focal length, the returning signal (red, along the optical axis) and reference beams (green) will not be parallel, leading to reduced mode overlap after recombination by the beam displacer (not shown). The dashed line shows the intended reference beam path. The depicted degree of typical misalignment is exaggerated here for clarity. 64
- 3.4 The reference beam has an angle α with respect to the signal beam, where the crest is indicated by the solid line and the dashed line marks the trough. The constructive interference is yellow highlighted and it occurs when the crest of one of the beams intersects with a crest of another beam or a trough meets another trough. The destructive interference is grey-highlighted and it appears where a crest meets a trough. 66

3.5	The six images illustrate how the spacing between fringes Δz varies with distance in mm. (Images are taken using ThorCam software (DCC1645C) with resolution $(1280 \times 1024 \text{ Pixels})$	68
3.6	The mismatch in the overlap between signal and reference beam. Alignment precision and mode overlap (bottom). The spatial fringe frequency is proportional to the deviation of lens-cavity distance from one focal length and can be used to locate the correct lens position (top). The expected mode overlap for deviations from that position shows the tolerance to misalignment. The estimated positioning accuracy of $\approx \pm 0.7 \text{ mm}$ allows for a mode overlap of better than 0.985. (bottom)	69
4.1	Holder design for a stable cavity.	71
4.2	Illustration of the lengths of each material where $(\alpha_{\text{Aluminum}} > \alpha_{\text{Invar}})$	72
4.3	The membrane holder.	73
4.4	(a) Membrane holder fixed into optical cavity mount. (b) Assembly of all parts of the optomechanical holder which are attached to a flange that is provided with electrical feedthrough to power PZTs in (c).	74
4.5	A photograph of MIM optical breadboard, showing the MIM vacuum chamber and optical elements.	75
4.6	Setup for filter cavity experiment. Laser light is sent through a filter cavity to eliminate the laser frequency fluctuations.	76

- 4.7 Experimental MIM setup including position to polarization converter detection. A-D are waveplates which are adjusted sequentially in order to optimise the polarization. 77
- 4.8 The balanced signal as a function of detuning between cavity and laser beam. 79
- 4.9 Rotating QWP will change the polarization of the recombined beam resulting in two beams. The grey beam is undesirable and QWP has to be rotated to eliminate it. 80
- 4.10 Adjustment of polarimetric measurement basis. The imbalanced signal and reference beam returning from the cavity are combined in a horizontal/vertical (H/V) basis with some phase offset ϕ_0 and varying phase difference $\Delta\phi$. The combined polarisation is depicted on the Poincaré sphere in (a). A quarter-wave plate introduces a 90-degree rotation about the anti-/diagonal (A/D) axis, shown in (b), transforming signal and reference to orthogonal circular polarisations (L/R). Finally, a half-wave plate allows for the compensation of the phase offset by introducing opposite phase shifts to the circular components (and swapping L/R). The phase difference $\Delta\phi$ is mapped onto the imbalance between H and V polarisations 81
- 4.11 The reflected signal from the cavity as a function of frequency. If the frequency is modulated with a small shift, one can tell from the slope which side of resonance the frequency is on. . . 82
- 4.12 The PDH error signal and the sidebands at frequency modulation at $\Omega = 6\text{MHz}$ 85
- 4.13 Locking setup to lock the MIM cavity via balanced signal. . . . 86

4.14 Active stabilization locking setup to lock the filter cavity using PDH technique.	87
4.15 The error signal with generated sidebands. Top: when there is no feedback to the DC modulation laser and the laser is scanned sufficiently fast over the cavity resonance. Bottom: When there is feedback to the DC modulation laser, the laser frequency is kept longer in the vicinity of the resonance and fast frequency fluctuations become visible in the error signal.	88
4.16 Feedback block system.	89
4.17 Noise feedback using different attenuators.	90
4.18 Feedback noise level with different attenuators. At ∞ dB, there is no feedback connected and at 0dB is direct feedback with no attenuator.	91
4.19 Bode plot for frequency response of the feedback system. Top: The amplitude $20\log(A)$ versus the frequency $\log(f)$. The high gain corresponds to low frequency whereas the low gain corresponds to high frequency. Bottom: The phase changes sharply at a higher frequency and it is zero around 5.5 Hz but increases to 180 degrees for lower frequency	92
4.20 Nyquist plot shows the system stability within the amplitude range which should not exceed the critical point.	93
5.1 Cavity transmission which shows the fundamental mode TEM_{00} .	95

- 5.2 Transverse mode of the cavity. Theoretical intensity profiles are shown in the top row and the lower row refers to experimental images for cavity transmission. Column a \rightarrow ($l=0,m=0$) and b \rightarrow ($l=0,m=1$) are profile for Hermite-Gaussian mode whereas c \rightarrow ($p=0,m=1$) and d \rightarrow ($p=1,m=1$) are profile for Laguerre-Gaussian mode. 96
- 5.3 Intensity profiles of the reflected beam. The near-Gaussian intensity profile of the signal beam is shown in (a) and the residual reflected intensity for the resonant cavity is shown in (b). Cuts through the data and modelled intensity distributions for those profiles as well as the assumed intensity profile of the cavity are shown in (c). 96
- 5.4 The amplitude reflectivity is plotted versus laser wavelengths (top) and versus the membrane thickness (bottom). At $\lambda = 795nm$ and $d_m = 50nm$, the amplitude reflection coefficient is estimated to be 0.47. 97
- 5.5 Setup for measuring the gain of the PZT a)cavity b)membrane. 98
- 5.6 The slope of the two plots estimates the gain of the PZT of the cavity G_c (top) and of the membrane G_m (bottom). 99
- 5.7 This plot shows the difference between the maximum and minimum of the location of the resonance which can be used to estimate α_m 100
- 5.8 The plot shows the position of the dispersive signal versus the membrane position. The slope is fitted between MIM cavity resonance maxima and minima. The x and y axis is calibrated by $\Delta x_m = \alpha_m V'_m$ and $f = V'_c FSR / \Delta V'_c$ respectively. 101

5.9	The dispersive signal with the linear fit to estimate σ	102
5.10	MIM cavity resonance as a function of the back mirror position. a)The MIM transmitted resonance at different membrane locations shows low finesse at $V_m = 5.5V$ and high finesses at $V_m = 2.5V$. b) It shows the phase of each resonance. The x-axis is calibrated by $\Delta V_c \alpha_c / \Delta t$	103
5.11	Experimental data for resonance locations has been overlaid (black dots). Corresponding full linewidths, measured as mirror displacement w_z , are shown together with the theoretical expectation for an estimated $\eta_1 \approx 0.994$. We attribute deviations to spurious coupling to higher-order, transversal cavity modes. . .	104
5.12	Mechanical modes of membrane for different frequencies. The modes of the membrane in Table 5.1 are indicated	107
5.13	Shot noise limited detector response. The spectral response of our 1 MHz-bandwidth balanced detector to photon shot noise is plotted for different power. One-sided power spectral density $G_{UU}(f) = 2S_{UU}(f)$ was measured with a 100 Hz effective bandwidth.	108
5.14	Noise power dependence of amplified photo-current noise at different frequency values. It is plotted versus light power which shows that the noise power will increase linearly with optical power.	109

5.15	Thermal noise of the membrane is detected for dispersive coupling (trace A). For membrane positions near minimal dispersive coupling (trace B), only higher-order membrane modes remain visible. Here, the combined level (black line) of photon shot noise ($\approx 1.0 \times 10^{-12} \text{ V}^2/\text{Hz}$) and electronic noise ($\approx 2.3 \times 10^{-12} \text{ V}^2/\text{Hz}$) near 400 kHz at a total light power of $8.3\mu\text{W}$ is just above the electronic noise (dashed line). For improved conditions (trace C) with lower membrane damping (lower vacuum pressure) and reduced laser frequency noise, signal-to-noise-ratio improves and near-degenerate modes can be resolved. For comparison, (aliased) expected mode frequencies for an almost square membrane (1.01 side ratio) with a fundamental frequency of 397.5 kHz are indicated.	111
5.16	Fundamental mode of membrane ω_{11} at 397 kHz at lowered vacuum pressure.	112
5.17	Thermal noise measurement at $150\mu\text{W}$ and $300\mu\text{W}$. The measurement is taken by fixing the total power and changing the ratio between the signal beam power and reference beam power.	113
5.18	The ratio of the noise power and reference power at $150\mu\text{W}$ and $300\mu\text{W}$ which is proportional to the cavity signal power.	114

Chapter 1

Introduction

Hybrid quantum systems have received significant interest, especially with the goal of technological exploitation of complementary capabilities for quantum information processing and communication tasks. Quantum transducers can be used to couple the properties of one object or system to different properties of another system, thus combining e.g. robust transmission of photonic quantum states with strong interactions between material quantum objects [3]. Driven further, this type of research develops a toolbox for the engineering of strong interactions between quantum systems, thus building quantum machines.

These systems are important because they have many possible applications. An important example is that optomechanical systems are effective in sensing uses ranging from gravity wave interferometry [4] to atomic force microscopy. However, the detection of the displacements for example in accelerometers is restricted by the standard quantum limit which sets a limit on the weakest forces that can be measured. This measurement is limited by the quantum noise of light and its backaction on the interferometer mirrors. Optomechanical devices are appealing for quantum computing because of their ability to store, transduce and retrieve quantum information where

the mechanical oscillator can be excited into other states by the laser beam. Let's say a transferred quantum state on a microwave signal can be stored in a mechanical oscillator by coupling interactions, it will be retrieved by a laser beam pulse interacting with the same mechanical oscillation [5]. They are also promising for future quantum networking, thus mapping the quantum state of a material quantum system on the state of a laser beam and vice versa can be used to couple distant and different quantum systems.

Optomechanical systems have a wide range of configurations and sizes, allowing access to several parameters and operational regimes. A well-studied, prototypical system where the membrane-in-the-middle (MIM) arrangement is introduced by Thompson et al.[6]. The micro-mechanical membrane couples to the electromagnetic field inside an optical cavity which is driven by low-noise lasers via the radiation pressure force. A typical membrane material is silicon nitride (Si_3N_4), which combines low optical absorption in the near-infrared with low mechanical loss[7]. Engineering of SiN membranes and beams led to demonstrations of extremely high mechanical quality (Q) factors [8–11] that enable quantum mechanical experiments with massive objects at room temperature.

The MIM optomechanical system is characterised by the detuning (for dispersive coupling) or the change of optical loss (for dissipative coupling) that affects a light beam when the position of the membrane is changed [6, 12]. This system can be used to observe the quantum noise effects, but it must be shielded from all external forces to eliminate all classical noises like phase, frequency, intensity fluctuations of the laser beam and any environment seismic vibrations. The effects of typical effects of quantum noise on the MIM system can be studied. Photon shot noise limits the precision with which the position of the membrane can be measured. At the same time, back-action noise arises from the radiation pressure and alters the momentum of the membrane. Together, these two types of noise preserve the validity of the uncertainty prin-

principle. The shot noise leads to a noisy output of the photodetector and this noise is intrinsically linked due to the quantum nature of photons as they reach the detector at random time intervals, leading to uncertainty in its position measurement [13]. The quantum back-action noise results from each photon causing a momentum kick to the membrane, which increases the uncertainty in its momentum, such that the Heisenberg uncertainty principle is fulfilled.

There have also been many experiments on the quantum mechanical interaction between light and atomic ensembles [14] where polarised light was used to drive effective interactions [15], generate entanglement [16], and deterministically teleport quantum states between macroscopic objects [17]. A key feature is the robustness of the polarisation state of light that preserves quantum properties over long distances. It is thus the combination of these systems that currently receive interest for the realisation of hybrid systems. It served for studies of quantum measurement back-action in the optical detection of macroscopic objects and demonstration of back-action evading measurement of mechanical oscillation [18]. The same toolbox enabled entanglement [19] and strong coherent coupling [20] between a membrane and an atomic ensemble. The same type of remote link was employed for quantum coherent measurement and feedback, where reducing entropy removal from the spin degrees of freedom in an atomic ensemble by optical pumping can be converted to cooling of a mechanical mode of vibration [21].

Observation of the back-action of the atoms onto the membrane has been studied [22]. The laser beam is strongly coupled with a micromechanical membrane and a collective atomic spin over a distance of 1 meter at temperature 300K [20]. However, it requires a stable interferometer, which is technically difficult. In this work, we design a position-to-polarisation converter to map the position of a micromechanical silicon nitride (Si_3N_4) membrane onto the polarization of a laser beam in an interferometrically stable way. This device

can reduce some of the technical overhead when coupling a polarised light beam to an optical cavity that interacts with a mechanical resonator. It works as an alternative approach that can be used for strong coupling between a micromechanical membrane and the atomic spin with no maintenance.

1.1 This Work

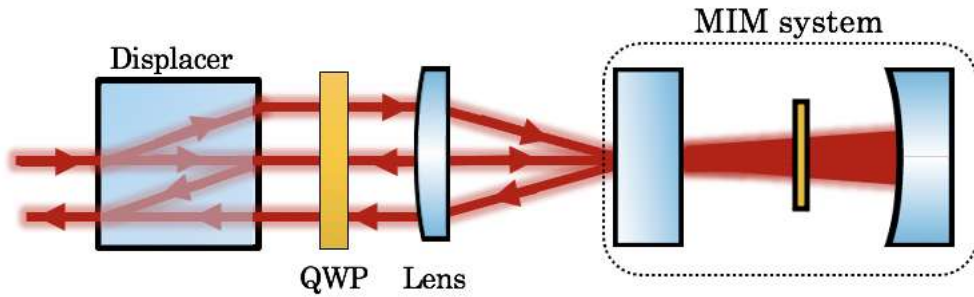


Figure 1.1: Construction of hybrid system with a robust polarization interferometer. It shows light-membrane coupling via an optical cavity and the input beam interferes with the reference beam. QWP represents a quarter wave plate.

The basic construction of the hybrid optomechanical system that is described in this thesis is shown in Figure 1.1. It aims to design a transducer that we named a position-to-polarization converter that maps the small position changes of the micromechanical membrane onto the polarization of a laser beam. A micromechanical membrane sits in the middle of an asymmetric optical cavity and causes phase shifts in the reflected near-resonant light field. A birefringent crystal which is the key part of the design of the transducer is used as a beam displacer to combine the signal beam with a mode-matched, orthogonally polarized reference beam for polarization encoding. This is done with a robust interferometric setup where the two-path of the interferometer has an exact length with no need for stabilization. The system is distinguished by its accuracy and is easily operated. Subsequent balanced homodyne measurement is used for detecting the membrane thermal noise. In the regime of high optomechanical coupling strength, the high signal-to-noise ratio should enable

us to detect the motional quantum noise. This experiment pursues an alternative approach that can be used for strong coupling between a micromechanical membrane and the atomic spin with no maintenance. The main objective is to observe the quantum effects and reach the optomechanical system with high position sensitivity. A short summary of each chapter is provided below.

1.2 Thesis Outline

This thesis is organised as follows:

Chapter 2 discusses fundamental concepts of optical cavities and their coupling to laser beams. It also gives a theoretical description of the mechanical membrane and its coupling to the light field when it sits in the middle of an optical cavity as well as a description of the read-out process via polarimetric measurements

Chapter 3 introduces to the reader the details principle of our robust interferometer of the position to the polarization converter and shows the scheme of the beam alignment with the condition to have the optimum mode overlap. We use a method of observing interference patterns and intentional misalignment to evaluate the required alignment precision. It manifests the scenario of the beam misalignment that causes interference.

Chapter 4 describes experimental details and characterizes the experiment of optomechanical setup that is designed in such a way as to have a thermally stable system and is vacuum-compatible. Also, it highlights the primary considerations for the optomechanical system e.g mode matching, etc. The theory of Pound Drever Hall (PDH) locking is presented with our locking scheme. Also, the theory of the active feedback to suppress noise is expressed with its measurements. A polarimetric setup which is used for adjusting the

phase or the polarization in the detection stage is also provided.

Chapter 5 includes the experimental measurements and calibrations of our optomechanical system. The calibration of the piezo actuator (PZT) which allows us to estimate the position sensitivity is provided. Also, the finesse of the MIM cavity is discussed as a function of the membrane position. The resulting signal from the detection stage can be used for measuring the membrane's motion, and thermal noise of the membrane. In addition, the shot-noise limited sensitivity is estimated to compare it with membrane thermal noise to reach the strong coupling regime. An improvement in our thermal noise measurement to deduce the laser frequency noise using a filter cavity is shown.

Chapter 6 includes the conclusion of our experiment and emphasizes future experiments with the main ideas and goals recapitulated to converge to the big picture.

Chapter 2

Theoretical model of the optomechanical system

To comprehend the more sophisticated cavity operation that occurs when a thin, partially reflecting membrane is placed in the middle of the cavity, this chapter begins by describing the theoretical model and background of the optomechanical system. In fact, we will be focused on the coupling between the membrane oscillation and the light field entering and leaving the cavity, which will result in optomechanical coupling to laser beam polarization.

Thus, this chapter has four main sections as follows: First, the propagation of a coherent beam through an optical cavity is explained by the derivation of the paraxial wave equation including the properties of the optical cavity with their stability criteria. Also, the laser beam coupling mode matching the optical cavity is discussed using two lenses. The second section describes the micromechanical membrane vibration modes as a mechanical oscillator with its damping. In addition, it is described from the quantum mechanical aspect. Third, the principle of the optomechanics system is discussed in the simple case where one mirror of the optical cavity is attached to a spring. Besides, the theoretical description of the optomechanical system where the

micromechanical membrane sits in the middle of the optical cavity is provided. In this system, the phase of the light beam that leaves the cavity will be shifted according to the membrane position. Also, the polarization state of the laser beam is described to give a better understanding of our polarization interferometer. The fourth section presents the scheme of homodyne detection with its derivation and the noise readout from the polarization converter.

2.1 Basics of the Optical Cavity

2.1.1 Paraxial Wave Equation and Gaussian beams

In order to describe the electromagnetic field inside an axially symmetric optical resonator it is useful to introduce Gaussian beams. The wave equation of the electric field \mathbf{E} can be derived by Maxwell's equations in vacuum [23, 24] as

$$\nabla^2 \mathbf{E} - \frac{1}{c^2} \frac{\partial^2 \mathbf{E}}{\partial t^2} = 0 \quad (2.1)$$

where c is the speed of light in a vacuum. A monochromatic solution \mathbf{U} to the wave equation for a laser beam which travels in the z direction is given by

$$\mathbf{E} = \mathbf{U}(x, y, z) e^{i(kz - \omega t)} \quad (2.2)$$

substituting Equation 2.2 in the wave Equation 2.1 leads to the Helmholtz equation which is given by

$$\nabla^2 \mathbf{U}(x, y, z) + k^2 \mathbf{U}(x, y, z) = 0 \quad (2.3)$$

where $k = \frac{2\pi}{\lambda}$ is the wave number of the light. The Helmholtz equation provides

a monochromatic solution and it is given by

$$\mathbf{U}(x, y, z) = \psi(x, y, z)e^{ikz} \quad (2.4)$$

The function $\mathbf{U}(x, y, z)$ provides a useful expression of plane waves e^{ikz} . Substituting Equation 2.4 into Equation 2.3 becomes

$$\left[\frac{\partial^2 \psi}{\partial x^2} + \frac{\partial^2 \psi}{\partial y^2} + \frac{\partial^2 \psi}{\partial z^2} + 2ik \frac{\partial \psi}{\partial z} \right] e^{ikz} = 0 \quad (2.5)$$

Here we assume that the longitudinal variation of $\psi(x, y, z)$ along z is very small with respect to the transverse variation along x and y which means the beam will have a small divergence and it will remain close the central axis of beam propagation. Thus, the second order variation $\frac{\partial^2 \psi}{\partial z^2}$ will be ignored. Therefore, Equation 2.5 can be simplified as

$$\left[\frac{\partial^2}{\partial x^2} + \frac{\partial^2}{\partial y^2} + 2ik \frac{\partial}{\partial z} \right] \psi e^{ikz} = 0. \quad (2.6)$$

This is called the paraxial wave equation. The following expression satisfies Equation.2.6

$$\psi(x, y, z) = \mathbf{E}_0 e^{i[P(z) + k \frac{(x^2 + y^2)}{2q(z)}]} \quad (2.7)$$

Here the parameter $P(z)$ and $q(z)$ represents the complex phase shift and the complex beam curvature respectively. By substituting Equation.2.7 into the paraxial equation, we obtain

$$\left[\left(\frac{2ik}{q} - 2k \frac{\partial P}{\partial z} \right) (x^2 + y^2) + \left(\frac{k^2}{q^2} \frac{\partial q}{\partial z} - \frac{k^2}{q^2} \right) (x^2 + y^2) \right] \psi(x, y, z) = 0 \quad (2.8)$$

For Equation 2.7 to be a solution for all x and y , the coefficients of $(x^2 + y^2)$ must be equal to zero separately, yielding

$$\frac{\partial P}{\partial z} = \frac{i}{q} \quad (2.9)$$

and

$$\frac{\partial q}{\partial z} = 1 \quad (2.10)$$

In order to characterize the beam, it is possible to express the complex radius of curvature as a function of two real parameters: The complex radius of curvature $\frac{1}{q}$ can be written in term of two real parameters as[25]:

$$\frac{1}{q} = \frac{1}{R} + i \frac{\lambda}{\pi w^2} \quad (2.11)$$

where R is the radius of curvature of the wavefront and w is the transverse dimension of the beam. The width of the beam is determined by the distance from the axis when the intensity drops to $\frac{1}{e^2}$. By substituting Equation 2.11 into 2.7, the solution of Equation 2.8 is given by

$$\psi(x, y, z) = \mathbf{E}_0 e^{iP(z)} e^{ik \frac{(x^2+y^2)}{2R(z)}} e^{-\frac{(x^2+y^2)}{w^2}} \quad (2.12)$$

where $e^{iP(z)} = \frac{\omega_0}{\omega(z)} e^{-i\phi(z)}$, ω_0 is the minimum waist and $\phi(z) = \tan^{-1}(\lambda z / \pi \omega_0^2)$ is known as the Gouy phase. At this point, we have a mathematical representation of the Gaussian beam of the electric field as

$$\mathbf{E}(r, z, t) = \frac{\mathbf{E}_0 w_0}{w(z)} e^{ik \frac{(r^2)}{2R(z)}} e^{-\frac{(r^2)}{w^2}} e^{-i[\phi(z) - kz + \omega t]} \quad (2.13)$$

with $r^2 = x^2 + y^2$, this full expression is a solution to the wave equation[23]. By comparing Equation 2.11 with Equation 2.7, it can be easy to understand the behaviour of the radius of curvature and the beam transverse size in terms of the spot size w_0 (minimum beam size). The beam waist and the radius of curvature are related to distance z as follows

$$\omega(z) = \omega_0 \sqrt{1 + \left(\frac{z}{z_R}\right)^2} \quad (2.14)$$

$$R(z) = z \left[1 + \left(\frac{z_R}{z}\right)^2 \right] \quad (2.15)$$

where z_R is Rayleigh range and it is given by

$$z_R = \frac{\pi\omega_0^2}{\lambda} \quad (2.16)$$

Consequently, the Rayleigh range is a measure of the length of the waist region where spot size is smallest as illustrated in Figure.2.1. Using Equation 2.14 and 2.15, one can see that for $z \rightarrow \infty$, w will linearly increase with z so that

$$\omega \approx \omega_0 \frac{z}{z_R} \quad (2.17)$$

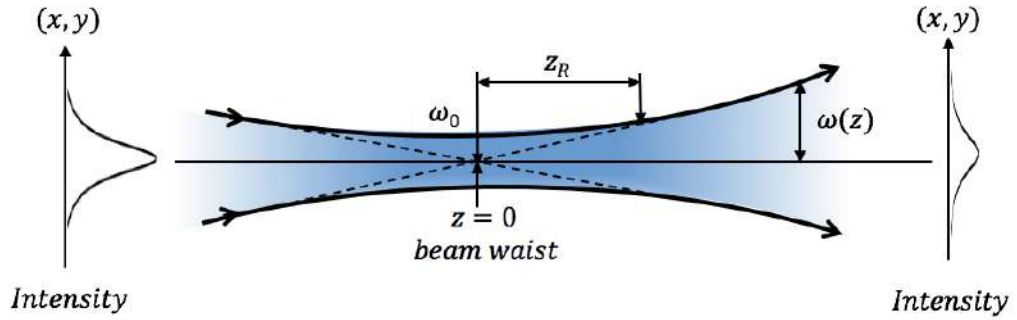


Figure 2.1: A Gaussian beam variation of the beam size $w(z)$ as a function of the distance z along the beam, which forms a hyperbola.

At position $z = 0$ beam waist, the wavefronts are plane waves and the wavefront curvature is minimum at $z = z_R$. For large distances $z \gg z_R$, one can define an angle θ which describes the beam divergence in the far field propagation of a Gaussian beam. The divergent angle is given by

$$\theta = \frac{\omega(z)}{z} = \frac{\lambda}{\pi\omega_0} \quad (2.18)$$

The Gaussian beam inside the optical cavity shown in Figure 2.2 has spherical wavefronts. For the two mirrors positioned at z_1 and z_2 respectively, the radii of the wavefronts at the mirrors must match their respective radii of curvature, R_1 and R_2 . Thus

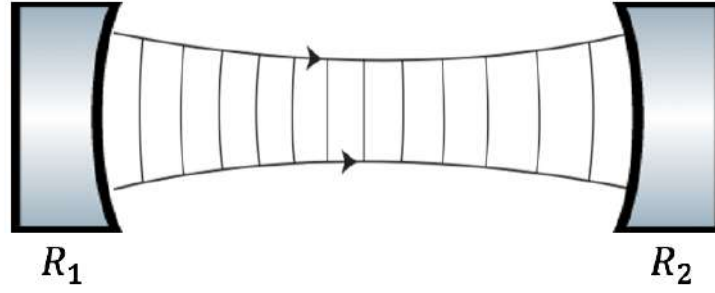


Figure 2.2: A Gaussian beam matches the radii of curvature of the optical cavity mirrors.

$$R(z_1) = z_1 + \frac{z_R^2}{z_1} = -R_1 \quad (2.19)$$

$$R(z_2) = z_2 + \frac{z_R^2}{z_2} = R_2 \quad (2.20)$$

where minus sign in Equation 2.19 comes from the sign convention used for the mirror and radii of the wavefront. The mirror separation L_{cavity} can be written as

$$L_{cavity} = z_2 - z_1 \quad (2.21)$$

Using Equation 2.21 and 2.19 enables us to obtain z_1 , z_2 and z_R in terms of the mirror radii and its separation as follows

$$z_1 = \frac{-L_{cavity}(R_2 - L_{cavity})}{R_1 + R_2 - 2L_{cavity}} \quad (2.22)$$

$$z_2 = \frac{L_{cavity}(R_1 - L_{cavity})}{R_1 + R_2 - 2L_{cavity}} \quad (2.23)$$

$$z_R^2 = \frac{L_{cavity}(R_1 - L_{cavity})(R_2 - L_{cavity})(R_1 + R_2 - L_{cavity})}{(R_1 + R_2 - 2L_{cavity})^2} \quad (2.24)$$

Similarly, the minimum spot size ω_0 explicitly can be expressed in terms of the

mirror radii of curvature, their separation and the wavelength as

$$\omega_0 = \frac{(\lambda/\pi)^{1/2} [L_{cavity}(R_1 - L_{cavity})(R_2 - L_{cavity})(R_1 + R_2 - L_{cavity})]^{1/4}}{(R_1 + R_2 - 2L_{cavity})^{1/2}} \quad (2.25)$$

we obtain the beam spot sizes at the mirrors using Equation 2.14 as

$$\omega_1 = \omega_0 \sqrt{1 + \frac{z_1^2}{z_R^2}}, \quad (2.26)$$

$$\omega_2 = \omega_0 \sqrt{1 + \frac{z_2^2}{z_R^2}}, \quad (2.27)$$

The phase of the Gaussian-mode field along the optical axis of the optical cavity is given by

$$\theta(z) = kz - \tan^{-1} \left(\frac{z}{z_R} \right) \quad (2.28)$$

Along the optical axis, the phase change of the field in a round trip must be an integral multiple of 2π which imposes that the electric field at the mirrors is zero, therefore

$$\theta(z_2) - \theta(z_1) = k(z_2 - z_1) - \left[\tan^{-1} \frac{z_2}{z_R} - \tan^{-1} \frac{z_1}{z_R} \right] = n\pi \quad (2.29)$$

where $n = 0, 1, 2, \dots$. The allowed values of k are given by this expression and the resonance frequencies $f = kc/2\pi$ and the allowed mode frequencies are

$$f_n = \frac{c}{2L_{cavity}} \left(n + \frac{1}{\pi} \cos^{-1} \sqrt{\left[1 - \frac{L_{cavity}}{R_1}\right] \left[1 - \frac{L_{cavity}}{R_2}\right]} \right). \quad (2.30)$$

which are found using Equations 2.21–2.23

There are other solutions to the paraxial Equation 2.6 which form a complete and orthogonal set of functions. These solutions are sums of forward and backward propagating Gaussian beams that match that shape and are named

“ modes of propagation” [26]. These modes can represent the modes of the electromagnetic field inside the optical cavity. They are a full set of solutions that satisfies the paraxial equation. In Cartesian coordinates, a full set of solutions which have a rectangular symmetry is known as Hermite Gaussian modes and it is given by [27]

$$\psi_{l,m}(x, y, z) = \frac{w}{w_0} \cdot H_l \left(\frac{\sqrt{2}x}{w} \right) \cdot H_m \left(\frac{\sqrt{2}y}{w} \right) \mathbf{E}(r, z) e^{i[l+m]\phi(z)} \quad (2.31)$$

H_l and H_m are the Hermite polynomials of order l and m ($l, m = 0, 1, \dots$). The lowest order mode can be found when $l = m = 0$. In this case, the Hermite polynomial zeroth order is constant, thus Equation 2.31 is turned into a Gaussian beam as in Equation 2.13. The zero-order mode is called TEM_{00} . Another complete set solution which obeys the axial symmetry in cylindrical coordinates is the Laguerre Gaussian mode. Thus, it can be expressed as

$$\psi_{p,l}(r, \phi, z) = \frac{w}{w_0} \cdot L_p^l \left(\frac{2r^2}{w^2} \right) \left(\frac{\sqrt{2}r}{w} \right)^2 \mathbf{E}(r, z) e^{i[2p+l]\phi(z)} \quad (2.32)$$

The lowest order mode at $l = p = 0$ is exactly a Gaussian beam. Higher order modes are produced when the light beam is not completely symmetric which causes a different waist size between the horizontal and vertical [28]. The optical cavities' boundary condition, stability and properties will be described in detail in the following sections.

2.1.2 ABCD Matrices and Beam Propagation

To understand the behaviour of light in an optical cavity, the ray tracing technique is used to relate the ray vectors at the input and output planes by the ray transfer matrix (RTM). The RTM analysis allows us to determine the stability criterion in the cavity.

The transmission of the paraxial ray through any optical component can be described by its positions x and its angle θ with respect to the optical axis. The position and the angle of the input and output ray in front of the optical component is represented by a column vector $\vec{p} = \begin{pmatrix} x \\ \theta \end{pmatrix}$ whereas the optical components are represented by a 2×2 matrix M with real numbers. Thus, it can be written in this form

$$\vec{p}' = M \cdot \vec{p} \quad \text{or} \quad \begin{pmatrix} x' \\ \theta' \end{pmatrix} = \begin{pmatrix} A & B \\ C & D \end{pmatrix} \cdot \begin{pmatrix} x \\ \theta \end{pmatrix} \quad (2.33)$$

The most important optical components like lenses, mirrors, etc. are described by these kinds of matrices [29]. For the propagation light with distance S , the transfer matrix of a thin lens with the focal length f is given by:

$$M_s = \begin{pmatrix} 1 & S \\ 0 & 1 \end{pmatrix} \quad \text{or} \quad M_f = \begin{pmatrix} 1 & 0 \\ -1/f & 1 \end{pmatrix} \quad (2.34)$$

The optical system can be constructed with more than one optical component. In the case of a system that has two thin lenses, the RTM of the system is simply a multiplication of five different transfer matrices: the ray propagation from the initial point to the first lens, refraction by that lens, ray propagation from the first lens to the second lens, the refraction by the second lens and finally the propagation to the endpoint:

$$M_g = M_{s3} M_{f2} M_{s2} M_{f1} M_{s1} \quad (2.35)$$

The beam tracing can be computed by Equation 2.33. This analysis reduces a complicated optical system to one single matrix and offers the possibility of tracing a ray propagation with a limited number of multiplications.

2.1.3 Types of Optical Cavities and Their Stability

It is possible to build an optical cavity with a different configuration of mirrors. These different types of configurations can be formed at least by two mirrors, and it is essential that their centre is on the optical axis. The optical cavity is geometrically symmetric if the radius of curvature of the two mirrors is identical, whereas mirrors with different radii of curvatures form asymmetrical cavities. The length of the cavity and the radius of curvature of the mirrors play an important role in the stability criteria of the cavity. The focus of a curved mirror is given in the limits of paraxial approximation by $f = R/2$ [30]. The two mirrors are separated by distance L_{cavity} and both have radii of curvatures R_1 and R_2 . One round trip of the ray can be described with Equation 2.35, thus

$$M_g = \begin{pmatrix} 1 & L_{cavity} \\ 0 & 1 \end{pmatrix} \begin{pmatrix} 1 & 0 \\ -\frac{2}{R_1} & 1 \end{pmatrix} \begin{pmatrix} 1 & L_{cavity} \\ 0 & 1 \end{pmatrix} \begin{pmatrix} 1 & 0 \\ -\frac{2}{R_2} & 1 \end{pmatrix} \quad (2.36)$$

The result of the multiplication leads to

$$M_g = \begin{pmatrix} 1 - \frac{2L_{cavity}}{R_2} - \frac{4L_{cavity}}{R_1} + \frac{4L_{cavity}^2}{R_1R_2} & 2L_{cavity} - \frac{2L_{cavity}^2}{R_2} \\ -2\left(\frac{1}{R_1} + \frac{1}{R_2}\right) + \frac{4L_{cavity}}{R_1R_2} & 1 - \frac{2L_{cavity}}{R_2} \end{pmatrix} \quad (2.37)$$

The light inside the optical cavity undergoes several reflections back and forth many times between the two mirrors. The optical cavity stability can be specified by finding the eigenvalues of M_g . The stability condition is given by

$$0 \leq \underbrace{\left(1 - \frac{L_{cavity}}{R_1}\right)}_{g_1} \underbrace{\left(1 - \frac{L_{cavity}}{R_2}\right)}_{g_2} \leq 1 \quad (2.38)$$

where g_1 and g_2 are called stability parameters. Any cavity with two plane

or spherical mirrors must obey Equation 2.38 to be stable. Figure 2.3 shows graphically the stability of different configurations of the optical cavity[28].

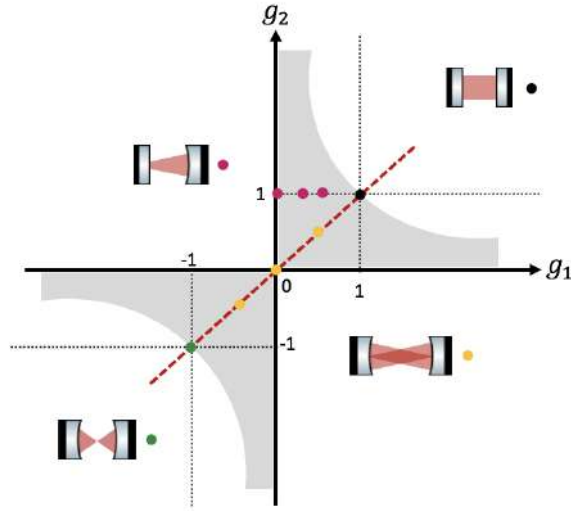


Figure 2.3: The graphical representation of different cavity configurations depends on the stability parameters g_1 and g_2 . The grey area shows the stable regions. The most stable configuration is a symmetrical confocal cavity (yellow dot) and stability varies along the red line. The borderline cases (green dots) are the planar parallel and the spherical concentric cavities. Also, hemispherical cavities, which have one planar and one spherical mirror, are denoted by pink dots.

In the following section, we will restrict the description to TEM_{00} mode and discuss it as a one-dimensional simplification in more detail.

2.1.4 Fabry-Perot Cavity and its Properties

Optical cavities are defined by their reflection and transmission properties. Even though we use an asymmetrical cavity in our optomechanical setup, this section provides the relevant theory for a simple case (symmetrical case). The important relevant features for example free spectral range, finesse and quality factor can be demonstrated in the simple case and generalized for different cavities according to [31].

Let us assume a Fabry-Perot cavity consists of two mirrors separated by a fixed distance L_{cavity} with reflectivity r . When laser light enters a Fabry-Perot cavity with a field amplitude E_{in} through the input mirror M_1 as shown

in Figure 2.4, it will be reflected back and forth multiple times between the two mirrors. Assuming that we have ideal, lossless mirrors, the electric field amplitude of the light inside the optical cavity will be reduced by \sqrt{r} after reflection from the mirror, thus it is reduced by a factor of r after one full round trip [27].

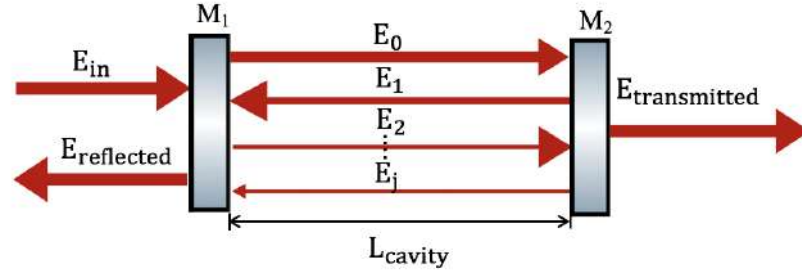


Figure 2.4: Schematic of a cavity transmission process. Laser light enters the optical cavity through M_1 and it will reflect multiple times between M_1 and M_2 .

In order for laser light inside the optical cavity to interfere with itself constructively after a full round trip forming a standing wave, it should satisfy

$$L_{cavity} = n \frac{\lambda_n}{2} \quad \text{with } n = 1, 2, 3, \dots \quad (2.39)$$

where n characterizes the cavity longitudinal modes. If this condition is satisfied in which beams constructively interfere at the coupling mirror M_1 , the frequency can be written as

$$f_n = n \frac{c}{2L_{cavity}} \quad (2.40)$$

In frequency space, the distance between two longitudinal modes (peaks) can be defined as Free Spectral Range (FSR) as seen in Figure 2.6. It can be written as

$$FSR = f_n - f_{n-1} = \frac{c}{2L_{cavity}} \quad (2.41)$$

If we assume the phase of the light wave at the first mirror M_{in} is zero, there will be a phase difference δ for the beam that circulated once in the cavity

after reflection. Thus, δ can be defined as

$$\delta = k \cdot 2L_{cavity} = \frac{2\pi \cdot 2L_{cavity}}{\lambda} = 2\pi f \frac{2L_{cavity}}{c} = \frac{2\pi f}{FSR} \quad (2.42)$$

where f is the light's frequency as it enters the cavity. The amplitude of the electric field after one full round trip is given by

$$E_{j+1} = r \cdot E_j e^{i\delta} \quad (2.43)$$

E_j represents the amplitude of the field in the optical cavity after j round trips. The optical cavity's overall amplitude is represented by

$$E_{cavity} = E_0 + E_1 + E_2 + \dots = \sum_{j=0}^{\infty} r \cdot E_0 (e^{i\delta})^j = E_0 \frac{1}{1 - r e^{i\delta}} \quad (2.44)$$

E_{cavity} experimentally can be measured by its intensity, which is described by $I_{cavity} = |E_{cavity}|^2$. Thus, the intensity of light inside the cavity is related to the incoming light intensity by

$$\frac{I_{cavity}}{I_{in}} = \left| \frac{E_0}{E_{in}} \right|^2 \cdot \left| \frac{1}{1 - r e^{i\delta}} \right|^2 = \frac{1}{(1 - r)} \frac{1}{1 + \left(\frac{2\mathcal{F}}{\pi}\right)^2 \sin^2\left(\frac{\delta}{2}\right)} \quad (2.45)$$

This is known as the Airy function and it is Lorentzian in shape, see Figure 2.6. The finesse \mathcal{F} represents the quality of the cavity to sustain the constructive interference along the path length in the cavity and it is defined as [32]

$$\mathcal{F} = \frac{\pi\sqrt{r}}{1 - r} \quad \text{with} \quad r = r_1 r_2 \quad (2.46)$$

If $r \approx 1$, \mathcal{F} will be high and lead to narrow resonance features with a small

value of full width at half maximum (FWHM) linewidth which is given by

$$FWHM = \kappa = \frac{FSR}{\mathcal{F}} \quad (2.47)$$

On the other hand, the resonance of the cavity will get broader for lower values of r as shown in Figure 2.5.

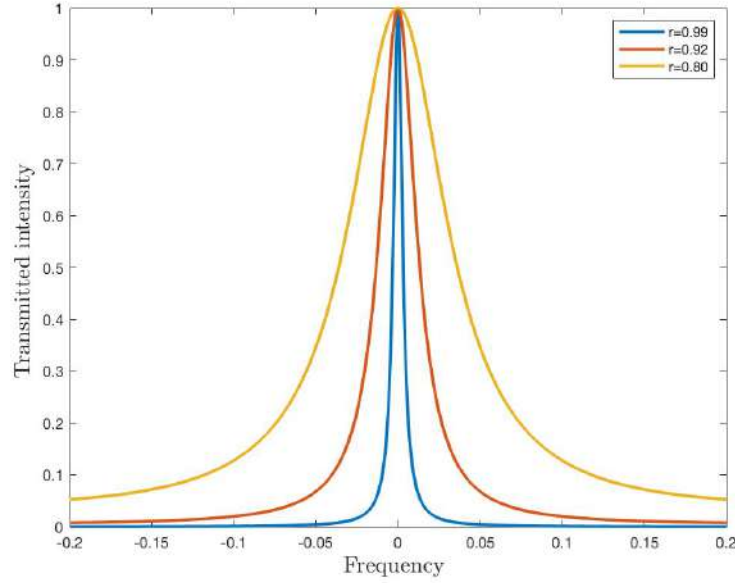


Figure 2.5: A plot of single resonance feature of Fabry-Perot cavity with different mirror reflectivities. The resonance is sharp for $r = 0.99$ with high finesse. It becomes broader for $r = 0.95$ and $r = 0.80$ with low finesse.

The light intensity of the transmission and reflection of the cavity can be described using Equation 2.45 by

$$I_{transmitted} = (1 - r)I_{cavity} = \frac{I_{in}}{1 + \left(\frac{2\mathcal{F}}{\pi}\right)^2 \sin^2\left(\frac{\delta}{2}\right)} \quad (2.48)$$

$$I_{reflected} = 1 - I_{transmitted} = \frac{\left(\frac{2\mathcal{F}}{\pi}\right)^2 \sin^2\left(\frac{\delta}{2}\right)}{1 + \left(\frac{2\mathcal{F}}{\pi}\right)^2 \sin^2\left(\frac{\delta}{2}\right)} \quad (2.49)$$

Moreover, the phase shift of the transmission and reflection of the cavity are frequency dependent and they express as[33]

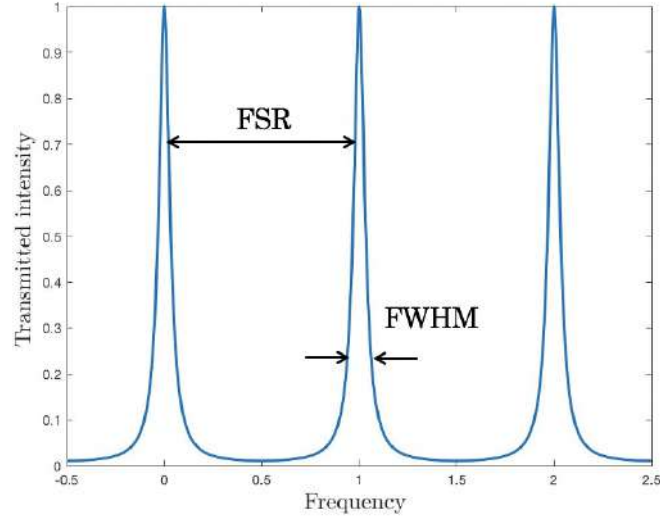


Figure 2.6: The cavity transmission spectrum is plotted using Equation.2.48 with linewidth (FWHM) and free spectral range (FSR).

$$\Delta\delta_{transmitted} = \tan^{-1} \left(\frac{-\sin\delta}{r - \cos\delta} \right) \quad (2.50)$$

$$\Delta\delta_{reflected} = \tan^{-1} \left(\frac{(1-r)\sin\delta}{1+r-\sqrt{r}(r+1)\cos\delta} \right) \quad (2.51)$$

The effect of losses in optical cavities is typically characterized by their finesse. There is another measure to quantify that loss, which can be used for any type of damped oscillation. It is called the quality factor Q which measures the photon lifetime of the optical cavity mode multiplied by the oscillation frequency. It is determined by the energy loss in the cavity as a consequence of the photon lifetime. This Q factor in principle is similar to any damped oscillating system. For electrical resonance circuits, Q is the quality factor of an oscillating electrical circuit [34]. The Q factor measures the efficiency of the stored energy inside the cavity, it means that a high Q factor provides a low energy loss in comparison with the stored energy. The Q factor is defined as[35]

$$Q = \frac{2\pi \times \text{stored energy}}{\text{loss of energy per cycle}} \quad (2.52)$$

It can be written as the resonant frequency of the cavity divided by the frequency linewidth κ

$$Q = \frac{f}{\kappa} = \frac{f\mathcal{F}}{FSR} \quad (2.53)$$

Equation 2.53 illustrates that the frequency resolution of a cavity is equivalent to its finesse times the number of half-waves between the cavity mirrors [36].

2.1.5 Coupling Laser Beam to the Optical Cavity

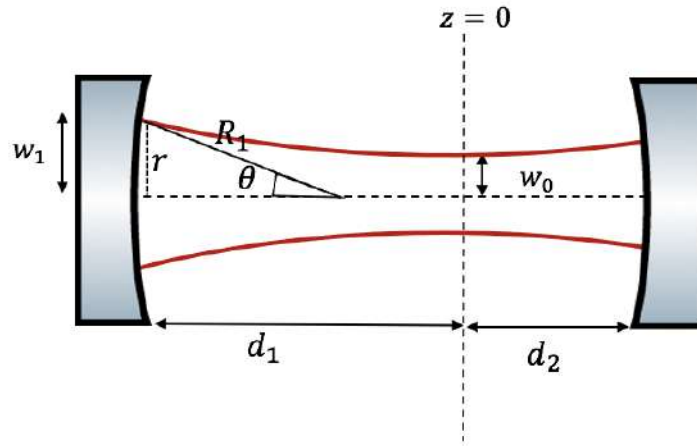


Figure 2.7: Optical cavity with length of $d_1 + d_2$, w_0 shows the smallest waist inside the cavity. The mirror on the left has a radius of curvature R_1 and the mirror on the right has a radius of curvature R_2 .

Mode matching of the input laser beam to the optical cavity mode is required for coupling. To optimally couple the laser beam to the fundamental cavity mode TEM_{00} , the radius of curvature and width must match that cavity mode at the first mirror.

The different configurations of misalignment between the laser beam with cavity mode are illustrated in Figure 2.8. Thus, it is useful to use the natural coordinates of the first cavity mirror, spherical polar coordinates with the origin at the mirror's centre as shown in Figure.2.7. The relationship between these spherical coordinates and the cylindrical polar coordinates is given below.

$$r = |R_1| \sin \theta \quad (2.54)$$

$$z = |R_1| (1 - \cos \theta) - d_1 \quad (2.55)$$

where R_1 is the radius of curvature of the first mirror and $d_1 + d_2$ is the length of the optical cavity. We need to introduce four parameters to characterize any misalignment (up to a rotation about the optic axis) between the optical cavity and the laser beam. The displacement along the optic axis between the optical cavity and laser waists denotes by δ , the angle between the direction of the laser and the cavity's optic axis refers to α ; b and c are the displacements of the laser beam's centre from the cavity's optic axis (along the axis of rotation for b and in the plane of the rotation for c).

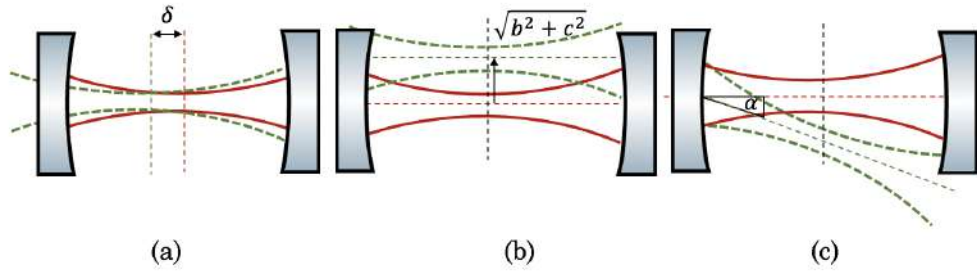


Figure 2.8: Different configurations of the misalignment between the laser beam (green dashed line) and cavity mode (red solid line).

$$r^2 = r'^2 + b^2 + c^2 - 2r'\sqrt{b^2 + c^2} \cos \gamma \quad (2.56)$$

$$z = |R_1| (1 - \cos \theta) - d_1 + \delta \quad (2.57)$$

with:

$$\begin{aligned}
r' = R_1^2 & (\sin^2\theta \cos^2\phi + \sin^2\theta \sin^2\phi \cos^2\alpha) \\
& - 2|R_1| \sin\alpha \cos\alpha \sin\theta \sin\phi (|R_1|(1 - \cos\theta) + \delta) \\
& + \sin^2\alpha (|R_1|(1 - \cos\theta) + \delta)^2
\end{aligned} \tag{2.58}$$

$$\gamma = \phi - \arctan(c/b) \tag{2.59}$$

Examples of misalignment with just one non-zero parameter are shown in Figure 2.8. It shows the laser beam and cavity mode waists are mismatched along the optic axis in (a), the laser beam is not well matched due to its displacement away from the centre of the cavity's optic axis in (b) and undergoing an angle α in (c).

All these types of misalignment between the two will lead to a couple of higher-order modes. Laguerre-Gaussian modes in one dimension form a complete basis and any axially symmetric function can be entirely described as a sum of these modes.

$$\psi_{p,l}(r) = \sum_{p=0}^{\infty} \sum_{l=0}^{\infty} C_{p,l} \sqrt{\frac{p!}{(p+l)!}} L_p^l(2r^2) (\sqrt{2r})^{|l|} e^{-r^2} \tag{2.60}$$

Normalized Laguerre-Gaussian modes as in Equation 2.60 yield that the sum of the modulus square of the coefficients should be one.

$$\sum_{p=0}^{\infty} \sum_{l=0}^{\infty} |C_{p,l}|^2 = 1 \tag{2.61}$$

This means that the laser beam must be aligned correctly such that it is axially symmetric along the optical axis of the cavity, thus the intensity of the

laser beam will couple to one of the cavity modes. From another point of view, if the laser is not axially symmetric along the optic axis of the cavity, being at an angle, the sum of the coupling coefficients can not be one and the intensity will not couple to the cavity fundamental mode.

Mode Matching with Two Lenses

To achieve strong coupling between the laser beam and the cavity fundamental mode, the beam width and radius of curvature must match the mode of the cavity. It is easily can be done with an arrangement of two lenses with focal lengths f_1 and f_2 as shown in Figure 2.9 such that the beam along the distance between the two lenses D has to be collimated. The distance between the second lens and the front mirror of the optical cavity must be equal to the focal length f_2 .

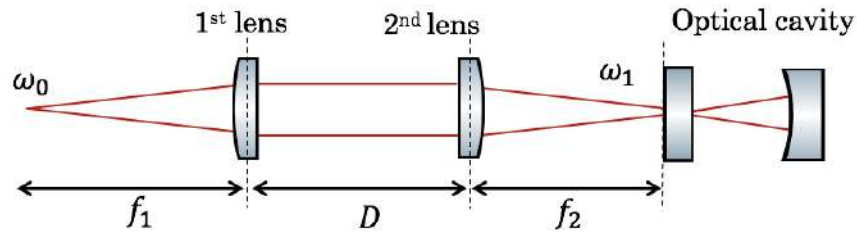


Figure 2.9: An arrangement of two lenses to achieve strong coupling between the laser and optical cavity.

The output complex radius of curvature q_1 at the first mirror can be calculated using ABCD metrics[30] as follows

$$q_1 = \frac{\frac{f_2}{f_1} q_0}{\frac{f_1}{f_2} + \left(\frac{1}{f_1} + \frac{1}{f_2} - \frac{D}{f_1 f_2} \right) q_0} \quad (2.62)$$

where q_0 is the complex radius of curvature at the initial width of the laser w_0 which is given by

$$\frac{1}{q_0} = \frac{i\lambda}{\pi w_0^2} \quad \text{and} \quad \frac{1}{q_1} = \frac{1}{R_1} + \frac{i\lambda}{\pi w_1^2} \quad (2.63)$$

By inserting the equation 2.63 into 2.62, we come up with the following constraints.

$$\frac{w_0}{w_1} = \frac{f_1}{f_2} \quad (2.64)$$

$$D = f_1 + f_2 - \frac{f_2^2}{R_1} \quad (2.65)$$

where R_1 is the radius of the first mirror in the cavity. The first mirror in our MIM cavity is a plane mirror, so $R_1 = \infty$.

2.2 Mechanical Oscillator

2.2.1 Mode Function of Mechanical Oscillator

To have an accurate description of the vibrations of the mechanical oscillator, continuum mechanics is used for calculating the eigenmodes of bulky geometries. The mechanical oscillator that is used in this thesis is a stoichiometric silicon nitride square membrane with a dimension of $1\text{mm} \times 1\text{mm} \times 50\text{nm}$ thick. A 3D membrane is restricted to 2D for simplicity, which has displacement along z within the linear response. As the laser beam passes through the membrane along the z direction, it will vibrate from its equilibrium position in the $x - y$ plane, see Figure 2.10(b).

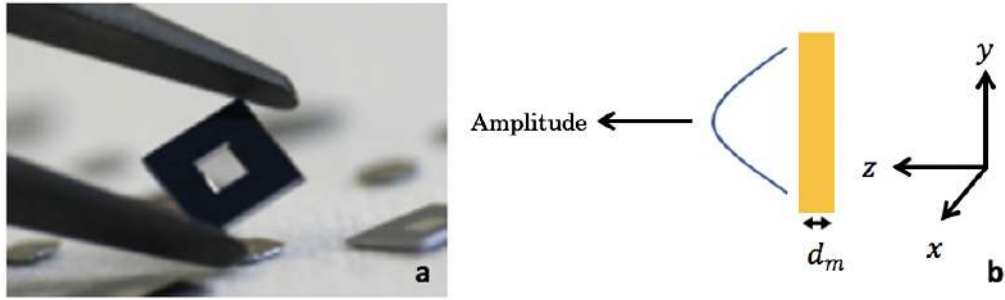


Figure 2.10: a) Commercial membrane from Norcada [1]. b) Transverse amplitude along the z direction.

The partial differential equation governing the free vibrations of the membrane is [37]

$$\frac{\partial^2 z}{\partial x^2} + \frac{\partial^2 z}{\partial y^2} = \frac{1}{c_m^2} \frac{\partial^2 z}{\partial t^2} \quad (2.66)$$

Along z is the vertical displacement of the membrane as a function of x , y coordinates in time and c_m refers to the speed of the wave propagating in the medium. The solution is presumed to be separable as [13]

$$z(x, y, t) = X(x)Y(y)T(t) \quad (2.67)$$

By inserting the solution in Equation 2.67 into 2.66, the differential equation

takes the form

$$YT \frac{d^2 X}{dx^2} + XT \frac{d^2 Y}{dy^2} = XY \frac{1}{c_m^2} \frac{d^2 T}{dt^2} \quad (2.68)$$

The left and right sides must be equal to a constant value. After multiplying the equation by $\frac{c_m^2}{XYT}$, it turns to

$$\frac{c_m^2}{X} \frac{d^2 X}{dx^2} + \frac{c_m^2}{Y} \frac{d^2 Y}{dy^2} = \frac{1}{T} \frac{d^2 T}{dt^2} = \omega_m^2 \quad (2.69)$$

The solution for the right side is a harmonic solution with an oscillating at frequency ω_m . Thus, $T(t)$ can be written as

$$T(t) = A \cos(\omega_m t) + B \sin(\omega_m t) \quad (2.70)$$

Likewise, the left side also equals to ω_m^2 , and dividing all terms by c_m^2 will leads to

$$\frac{1}{X} \frac{d^2 X}{dx^2} = -\frac{\omega_m^2}{c_m^2} - \frac{1}{Y} \frac{d^2 Y}{dy^2} = -k_x^2 \quad (2.71)$$

$$\frac{1}{Y} \frac{d^2 Y}{dy^2} = k_x^2 - \frac{\omega_m^2}{c_m^2} = -k_y^2$$

Thus, the new constant has to satisfy the condition,

$$k_x^2 + k_y^2 = \frac{\omega_m^2}{c_m^2} \quad (2.72)$$

The solution for the spatial coordinates x and y follows,

$$X = C \cos(k_x x) + D \sin(k_x x) \quad (2.73)$$

$$Y = E \cos(k_y y) + F \sin(k_y y)$$

Now, we are setting boundary conditions of all four sides of the membrane with lengths of l_x and l_y to be zero (fixed edges). We need to find the derivative of z and the second derivative of z to predict how the membrane “trampoline” behaves. The boundary conditions for vibrations of the membrane are

$z(x, 0, t) = z(0, y, t) = 0$ and $z(l_x, y, t) = z(x, l_y, t) = 0$. At $t = 0$ the membrane has an initial displacement and is released with zero velocity $z(x, y, 0)$. Applying these conditions leads to

$$k_x = \frac{i\pi}{l_x} \quad \text{and} \quad k_y = \frac{j\pi}{l_y} \quad (2.74)$$

where i and j are mode numbers (integers). For square membrane, $l_x = l_y = l_m$ and the oscillation eigenfrequencies are given by

$$\omega_m = c_m \pi \sqrt{\frac{i^2 + j^2}{l_m^2}} \quad (2.75)$$

The frequency also can be written as

$$f_m = \frac{c_m}{2} \sqrt{\frac{i^2 + j^2}{l_m^2}} \quad (2.76)$$

The speed of the wave is defined in terms of tensile stress \mathcal{T} and the density of the membrane ρ_m as

$$c_m = \sqrt{\frac{\mathcal{T}}{\rho_m}} \quad (2.77)$$

The solution of the wave equation for the selected boundary conditions is harmonic and the mode function gives the general solution for the motion as

$$z_{ij}(x, y, t) = \sum_{i=1}^{\infty} \sum_{j=1}^{\infty} [A_{ij} \cos(\omega_{ij}t) + B_{ij} \sin(\omega_{ij}t)] \sin\left(\frac{i\pi x}{l_x}\right) \sin\left(\frac{j\pi y}{l_y}\right) \quad (2.78)$$

where A_{ij} and B_{ij} are of course the constants of motion depending on the initial conditions. At initial displacement $t = 0$, the vibrations of the square membrane are simulated by MATLAB in Figure 2.11. The mechanical mode here is similar to a simple harmonic oscillator with a single momentum and position coordinate. Thus, the potential energy of the vibrational mode of the

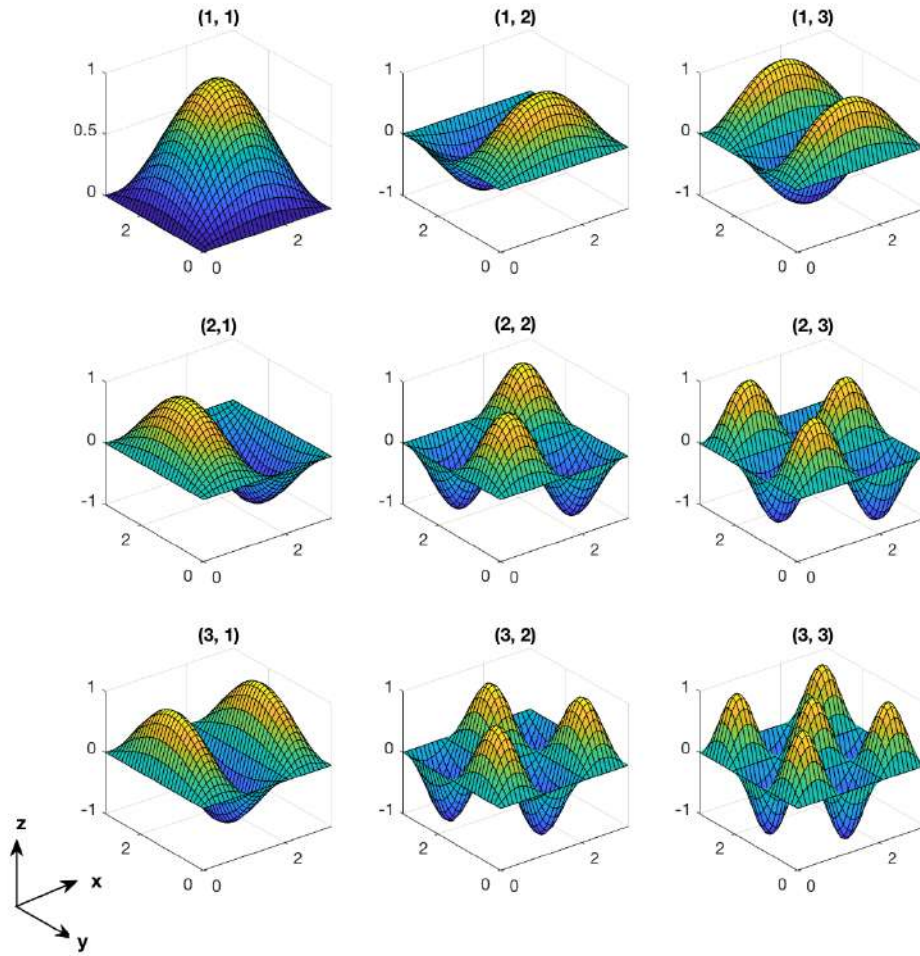


Figure 2.11: Simulated vibrations of the square membrane with different mode numbers (i,j) .

square membrane is given by

$$E_{pot}(t) = \frac{1}{2} \int_{l_m} \int_{l_m} \int_{d_m} z_{ij}^2 \omega_m^2 \rho_m dx dy dz = \frac{1}{2} M \omega_m^2 x_m^2(t) \quad (2.79)$$

where d_m , $x_m(t)$ and ω_m are the thickness of the membrane, the peak displacement and the frequency of the membrane respectively. Here, $M = \frac{1}{4} l_m^2 d_m \rho_m$ is the effective mass of the oscillator which is defined as 1/4 of its physical mass.

2.2.2 The Driven Damped Oscillator

There are always external forces as a function of time $F(t)$ that affect the membrane and they may arise from collisions with surrounding gas molecules, thermal vibrations of the membrane holder, acoustic noise, and radiation pressure forces from the light field. This will cause a small displacement to the mechanical oscillator from its equilibrium position $x_m(t)$. The equation of motion for a driven damped harmonic oscillator is given by [38]

$$M\ddot{x}_m(t) + M\gamma_m\dot{x}_m(t) + M\omega_m^2x_m(t) = F(t) \quad (2.80)$$

here γ_m and ω_m are the damping rate of the oscillator and the mechanical resonance frequency in the units of rad s^{-1} respectively. $F(t)$ is an externally driven force exerted by laser light. Decomposing the driven force $F(t)$ into a Fourier series leads to

$$-M\omega^2x_m(\omega) + iM\omega\gamma_mx_m(\omega) + M\omega_m^2x_m(\omega) = F(\omega) \quad (2.81)$$

The mechanical susceptibility linearly relates the response of the oscillator to a driven external force and it is given in the frequency domain by

$$X(\omega) = \frac{x_m(\omega)}{F(\omega)} = \frac{1/M}{\omega_m^2 - \omega^2 - i\gamma_m\omega} \quad (2.82)$$

If the driven force is $F(t) = F_0 \sin(\omega t)$ with laser frequency ω , the expected solution of the oscillator on the time domain is given by

$$x_m(t) = x_0 \sin(\omega t - \phi) \quad (2.83)$$

where the amplitude and the phase are expressed as $x_0 = \frac{F_0/M}{\sqrt{(\omega_m^2 - \omega^2)^2 + \gamma_m^2\omega^2}}$ and $\phi = \arctan\left(\frac{\gamma_m\omega}{\omega_m^2 - \omega^2}\right)$ respectively.

Our mechanical oscillator or the membrane is assumed to be a weak damp-

ing oscillator. This regime requires $\gamma_m \ll \omega_m$. Thus, the amplitude of the damped oscillator can be rewritten as

$$x_m(t) = x_0 e^{-\frac{\gamma_m}{2}t} \sin\left(t \sqrt{\omega_m^2 - \gamma_m^2/4} - \phi\right) \quad (2.84)$$

The smaller damping of the mechanical oscillator increases the quality factor of the oscillator whereas more damping will decrease it. In general, the quality factor Q is defined for the membrane oscillation as

$$Q = \frac{\omega_m}{\gamma_m}. \quad (2.85)$$

Here ω_m and γ_m have dimensions of frequency. Moreover, Q can be investigated by looking at a resonator response that is extremely sharp around its resonant frequency as shown in Figure 2.12. The mechanical oscillator has efficiently stored the energy as long as it is well isolated from its environment, thus achieving high Q . On the other hand, coupled oscillator to its environment leads to a low Q factor or broad peak around its resonant frequency.

Thermal Noise of Mechanical Oscillator

When there is no external force applied to the oscillator, the damping rate of the oscillator will be zero. But lack of forces would also mean that there is no excitation of the oscillator. In reality, the environment always couples to the oscillator producing damping as well as non-zero amplitude influenced by finite temperature T_{bath} . The impact of coupling acts as a random driving force with a noise power spectral density which is given by the Fluctuation-Dissipation Theorem [39, 40].

$$S_F(\omega) = 4k_B T_{bath} \gamma_m M \quad (2.86)$$

Here $S_F(\omega)$ is single-sided power spectral density in the domain of positive angular frequencies. The Fluctuation of x_m and F are related by important parameter namely mechanical susceptibility $|X(\omega)|^2$ and it is given by

$$\begin{aligned} S_{zz}(\omega) &= |X(\omega)|^2 S_F(\omega) = \frac{4k_B T_{bath} \gamma_m}{M} \cdot \frac{1}{(\omega_m^2 - \omega^2)^2 + \gamma_m^2 \omega^2} \\ &\approx \frac{4k_B T_{bath}}{\gamma_m M \omega_m^2} \cdot \frac{1}{1 + 4(\omega_m - \omega)^2 + \gamma_m^2} \end{aligned} \quad (2.87)$$

The last approximation satisfied the condition of the weak damping regime of the oscillator which takes a Lorentzian form near resonance. The variance of thermal amplitude (thermal displacement) in a stationary system can be found by the surface integral of the noise power spectral density $S_{zz}(\omega)$ as

$$\langle x_m^2(t) \rangle_{th} = \int_0^\infty \frac{1}{\pi} S_{zz}(\omega) d\omega = \frac{k_B T_{bath}}{M \omega_m^2}. \quad (2.88)$$

The surface integral of the noise power spectral density $S_{zz}(\omega)$ is independent of γ_m and $\langle x_m^2(t) \rangle$ is coupled to the average energy from the equipartition theorem. The average of the potential energy of the oscillator is given by

$$\langle U \rangle = \frac{1}{2} k \langle x_m^2(t) \rangle_{th} = \frac{1}{2} k_B T_{bath} \quad (2.89)$$

Thus

$$\langle x_m^2(t) \rangle_{th} = \frac{k_B T_{bath}}{M \omega_m^2}. \quad (2.90)$$

where $k = \omega_m^2 M$ is the spring constant. The average of the total energy of the oscillator is given by $k_B T_{bath}$.

For example, a SiN membrane has $(1\text{mm})^2 \times 50\text{nm}$, density $\rho_m = 3170\text{kg/m}^3$, tensile stress $\mathcal{T} = 1\text{ GPa}$ results effective mass $M = 3.96 \times 10^{-11}\text{kg}$, fundamental eigenfrequency $\omega_m = 2\pi \times 397\text{kHz}$ and thermal amplitude at room temperature $x_{th} = 4\text{pm}$.

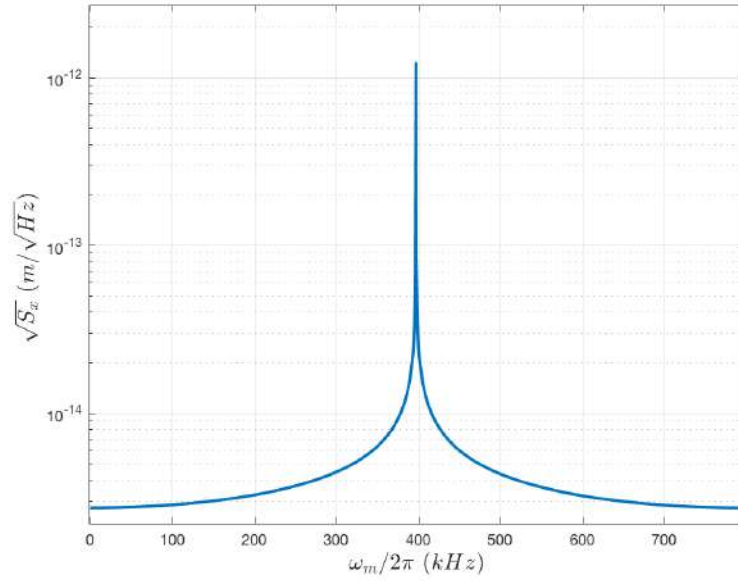


Figure 2.12: Power spectral density is plotted using Equation 2.87. Assuming that a SiN membrane at room temperature $T_{\text{bath}} = 300\text{K}$, has $\omega_m = 2\pi \times 397\text{kHz}$, $M = 3.9 \times 10^{-11}\text{kg}$ and $Q = 10^6$.

2.2.3 Quantum Mechanical Harmonic Oscillator

The Hamiltonian of the mechanical harmonic oscillator of mass M and frequency ω_m is given by [41]

$$\hat{H}_m = -\frac{\hat{p}_m^2}{2M} + \frac{1}{2}M\omega_m^2\hat{x}_m^2 \quad (2.91)$$

where \hat{x}_m and \hat{p}_m are the position and momentum operators, respectively. The quantised energy follows by solving the time-independent Schrodinger equation

$$\hat{H}_m\psi(x_m) = E_n\psi(x_m) \quad (2.92)$$

For eigenfunctions ψ_n and energies E_n . \hat{x}_m and \hat{p}_m can be expressed in terms of the ladder operators or the creation and annihilation operators \hat{b}^\dagger and \hat{b} respectively as follows

$$\hat{x}_m = \sqrt{\frac{\hbar}{2M\omega_m}}(\hat{b} + \hat{b}^\dagger) = x_{zp}(\hat{b} + \hat{b}^\dagger) \quad (2.93)$$

$$\hat{p}_m = iM\omega_m \sqrt{\frac{\hbar}{2M\omega_m}} (\hat{b}^\dagger - \hat{b}) = iM\omega_m x_{zp} (\hat{b}^\dagger - \hat{b}) \quad (2.94)$$

Here x_{zp} is the ground state amplitude and we have made use of the commutator $[\hat{x}_m, \hat{p}_m] = i\hbar$. Also, \hat{b} and \hat{b}^\dagger will obey the bosonic commutation $[\hat{b}, \hat{b}^\dagger] = 1$. Thus, we may rewrite the Hamiltonian in the form:

$$\hat{H}_m = \hbar\omega_m \left(\hat{b}^\dagger \hat{b} + \frac{1}{2} \right) \quad (2.95)$$

Equation 2.95 has the form of an eigenvalue equation. Where $\hat{N} = \hat{b}^\dagger \hat{b}$ is the number operator. In Fock space, the various eigenstates $|n\rangle$ with eigenvalues of $n = 0, 1, 2, 3, \dots$ can be written in term of the ground state $|0\rangle$ as follows

$$|n\rangle = \frac{1}{\sqrt{n!}} (\hat{b}^\dagger)^n |0\rangle \quad (2.96)$$

Where $|0\rangle$ is the lowest eigenstate for $n = 0$. Since the Fock states form an orthonormal basis, they must satisfy $\langle n|n'\rangle = \delta_{nn'}$ and $\sum_{n=0}^{\infty} |n\rangle\langle n| = 1$. The energy of n^{th} level is given by

$$E_n = \hbar\omega_m \left(n + \frac{1}{2} \right) \quad (2.97)$$

We notice that the energy levels are quantized. Also, the energy of the ground state can not be zero ($E_0 = \hbar\omega_m/2 > 0$) and it is called zero-point energy[42].

The ground state wave function in the position space represents as

$$\psi_0(x_m) = \left(\frac{1}{\pi x_{zp}^2} \right)^{1/4} \exp \left(-\frac{x_m^2}{2x_{zp}^2} \right) \quad (2.98)$$

The expectation value of the position operator $\langle x_m^2 \rangle_0$ and its variance $\langle x_m \rangle_0^2$ will lead to

$$x_{zp} = \sqrt{\langle x_m^2 \rangle_0 - \langle x_m \rangle_0^2} = \sqrt{\frac{\hbar}{2M\omega_m}} \quad (2.99)$$

which allows us to find the ground state amplitude x_{zp} where

$$\langle x_m^2 \rangle_0 = \frac{\hbar}{M\omega_m} \left(n + \frac{1}{2} \right) = \sqrt{\frac{\hbar}{2M\omega_m}} \quad (2.100)$$

$$\langle x_m \rangle_0^2 = 0 \quad (2.101)$$

For membrane with $M = 3.96 \times 10^{-11}$ kg at the center frequency $\omega_m = 2\pi \times 379$ kHz leads to $x_{zp} = 1.8$ fm. Up to this point, we looked at the behaviour of the membrane from a quantum perspective. Now, we follow the next section to discuss the membrane that sits in the middle of the optical cavity and understand the optomechanical coupling.

2.3 Optomechanics System with Membrane

2.3.1 Basic Theory of Optomechanics system

Cavity optomechanics aims to utilize mechanical interactions with the radiation pressure of laser light allowing us to control and measure the motion of mechanical oscillators with extremely high precision. It is a sufficient approach for highly sensitive position measurements which paves the way to study the quantum mechanical behaviours of mechanical oscillators. Moreover, the radiation pressure of the light can be used to cool the mechanical oscillators to their vibrational ground states [43–49] and generate mechanical oscillators in non-classical states [43, 50, 51]. To understand the effect of the optomechanical system, we introduce the basic cavity optomechanics by considering a Fabry-Perot cavity with one mirror mounted on a spring as in Figure 2.13. The frequency of the input laser beam has to be near the resonant frequency of the Fabry-Perot cavity to leak into the cavity and form a standing wave within it. The movable mirror will move when it experiences a force which is the radiation pressure of light. At the same time, the cavity's length and the

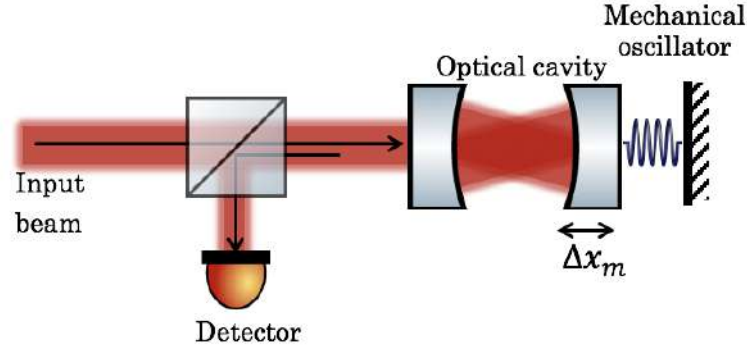


Figure 2.13: Schematic of the basic optomechanical system. Laser light can change the position of the mechanical oscillators by the radiation pressure and the motion of mechanical oscillators with extremely high precision can be measured by sending the reflected beam by a detector.

resonant frequency of the cavity will be altered when the mirror is displaced, leading to a change in the amount of light inside the cavity and its phase. The amplitude and phase of the light can be measured by looking at the reflection of the cavity in a photodetector.

2.3.2 Optomechanical Interaction Hamilton

The cavity optomechanical system illustrated in Figure 2.13 involves an optical cavity that is dispersively coupled to a mechanical oscillator. The resonance frequency of the cavity ω_c will depend on the position of the oscillator x_m [52]. The optomechanical system in quantum mechanics can be described by following Hamiltonian as [53]

$$\hat{H} = \hat{H}_m + \hat{H}_c = \hbar\omega_m \left(\hat{b}^\dagger \hat{b} + \frac{1}{2} \right) + \hbar\omega_c \left(\hat{a}^\dagger \hat{a} + \frac{1}{2} \right) \quad (2.102)$$

where $\hat{a}^\dagger \hat{a}$ is the optical modes at resonance frequency ω_c and $\hat{b}^\dagger \hat{b}$ represent the mechanical modes at resonance frequency ω_m . Assuming that oscillator displacement x_m or Δx_m is small compared to the cavity length, the resonance frequency of the cavity can be expanded by Taylor expansion to the first order

at zero displacements $\Delta x_m = 0$ as

$$\omega_c \approx \omega_c + \frac{\partial \omega_c}{\partial x_m} \Delta x_m \quad (2.103)$$

where $G = -\frac{\partial \omega_c}{\partial x_m}$ is the cavity frequency shift per mechanical displacement. By substituting $\Delta x_m = x_{zp}(\hat{b} + \hat{b}^\dagger)$ in Equation.2.103, we can rewrite the Hamiltonian as

$$\hat{H} = \hbar \omega_m \left(\hat{b}^\dagger \hat{b} + \frac{1}{2} \right) + \hbar \omega_c \left(\hat{a}^\dagger \hat{a} + \frac{1}{2} \right) - \hbar G x_{zp} (\hat{b} + \hat{b}^\dagger) \left(\hat{a}^\dagger \hat{a} + \frac{1}{2} \right) \quad (2.104)$$

It includes the unperturbed Hamiltonian and the optomechanical interaction Hamiltonian

$$\hat{H}_{opt} = -\hbar g \left[\hat{a}^\dagger \hat{a} (\hat{b} + \hat{b}^\dagger) + \frac{1}{2} (\hat{b} + \hat{b}^\dagger) \right] \quad (2.105)$$

where $g = G x_{zp}$ is the single photon optomechanical coupling system. This interaction is not a linear process at the level of a single photon. If the cavity is completely filled with \hat{N} photons, the coupling interaction will increase. The optical field can be described by a coherent state, and the annihilation operator is represented by the sum of complex number α and quantum fluctuations $\delta \hat{a}$ around the amplitude

$$\hat{a} = \alpha + \delta \hat{a} \quad (2.106)$$

substituting Equation.2.106 in 2.105 leads to

$$\hat{H}_{opt} = -\hbar g \left[(\alpha^* + \delta \hat{a}^\dagger) (\alpha + \delta \hat{a}) (\hat{b}^\dagger + \hat{b}) + \frac{1}{2} (\hat{b} + \hat{b}^\dagger) \right] \quad (2.107)$$

$$\hat{H}_{opt} = -\hbar g \left[(|\alpha|^2 + \alpha^* \delta \hat{a} + \delta \hat{a}^\dagger \alpha + \delta \hat{a}^\dagger \delta \hat{a}) (\hat{b}^\dagger + \hat{b}) + \frac{1}{2} (\hat{b} + \hat{b}^\dagger) \right] \quad (2.108)$$

where $|\alpha| = \sqrt{\hat{N}}$ is a constant that causes an offset in the mechanical oscillator's equilibrium position due to radiation pressure force. The small fluctuation in quadratic term $\delta \hat{a}^\dagger \delta \hat{a}$ is ignored. Thus, the interaction Hamiltonian is

linearized as following

$$\hat{H}_{opt} = -\hbar g \sqrt{\hat{N}} (\delta\hat{a} + \delta\hat{a}^\dagger) (\hat{b}^\dagger + \hat{b}) \quad (2.109)$$

we see that the fluctuations of the light field $\delta\hat{a}$ couple to the mechanical state \hat{b} and the coupling is enhanced by the square root of the number of photons in the cavity, $g\sqrt{\hat{N}}$.

Resolving the cavity frequency shift in the strong coupling regime where ($g/\kappa > 1$) would allow us to observe quantum nonlinear dynamics at a single photon-phonon level such as observation of mechanical quantum jumps [52]. However, the regime where ($g \ll \kappa$) is operated in solid state mechanical resonators experiments [43, 54–57]. The strong coupling regime only achieved for cold atoms experiments [58, 59]. However, It is essential to note from Equation 2.108 that a large cavity photon number is sufficient for reaching a high sensitivity to mechanical zero-point motion in the measurement of the reflected beam from the cavity.

2.4 Membrane in Asymmetric Optical Cavity

The model described in the previous section does not accurately describe the situation where a transparent membrane is placed in the middle of a cavity. While the essence of the optomechanical coupling remains the same, it is not the mirror that moves and changes the resonance frequency via the cavity length, but the position of the partially reflecting membrane. Here, the influence of that position is analysed. Specifically, the case of an asymmetric cavity is discussed, where the front mirror has a lower reflectivity than the back mirror. Each optical element in the optomechanical system can be described as a beam splitter. Two light waves enter (one going forward, one going backwards), and two light waves exit. All we need to describe these four waves

are the four complex amplitudes. Ignoring additional phase shifts, the relation

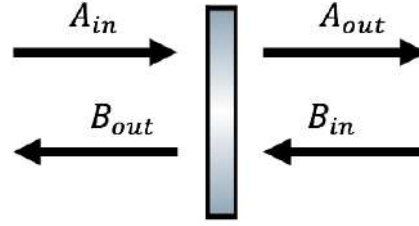


Figure 2.14: Optical element with the incident, transmitted and reflected light fields.

between inputs and outputs is given by a beam splitter matrix of the form [60]

$$\begin{pmatrix} A_{out} \\ B_{out} \end{pmatrix} = \begin{pmatrix} t & r' \\ r & t' \end{pmatrix} \begin{pmatrix} A_{in} \\ B_{in} \end{pmatrix} = \begin{pmatrix} \cos\theta & i\sin\theta \\ i\sin\theta & \cos\theta \end{pmatrix} \begin{pmatrix} A_{in} \\ B_{in} \end{pmatrix} \quad (2.110)$$

where r, r' and t, t' are reflection and transmission amplitudes that link the forward and backward travelling complex field amplitudes before (A_{in} and B_{in}) and after (A_{out} and B_{out}). We assume that the light is originally sent from the left and if the light at A_{out} goes through further optical elements which cause the incoming light to be reflected back. This will include a phase shift due to the optical path length to the next optical element and back, but also everything that happens due to the combination of further optical elements. For now, and in analogy to impedance transformations on transmission lines, we can describe that all by an effective, complex reflection coefficient Z' , such that

$$B_{in} = Z' A_{out} \quad (2.111)$$

Therefore, we have a resulting transmission coefficient for the optical element of

$$\begin{aligned}
A_{out} &= tA_{in} + r'B_{in} = tA_{in} + r'Z'A_{out} \\
&\Rightarrow A_{out}(1 - r'Z') = tA_{in} \\
&\Rightarrow Y = \frac{A_{out}}{A_{in}} = \frac{t}{1 - r'Z'}
\end{aligned} \tag{2.112}$$

Which also follows a resulting reflection coefficient for the optical element of

$$\begin{aligned}
B_{out} &= rA_{in} + t'B_{in} = rA_{in} + t'Z'A_{out} \\
&\Rightarrow B_{out} = rA_{in} + t'Z'\frac{t}{1 - r'Z'}A_{in} \\
&\Rightarrow Z = \frac{B_{out}}{A_{in}} = r + \frac{tt'Z'}{1 - r'Z'}
\end{aligned} \tag{2.113}$$

The effective reflection coefficient Z' for the next element can be calculated exactly in the same way. But we must also include the extra phase shift that arises from twice the optical path length to that element (light travels back and forth), as well as any losses that we want to describe.

For an optomechanical system where a thin dielectric membrane sits in the middle of the optical cavity, we can introduce field amplitudes for all inputs and outputs as in the Figure 2.15.

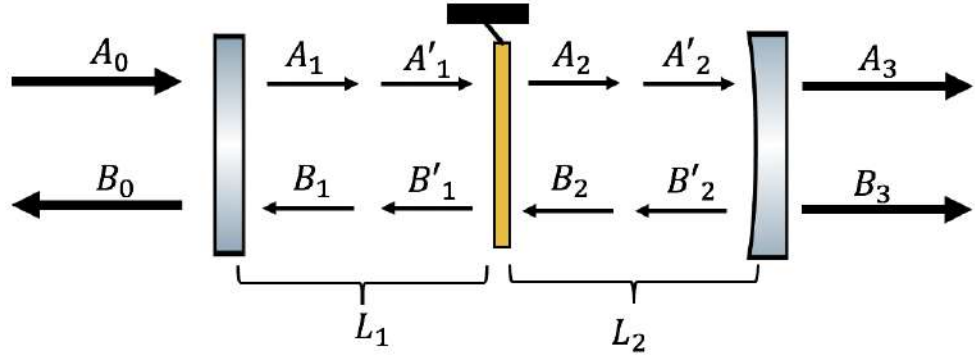


Figure 2.15: A schematic representation of the membrane in the middle of the optical cavity. A thin dielectric membrane locates at Δx_m along the optical axis of the cavity. It divides the length of the cavity into two, on the left L_1 and on the right L_2 . A_0, B_0, A_3, B_3 are the incident, reflected, transmitted fields. $A_1, A'_1, A_2, A'_2, B_1, B'_1, B_2, B'_2$ are circulating fields.

At each element (mirror, membrane, mirror), the two respective outputs

(top right and bottom left) can be calculated from the respective input (top left) by using effective transmission and reflection coefficients.

$$\begin{aligned} A_1 &= Y_1 A_0 & A_2 &= Y_2 A'_1 & A_3 &= Y_3 A'_2 \\ B_0 &= Z_1 A_0 & B'_1 &= Z_2 A'_1 & B'_2 &= Z_3 A'_2 \end{aligned} \quad (2.114)$$

The distances between the three elements are the lengths L_1 and L_2 , and we use the relations

$$\begin{aligned} A'_1 &= \eta_1 A_1 e^{ikL_1} & A'_2 &= \eta_2 A_2 e^{ikL_2} \\ B_1 &= \eta_1 B'_1 e^{ikL_1} & B_2 &= \eta_2 B'_2 e^{ikL_2} \end{aligned} \quad (2.115)$$

to include the optical delays and losses from scattering and diffraction that are produced by unstable modes. The relevant ratios of amplitudes on the right-hand side of the elements are then given by

$$\begin{aligned} Z'_1 &= \frac{B_1}{A_1} = \frac{\eta_1 e^{ikL_1}}{\eta_1^{-1} e^{-ikL_1}} \frac{B'_1}{A'_1} = \eta_1^2 e^{2ikL_1} Z_2 \\ Z'_2 &= \frac{B_2}{A_2} = \frac{\eta_2 e^{ikL_2}}{\eta_2^{-1} e^{-ikL_2}} \frac{B'_2}{A'_2} = \eta_2^2 e^{2ikL_2} Z_3 \end{aligned} \quad (2.116)$$

Since there is no fourth element and thus no light at the return input

$$Z'_3 = \frac{B_3}{A_3} = 0 \quad (2.117)$$

Now, the overall reflection and transmission can be calculated using nested expressions. To describe the behaviour of each element, we use beam splitter “mixing” angles α , β , and γ instead of θ . For the first element, we have

$$\begin{aligned} Y_1 &= \frac{\cos \alpha}{(1 - i \sin \alpha Z'_1)} = \frac{\cos \alpha}{(1 - i \sin \alpha \eta_1^2 e^{2ikL_1} Z_2)} \\ Z_1 &= i \sin \alpha + \frac{\cos^2 \alpha Z'_1}{(1 - i \sin \alpha Z'_1)} = i \sin' \alpha + \frac{\cos^2 \alpha \eta_1^2 e^{2ikL_1} Z_2}{(1 - i \sin \alpha \eta_1^2 e^{2ikL_1} Z_2)} \end{aligned} \quad (2.118)$$

This can be expressed using the results for the second element

$$\begin{aligned}
 Y_2 &= \frac{\cos \beta}{(1 - i \sin \beta Z'_2)} = \frac{\cos \beta}{(1 - i \sin \beta \eta_2^2 e^{2ikL_2} Z_3)} \\
 Z_2 &= i \sin \beta + \frac{\cos^2 \beta Z'_2}{(1 - i \sin \beta Z'_2)} = i \sin \beta + \frac{\cos^2 \beta \eta_2^2 e^{2ikL_2} Z_3}{(1 - i \sin \beta \eta_2^2 e^{2ikL_2} Z_3)}
 \end{aligned} \tag{2.119}$$

And that can be expressed using the result for the third element, which is reduced to that of a simple beam splitter

$$\begin{aligned}
 Y_3 &= \frac{\cos \gamma}{(1 - i \sin \gamma Z'_3)} = \cos \gamma \\
 Z_3 &= i \sin \gamma + \frac{\cos^2 \gamma Z'_3}{(1 - i \sin \gamma Z'_3)} = i \sin \gamma
 \end{aligned} \tag{2.120}$$

Note that the total reflection coefficient is given by that of the first mirror

$$Z = \frac{B_0}{A_0} = Z_1 \tag{2.121}$$

But the total transmission coefficient is given by

$$Y = \frac{A_3}{A_0} = \frac{A_1 A'_1 A_2 A'_2 A_3}{A_0 A_1 A'_1 A_2 A'_2} = Y_1 \eta_1 e^{ikL_1} Y_2 \eta_2 e^{ikL_2} Y_3 \tag{2.122}$$

The membrane divides the optical cavity into two sub-cavities of lengths dependent upon the membrane displacement Δx_m and back mirror displacement Δx_c as follows

$$\begin{aligned}
 L_1 &= L_{front} + \Delta x_m \\
 L_2 &= L_{back} - \Delta x_m + \Delta x_c
 \end{aligned} \tag{2.123}$$

To calculate the spectra that we see, we need to relate the variables here to the real parameters. Laser frequency f affects the wavenumber

$$k = \frac{2\pi f}{c} = \frac{2\pi(f + \Delta f)}{c} = \frac{2\pi}{\lambda} + \frac{2\pi \Delta f}{c} \tag{2.124}$$

The beam splitter angles are given by the reflectivities (intensity coefficients)

$$\begin{aligned}\alpha &= \arcsin\sqrt{r_1} \\ \beta &= \arcsin\sqrt{r_2} \\ \gamma &= \arcsin\sqrt{r_3}\end{aligned}\tag{2.125}$$

where r_1 , r_2 and r_3 are the reflectivity of the front, membrane and back mirror respectively. In our optomechanical system with a planar front mirror, we disregard absorption and scattering losses but consider an efficiency $\eta_1 < 1$ due to the dominating optical instability of the plane parallel sub-cavity, which depends strongly on the parallel alignment of the membrane and front mirror. We assume $\eta_2 = 1$, i.e. no further losses in the back cavity other than the transmission through the back mirror.

The explicit expression for the cavity's reflection coefficient Z_1 becomes

$$Z_1 = \frac{r_1 (r_2 r_3 e^{2ikL_2} - 1) + \eta_1 (r_3 e^{2ik(L_1+L_2)} - r_2 e^{2ikL_1})}{(r_2 r_3 e^{2ikL_2} - 1) + \eta_1 r_1 (r_3 e^{2ik(L_1+L_2)} - r_2 e^{2ikL_1})}\tag{2.126}$$

The total reflection coefficient of the system is just the effective reflection coefficient Z_1 of the first element, while the total transmission is given by the product of all effective transmission coefficients Y , the total propagation phase and all single-pass loss factors.

The plot in Figure 2.16 shows the total reflection coefficient scanned Δx_c in meters for 5 fixed values of Δx_m (steps of to 100 nm). The resonance peak has the same finesse because losses are fixed, assuming that η_1 and η_2 are 0.7 and 1 respectively.

Different values of membrane parallel alignment η_1 lead to an increase (sharp resonance) or decrease (broad resonance) in losses between the two sub cavities at various membrane positions Δx_m and that is shown in Figure 2.17.

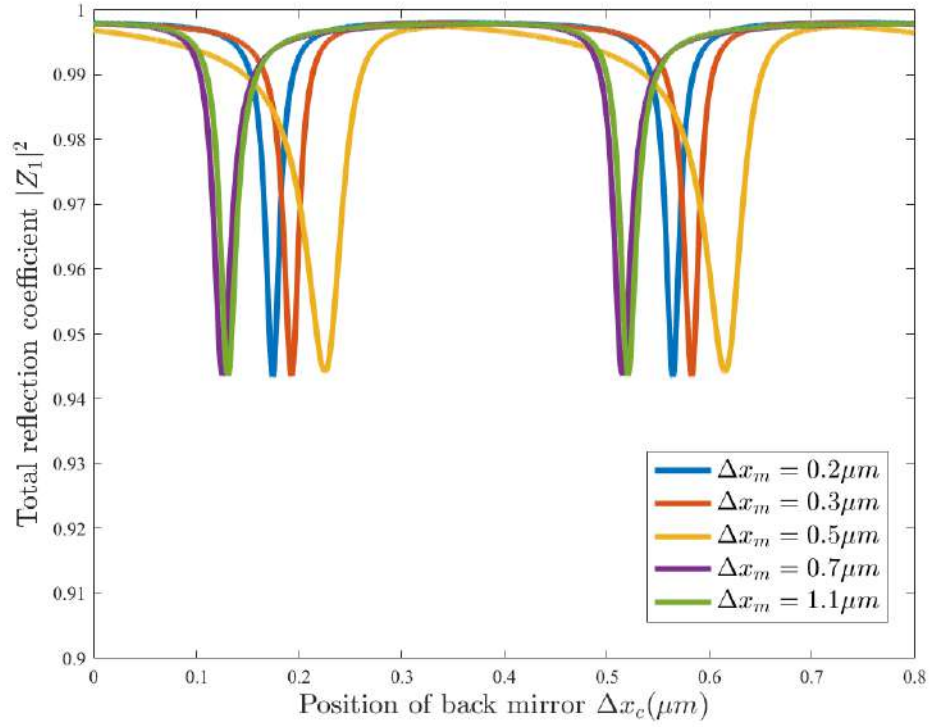


Figure 2.16: The total reflection coefficient is plotted for a cavity has a length of $L_1 = L_2 = 15\text{mm}$ with wavelength $\lambda = 780\text{nm}$ and reflectivities of $r_1 = 0.99$, $r_2 = 0.995$, $r_m = 0.22$ at different values of Δx_m where $\eta_1^2 = 0.7$.

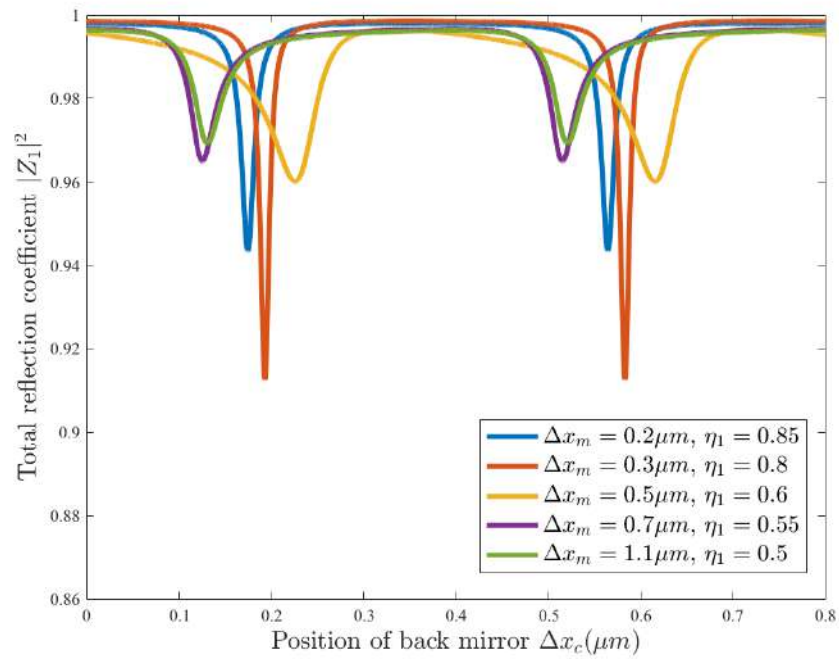


Figure 2.17: The total reflection coefficient is plotted with the same parameters as in Figure.2.16 but for several values of η_1^2 at different membrane positions Δx_m .

Figure 2.18 shows the theoretical cavity response according to this model as a function of membrane position Δx_m for tuned laser frequency as well as for tuned back mirror position Δx_c . The former might be intuitively understood in terms of decreasing and increasing mode energies of the two sub-cavities with different finesse. Their coupling by transmission through the membrane leads to avoided crossings. As a result, resonant frequencies as well as cavity finesse oscillate as a function of membrane displacement Δx_m . This behaviour corresponds to the maximum field intensity alternating between both sub-cavities. For the case of tuned mirror position, one should note that the mirror position does not influence the length of the front sub-cavity and is thus not equivalent to tuning the laser frequency. Here, the apparent linewidth of resonance is determined by a mixture of cavity decay rate and tuning behaviour. This case will be used for comparison with experimental data that will be shown in Chapter 5.

The strongest dispersive coupling to the membrane occurs when the back sub-cavity is resonant, while the front sub-cavity is anti-resonant ($L_{front} = \lambda/4 + m\lambda/2$ and $L_{back} + \Delta x_c = n\lambda/2$ with an integer m, n for the same sign of all r_i), see indicating arrow in Figure 2.18(a). Here, the first-order expansion of the effective reflection coefficient becomes

$$Z_1 \approx \frac{r_1(r_2r_3 - 1) + \eta_1(r_3 - r_2)}{(r_2r_3 - 1) + r_1\eta_1(r_3 - r_2)} + 4\pi i \frac{(r_1^2 - 1)r_2\eta_1(2r_2r_3 - 1 - r_3^2)}{((r_2r_3 - 1) + r_1\eta_1(r_3 - r_2))^2} \frac{\Delta x_m}{\lambda}, \quad (2.127)$$

where all amplitude reflection coefficients $r_{1,2,3}$ and η_1 are real. One should note here that the reflected intensity will reach a minimum on resonance and may completely vanish, i.e. lead to $Z_1(\Delta x_m = 0) = 0$. This impedance-matching condition is given by

$$r_1 = \frac{\eta_1(r_2 - r_3)}{r_2r_3 - 1}, \quad (2.128)$$

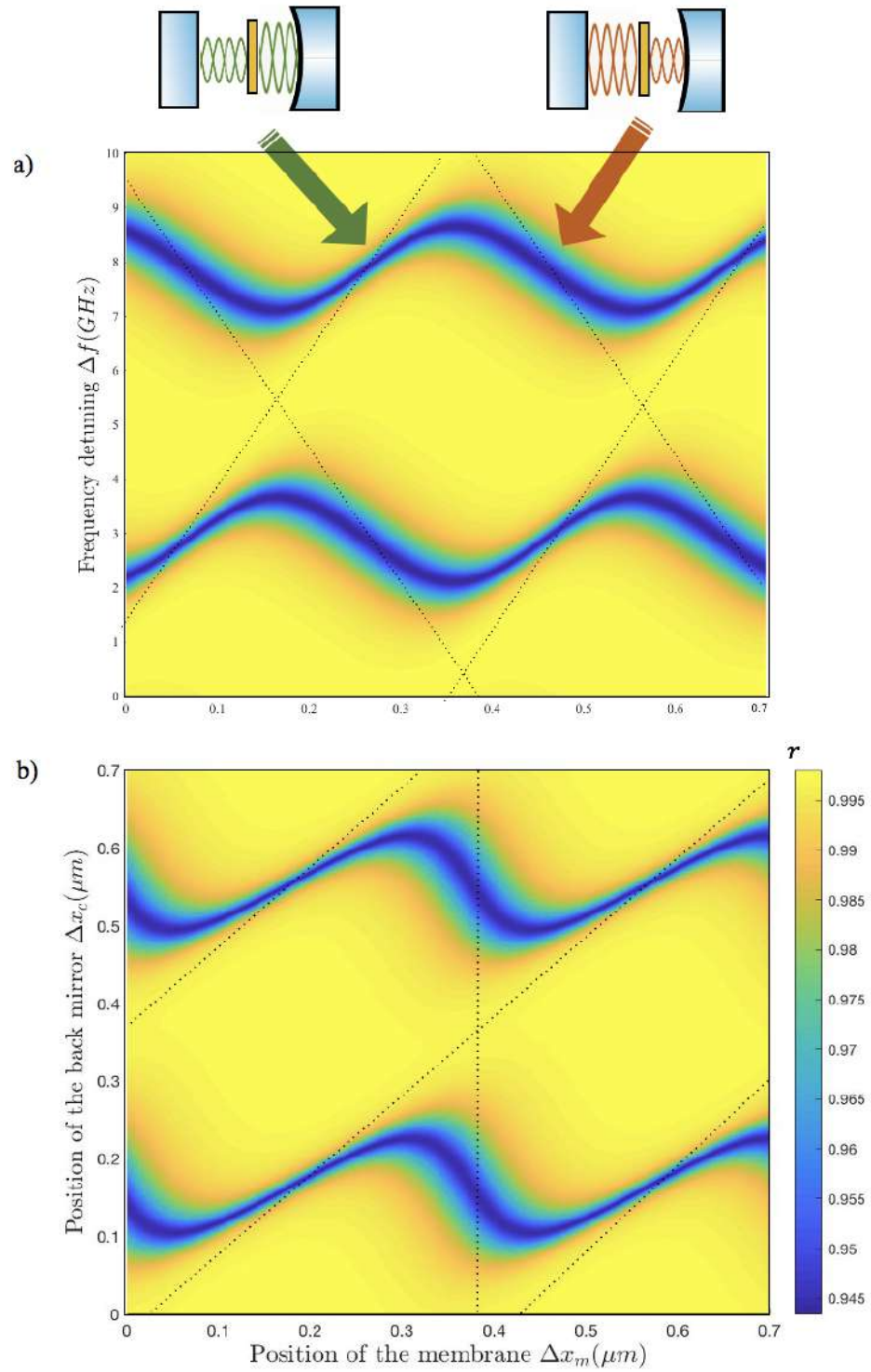


Figure 2.18: Theoretical simulations show the total reflectance of the resonator as a function of the membrane position and laser frequency (a) or back mirror position (b). For clarity, an exaggerated optical instability loss with $\eta_1 = 0.7$ was used, resulting in low-finesse modes. Dashed lines indicate loss-less sub-cavity modes for 100% membrane reflectivity.

which reduces to

$$r_1 \approx \eta_1 \quad (2.129)$$

for highly reflective back mirrors with $r_3 \approx 1$. However, the signal response is entirely given by the imaginary part of the expression in Equation (2.127) that also corresponds fully to the light quadrature, which we will discuss in the following section.

2.5 Polarization States of the Light

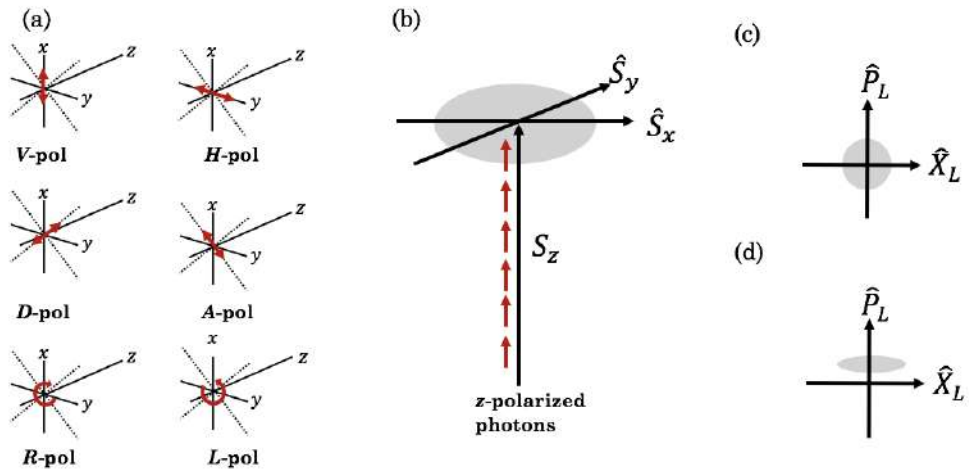


Figure 2.19: a) Types of photons polarization in a real space presentation for light travelling along the z -axis. Red arrows indicate the direction of the electric field oscillation. b) Polarisation is represented on the Poincaré sphere. Circularly polarized photons along S_z (here S_z is a classical component when we consider many photons in a pulse) and the grey disc represents Heisenberg uncertainty of the transverse components \hat{S}_x and \hat{S}_y . c) Top view of (b) where the field quadrature \hat{P}_L and \hat{X}_L are identical d) Squeezing of one quadrature.

The experiment in this thesis involves laser interacting with a mechanical oscillator via a polarization interferometer and it turns out that laser light polarization is relevant to the quantum variable. The polarization states of the light can be described by the Stokes operators. The quantum mechanical Stokes operators follow the definitions for photon flux differences and a right-handed coordinate system

$$\hat{S}_x = \frac{c}{2}(\hat{n}_H - \hat{n}_V) \quad (2.130)$$

$$\hat{S}_y = \frac{c}{2}(\hat{n}_D - \hat{n}_A) \quad (2.131)$$

$$\hat{S}_z = \frac{c}{2}(\hat{n}_L - \hat{n}_R) \quad (2.132)$$

thus, it can be rewritten in terms of the annihilation and creation operators as

$$\hat{S}_x = \frac{c}{2}(\hat{a}_H^\dagger \hat{a}_H - \hat{a}_V^\dagger \hat{a}_V) \quad (2.133)$$

$$\hat{S}_y = \frac{c}{2}(\hat{a}_H^\dagger \hat{a}_V + \hat{a}_V^\dagger \hat{a}_H) \quad (2.134)$$

$$\hat{S}_z = \frac{c}{2}(i\hat{a}_V^\dagger \hat{a}_H - i\hat{a}_H^\dagger \hat{a}_V) \quad (2.135)$$

where V and H denote the two orthogonal field components in vertical and horizontal directions. We have defined the annihilation operators for the other two basis sets as

$$\hat{a}_{L,R} = (\hat{a}_H \mp i\hat{a}_V)/\sqrt{2} \quad (2.136)$$

$$\hat{a}_{D,A} = (\pm\hat{a}_H + \hat{a}_V)/\sqrt{2}, \quad (2.137)$$

where $\hat{a}_{L,R}, \hat{a}_{D,A}$, describes left/right-handed circular, linear diagonal/anti-diagonal, beam polarization, respectively. All these types of polarization are depicted in Figure 2.19(a). These Heisenberg operators for the field amplitude must obey

$$[\hat{a}_i(z), \hat{a}_j^\dagger(z')] = \delta_{i,j} \delta_z(z - z') \quad (2.138)$$

for orthogonal polarizations i, j , such that the number operators $\hat{n}_i = \hat{a}_i^\dagger \hat{a}_i$ describe linear spatial photon density and the Stokes operators describe photon flux, i.e. the rates at which photons arrive at the detector.

Observing that $\delta(t) = c\delta_z(z = ct)$, the Stokes vector components must

obey the commutation rules of the angular momentum according to

$$[\hat{S}_x(t), \hat{S}_y(t')] = i\delta(t - t')\hat{S}_z(t) \quad (2.139)$$

$$\langle \Delta \hat{S}_x \rangle \cdot \langle \Delta \hat{S}_y \rangle \geq \frac{S_z^2}{4} \quad (2.140)$$

and using circular permutation $x \rightarrow y, y \rightarrow z, z \rightarrow x$.

The total photon flux is given by

$$2\hat{S}_0 = c(\hat{n}_H + \hat{n}_V) = c(\hat{a}_H^\dagger \hat{a}_H + \hat{a}_V^\dagger \hat{a}_V). \quad (2.141)$$

If a beam is fully circularly polarized, the \hat{S}_z component of the corresponding Stokes vector measures half the photon flux. However, measurements of polarisation in another basis, for example in (A/D or H/V) basis will lead to noise which is the Heisenberg uncertainty of the transverse components \hat{S}_x and \hat{S}_y that is represented by the grey disc, see Figure 2.19(b). The reason is that a circularly polarised photon has an equal probability to be detected at either output of a polarising beam splitter, which measures if it was H or V. Measuring at a 45-degree rotated polarizer will lead to the same result unless the polarisation state is squeezed which means the noise may be smaller in the A/D measurement if it is larger in the H/V measurement, see Figure 2.19(d).

In the assumption of the impedance matching at the cavity, the reference beam that comes back is horizontally polarised and the signal beam is very weak and vertically polarised. That means, instead of having a large \hat{S}_z , we have a large positive \hat{S}_x ($n_H = A^2 \cos^2 \alpha$ and $n_V = 0$, thus $\langle \hat{S}_x \rangle = \frac{cA^2}{2} \cos^2 \alpha$ where α is the polarisation angle and A the amplitude of the electric field before the beam displacer). From the above view of the grey disk that is shown in Figure 2.19(c, d), we can define new quantum quadrature operators \hat{X}_L and

\hat{P}_L and their commutator as

$$\hat{X}_L = \frac{\hat{S}_y}{\sqrt{\langle \hat{S}_x \rangle}}, \quad \hat{P}_L = \frac{\hat{S}_z}{\sqrt{\langle \hat{S}_x \rangle}}, \quad \rightarrow [\hat{X}_L, \hat{P}_L] = i. \quad (2.142)$$

Thus, it is convenient to rewrite these Hermitian operators in terms of non-Hermitian operators \hat{a}_V^\dagger and \hat{a}_V as

$$\hat{X}_L = \frac{\hat{a}_V + \hat{a}_V^\dagger}{\sqrt{2}}, \quad \hat{P}_L = \frac{\hat{a}_V - \hat{a}_V^\dagger}{\sqrt{2}} \quad (2.143)$$

where \hat{a}_V and \hat{a}_V^\dagger are the annihilation and creation operators for photons that send to the cavity with vertical polarization. The Stokes operators can be measured by a homodyne detection which will be explained in the following section

2.6 Quantum noise

To assess the suitability of our setup for quantum optical experiments, observing and evaluating the levels of measurement noise is required. Here, the principle of the detection scheme of homodyne detection is described with the quantum noise of the light. Also, we show the entire quantum description of coherent beam propagation through the converter and we end up with an important usage of the power spectral density, which can be used for predicting the outcome of passing a noisy signal through our system.

2.6.1 Homodyne detection and quantum noise of light

A balanced homodyne detection (BHD) schematic diagram in Figure 2.20 is used for the detection of the thermal noise of the membrane. In general, it consists of a 50:50 beam splitter and two identical photodiodes PD_1 and

PD_2 . The two photodiodes are connected to an electronic circuit that takes the difference between them as an output ($i_1 - i_2$), where i_1 and i_2 are the photocurrents that are produced by PD_1 and PD_2 respectively. The balanced

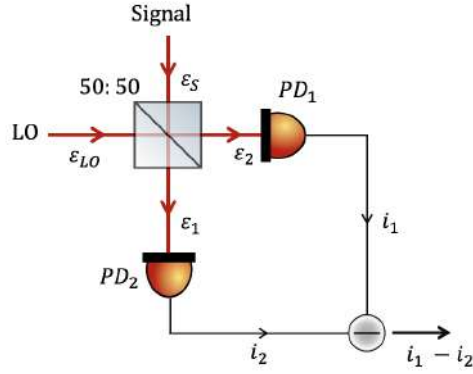


Figure 2.20: Schematic of the balanced homodyne detection.

detector has two input ports. The signal beam and local oscillator (LO) are normally generated from the same laser and each beam input is detected by one of the input ports of the balanced detector. The LO beam has the same frequency as the signal beam but with a large amplitude light wave. Let's assume signal and LO beams are interfering on the beam splitter and the output fields are ε_1 and ε_2 are given by

$$\varepsilon_1 = \frac{1}{\sqrt{2}}(\varepsilon_{LO}e^{i\phi_{LO}} + \varepsilon_S) \quad (2.144)$$

$$\varepsilon_2 = \frac{1}{\sqrt{2}}(\varepsilon_{LO}e^{i\phi_{LO}} - \varepsilon_S) \quad (2.145)$$

where ε_{LO} and ε_S are the amplitude of LO and signal beams respectively. ϕ_{LO} is the phase of LO relative to the signal beam. The LO beam is treated classically as its amplitude field is large whereas the signal beam is a weak field and must be treated quantum mechanically. Therefore, the signal beam can be represented by its two quadrature components as $\varepsilon_S = \varepsilon_S^{XL} + i\varepsilon_S^{PL}$. Thus, the output fields split into their real and imaginary parts as

$$\varepsilon_1 = \frac{1}{\sqrt{2}} [(\varepsilon_{LO} \cos \phi_{LO} + \varepsilon_S^{X_L}) + i(\varepsilon_{LO} \sin \phi_{LO} + \varepsilon_S^{P_L})] \quad (2.146)$$

$$\varepsilon_2 = \frac{1}{\sqrt{2}} [(\varepsilon_{LO} \cos \phi_{LO} - \varepsilon_S^{X_L}) + i(\varepsilon_{LO} \sin \phi_{LO} - \varepsilon_S^{P_L})] \quad (2.147)$$

The balanced homodyne detection output to the first order of ε_S is given by

$$\begin{aligned} \text{Output} &\propto i_1 - i_2 \\ &\propto \varepsilon_1 \varepsilon_1^* - \varepsilon_2 \varepsilon_2^* \\ &\propto 2\varepsilon_{LO} (\cos \phi_{LO} \varepsilon_S^{X_L} + \sin \phi_{LO} \varepsilon_S^{P_L}) \end{aligned} \quad (2.148)$$

that results from the fact that the photocurrent of the balanced detector is proportional to $|\varepsilon|^2 = \varepsilon \varepsilon^*$. The LO beam has a sensitive phase, for example for $\phi_{LO} = 0, \pi, 2\pi, \dots$, the output amplitude will be proportional to signal beam quadrature $\varepsilon_{LO} \varepsilon_S^{X_L}$, which is in phase with LO beam [61].

In a classical scenario with a blocked signal beam - or a signal beam of zero amplitude, the two signal quadratures are zero. Therefore, the measured signal will also be zero. LO intensity will be equally divided between the two photodiode inputs. That will lead to zero photocurrents ($i_1 - i_2 = 0$) which suppress all classical intensity fluctuation of LO. However, that is not correct in the quantum description according to Equation 2.148. Even though a signal field has zero intensity, it will still have a non-zero field amplitude that fluctuates around zero. These fluctuating amplitudes cause the non-zero signal output of the detector. This is because there are vacuum modes entering the signal port. Thus, the detector's output is proportional to $\varepsilon_{LO} \varepsilon^{vac}$ and it is equivalent to the photon shot noise in the LO. The interpretation is that the shot noise output with no signal presents a result of the homodyning of the

local oscillator with the vacuum field.

Quantum mechanically, the signal quadratures are described by the sum and difference of field amplitude (or photon creation and annihilation) operators for the signal field

$$\hat{X}_L = \frac{1}{\sqrt{2}} (\hat{a}_S + \hat{a}_S^\dagger), \quad (2.149)$$

$$\hat{P}_L = \frac{1}{\sqrt{2}} (\hat{a}_S - \hat{a}_S^\dagger). \quad (2.150)$$

In our experiment, we use polarisation homodyne detection. The principle is the same, but a polarising beam splitter is used. In this case, the local oscillator travels on the same path as the signal beam, but it has orthogonal polarisation. Using waveplates with the converter as shown in Figure 2.21, the polarisation is rotated such that each component will be divided equally between the two outputs. But the field amplitudes at the outputs will show interference of the two input amplitudes.

Let's assume the LO is horizontally polarised (H) and the signal beam is vertically polarized (V). Using the usual beam splitter matrix, the two output amplitudes that reach the two photodiodes will be described by the operators

$$\hat{a}_1 = \frac{\hat{a}_H + i\hat{a}_V}{\sqrt{2}}, \quad (2.151)$$

$$\hat{a}_2 = \frac{i\hat{a}_H + \hat{a}_V}{\sqrt{2}}, \quad (2.152)$$

and corresponding conjugate operators.

The measurements of the detected intensities or photon fluxes are de-

scribed by the operators

$$\phi_1 = c \hat{a}_1^\dagger \hat{a}_1, \quad (2.153)$$

$$\phi_2 = c \hat{a}_2^\dagger \hat{a}_2, \quad (2.154)$$

The intensity difference is given by

$$\phi_2 - \phi_1 = c \left(\hat{a}_2^\dagger \hat{a}_2 - \hat{a}_1^\dagger \hat{a}_1 \right) \quad (2.155)$$

$$= c \left(\frac{-i \hat{a}_H^\dagger + \hat{a}_V^\dagger}{\sqrt{2}} \frac{i \hat{a}_H + \hat{a}_V}{\sqrt{2}} - \frac{\hat{a}_H^\dagger - i \hat{a}_V^\dagger}{\sqrt{2}} \frac{\hat{a}_H + i \hat{a}_V}{\sqrt{2}} \right) \quad (2.156)$$

$$= c \left(i \hat{a}_V^\dagger \hat{a}_H - i \hat{a}_H^\dagger \hat{a}_V \right) \quad (2.157)$$

$$= 2 \hat{S}_z. \quad (2.158)$$

Therefore, the detector measures the operator \hat{S}_z , i.e. how circularly polarized the input beam is.

2.6.2 Noise Readout From the Polarization Converter

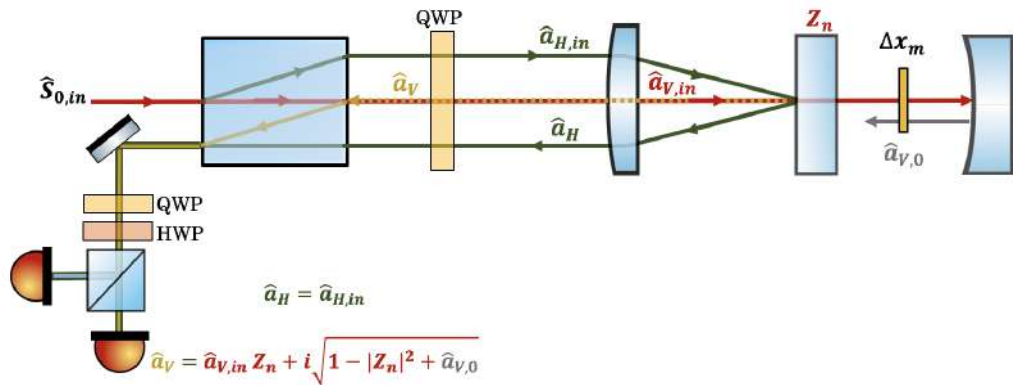


Figure 2.21: Schematic of the polarization of the beam in the converter. QWP refers to a quarter-wave plate and HWP refers to a half-wave plate .

We illuminate the converter with a coherent, linearly polarized input beam

under an angle α , and the input polarization is described by

$$\langle \hat{a}_{\text{H,in}} \rangle = A \cos \alpha, \quad \langle \hat{a}_{\text{V,in}} \rangle = A \sin \alpha \quad (2.159)$$

and thus

$$\langle \hat{S}_{z,\text{in}} \rangle = 0, \quad (2.160)$$

$$\langle \hat{S}_{y,\text{in}} \rangle = \langle \hat{S}_{0,\text{in}} \rangle \sin 2\alpha \quad (2.161)$$

$$\langle \hat{S}_{x,\text{in}} \rangle = \langle \hat{S}_{0,\text{in}} \rangle (\cos^2 \alpha - \sin^2 \alpha) \quad (2.162)$$

Here $\langle \hat{S}_{x,\text{in}} \rangle$ has a non-zero mean value due to the change in the balance between reference (H) and signal (V) beams.

The effect of the converter is described as an effective beam splitter acting on the partially entering signal field, while the reference beam is fully reflected because it is not aligned with respect to the optical axis of the cavity. Including the exchange of horizontal and vertical polarisations, the detected field is thus given by

$$\hat{a}_{\text{H}} = \hat{a}_{\text{H,in}} \quad \text{and} \quad \hat{a}_{\text{V}} = Z_1 \hat{a}_{\text{V,in}} + i\sqrt{1 - |Z_1|^2} \hat{a}_{\text{V},0}, \quad (2.163)$$

where $\hat{a}_{\text{V},0}$ is the fictitious vacuum mode that's required to describe the whole system as a single beams splitter. We assume impedance matching and resonance with the cavity such that $Z_1 \approx i\chi\Delta x_m$. We also assume $\langle \Delta x_m \rangle = 0$ and the coupling to membrane motion to be small enough such that $|Z_1|^2 \ll 1$. As a consequence, the measurement is described by

$$\hat{S}_z \approx \frac{c}{2} \left(\chi \Delta x_m (\hat{a}_{\text{V,in}}^\dagger \hat{a}_{\text{H,in}} + \hat{a}_{\text{H,in}}^\dagger \hat{a}_{\text{V,in}}) + (\hat{a}_{\text{V},0}^\dagger \hat{a}_{\text{H,in}} + \hat{a}_{\text{H,in}}^\dagger \hat{a}_{\text{V},0}) \right) \quad (2.164)$$

We write the field operators as a sum of expectation value (the classical field amplitude) and a different operator to describe the quantum fluctuations of those amplitudes

$$\hat{a}_{\text{H,V}} = \langle \hat{a}_{\text{H,V}} \rangle + \delta \hat{a}_{\text{H,V}} \quad (2.165)$$

$$\begin{aligned} \hat{S}_z \approx & \frac{c}{2} \left(2A^2 \chi \Delta x_m \cos \alpha \sin \alpha \right. \\ & + A \chi \Delta x_m \cos \alpha (\delta \hat{a}_{\text{V,in}}^\dagger + \delta \hat{a}_{\text{V,in}}) \\ & + A \chi \Delta x_m \sin \alpha (\delta \hat{a}_{\text{H,in}} + \delta \hat{a}_{\text{H,in}}^\dagger) \\ & + \chi \Delta x_m \delta \hat{a}_{\text{V,in}}^\dagger \delta \hat{a}_{\text{H,in}} + \chi \Delta x_m \delta \hat{a}_{\text{H,in}}^\dagger \delta \hat{a}_{\text{V,in}} \\ & + A \cos \alpha (\hat{a}_{\text{V},0}^\dagger + \hat{a}_{\text{V},0}) \\ & \left. + \hat{a}_{\text{V},0}^\dagger \delta \hat{a}_{\text{H,in}} + \delta \hat{a}_{\text{H,in}}^\dagger \hat{a}_{\text{V},0} \right) \end{aligned}$$

neglecting all higher-order terms results in

$$\hat{S}_z(t) \approx \eta_d \langle \hat{S}_{y,\text{in}} \rangle \chi \Delta x_m(t) + \sqrt{\eta_d \frac{c}{2} \langle \hat{S}_{0,\text{in}} \rangle} \cos \alpha (\hat{a}_{\text{V},0}^\dagger(ct) + \hat{a}_{\text{V},0}(ct)), \quad (2.166)$$

where we included a detection loss η_d which reduces the photon flux but replenishes the vacuum field. The first term measures the membrane displacement while the second term arises from the co-measured field quadrature of the vertically polarised vacuum field, which leads to white photon shot noise. This signal is measured with a frequency-dependent electronic gain G_e such that $U(t) = G_e S_z(t)$. Since membrane position and vacuum field are uncorrelated, the auto-correlation function $R_{UU}(\tau) = G_e^2 \langle \hat{S}_z(t) \hat{S}_z(t + \tau) \rangle$ of the measured

voltage is given by

$$\begin{aligned}
R_{UU}(\tau) &= G_e^2 \langle \hat{S}_z(t) \hat{S}_z(t + \tau) \rangle = G_e^2 \eta_d^2 \langle \hat{S}_{y,\text{in}} \rangle^2 \chi^2 \langle \Delta x_m(t) \Delta x_m(t + \tau) \rangle \\
&\quad + G_e^2 \eta_d \cos^2 \alpha \frac{c}{2} \langle \hat{S}_{0,\text{in}} \rangle \langle \hat{a}_{V,0}^\dagger(ct) \hat{a}_{V,0}^\dagger(ct + c\tau) \rangle \\
&\quad + G_e^2 \eta_d \cos^2 \alpha \frac{c}{2} \langle \hat{S}_{0,\text{in}} \rangle \langle \hat{a}_{V,0}(ct) \hat{a}_{V,0}^\dagger(ct + c\tau) \rangle \\
&\quad + G_e^2 \eta_d \cos^2 \alpha \frac{c}{2} \langle \hat{S}_{0,\text{in}} \rangle \langle \hat{a}_{V,0}^\dagger(ct) \hat{a}_{V,0}(ct + c\tau) \rangle \\
&\quad + G_e^2 \eta_d \cos^2 \alpha \frac{c}{2} \langle \hat{S}_{0,\text{in}} \rangle \langle \hat{a}_{V,0}(ct) \hat{a}_{V,0}(ct + c\tau) \rangle
\end{aligned} \tag{2.167}$$

Since for the vacuum $\langle 0 | \hat{a}_{V,0}^\dagger = \hat{a}_{V,0} | 0 \rangle = 0$, this reduces to

$$\begin{aligned}
R_{UU}(\tau) &= G_e^2 \eta_d^2 \langle \hat{S}_{y,\text{in}} \rangle^2 \chi^2 \langle \Delta x_m(t) \Delta x_m(t + \tau) \rangle \\
&\quad + G_e^2 \eta_d \cos^2 \alpha \frac{c}{2} \langle \hat{S}_{0,\text{in}} \rangle \langle \hat{a}_{V,0}(ct) \hat{a}_{V,0}^\dagger(ct + c\tau) \rangle.
\end{aligned} \tag{2.168}$$

Using the commutator $[\hat{a}, \hat{a}^\dagger] = \delta_z(ct - (ct + c\tau))$ leads to

$$\begin{aligned}
R_{UU}(\tau) &= G_e^2 \eta_d^2 \langle \hat{S}_{y,\text{in}} \rangle^2 \chi^2 \langle \Delta x_m(t) \Delta x_m(t + \tau) \rangle \\
&\quad + G_e^2 \eta_d \cos^2 \alpha \frac{c}{2} \langle \hat{S}_{0,\text{in}} \rangle \left(\langle \hat{a}_{V,0}^\dagger(ct) \hat{a}_{V,0}(ct + c\tau) \rangle + \delta_z(c\tau) \right),
\end{aligned} \tag{2.169}$$

where the last bracket reduces again to $\delta_z(c\tau)$, because $\hat{a}_{V,0} | 0 \rangle = 0$.

$$\begin{aligned}
R_{UU}(\tau) &= G_e^2 \eta_e^2 \langle \hat{S}_{y,\text{in}} \rangle^2 \chi^2 \langle \Delta x_m(t) \Delta x_m(t + \tau) \rangle + \frac{1}{2} G_e^2 \eta_e \cos^2 \alpha \langle \hat{S}_{0,\text{in}} \rangle c \delta_z(c\tau) \\
&= G_e^2 \eta_d^2 \langle \hat{S}_{y,\text{in}} \rangle^2 \chi^2 R_{zz}(\tau) + \frac{1}{2} G_e^2 \eta_d \cos^2 \alpha \langle \hat{S}_{0,\text{in}} \rangle \delta(\tau)
\end{aligned} \tag{2.170}$$

Here, we can introduce the auto-correlation $R_{zz}(\tau) = \langle \Delta x_m(t) \Delta x_m(t + \tau) \rangle$ of membrane motion. To calculate the spectrum of the expected noise, we can use the theorem that the power spectral density S_{UU} of a voltage signal is given by the Fourier transform of the signal's auto-correlation function R_{UU} .

Without electronic noise, the power spectral density of the measured volt-

age is given by

$$S_{UU}(f) = \int_{-\infty}^{\infty} R_{UU}(\tau) e^{-2\pi i f \tau} d\tau = G_e^2 \eta_d^2 \langle \hat{S}_{y,\text{in}} \rangle^2 \chi^2 S_{zz}(f) + \frac{1}{2} G_e^2 \eta_d \cos^2 \alpha \langle \hat{S}_{0,\text{in}} \rangle. \quad (2.171)$$

As discussed in Section 2.2.2, the power spectral density (per natural frequency) of an underdamped, thermally driven oscillator with resonant frequency f_m and energy loss rate γ_m is approximately given by

$$S_{zz}(f) = \int_{-\infty}^{\infty} R_{zz}(\tau) e^{-2\pi i f \tau} d\tau \approx \frac{k_B T}{M(2\pi f_m)^2} \frac{2\gamma_m}{16\pi^2(|f| - f_m)^2 + \gamma_m^2}, \quad (2.172)$$

where M is the effective mass taking part in the oscillation with variance

$$\langle \Delta x_m^2 \rangle = \int_{-\infty}^{\infty} S_{zz}(f) df = \frac{k_B T}{4\pi^2 M f_m^2}. \quad (2.173)$$

The power spectral density voltage of the measured S_{UU} can be detected using homodyne detection.

This chapter has described all the needed background that is used for the MIM system. Also, the quantum description of our converter is well explained and we provide the detection scheme with the converter's readout. The following chapter will show how to design a robust interferometer taking into account precise alignment.

Chapter 3

A Position to Polarization

Converter

In this chapter, we want to build an interferometer that maps the quantum mechanical properties of the laser light that comes back from the optical cavity signal beam onto the polarization of the laser beam. That has to be done in an interferometric robust way because the reference beam must not change its phase with respect to the signal beam rather than the membrane. The design of our interferometer includes a birefringent crystal, thus it is useful to show the effect of laser light polarization propagating in a birefringent crystal. The sensitive alignment of the laser beams into the optomechanical system is theoretically discussed considering the optimum overlap between the reference and the signal beam to form the interferometer.

3.1 Polarization In A Birefringent Crystal

The speed of monochromatic light that passes through a Glass is the same in all directions in isotropic materials which is characterized by a single index of refraction. For anisotropic materials, the speed of light is different along

different axes within the material as well as the index of refraction. Examples of anisotropic materials are calcite, ice and quartz. When the material is doubly refracting, it is called birefringence. This optical property is interesting because it is polarization-dependent.

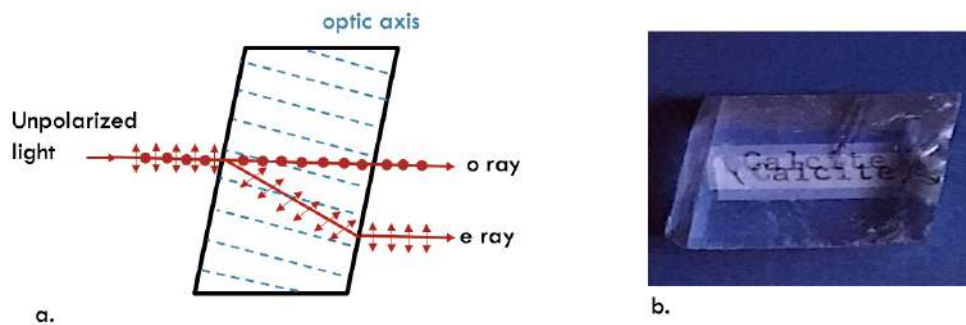


Figure 3.1: Birefringent crystal. a) Schematics of an unpolarized beam that is doubly refracted by birefringent crystal. The input beam splits into an ordinary beam (o-ray) and an extraordinary beam (e-ray). The ordinary beam will be linearly polarized and travels just like in an isotropic medium. The extraordinary beam will be polarized in the orthogonal direction and will be laterally displaced b) Photo of calcite crystal showing the effect of double refraction [2]

When unpolarized light passes through a birefringent crystal as shown in Figure 3.1 at some non-zero angle to the optical axis of the crystal, the beam will be doubly refracted and split into two components. The two beams are linearly polarized in orthogonal directions. The ordinary beam (o-ray) is the beam that passes through a birefringent crystal in a straight line and it has a refractive index n_o . In contrast, the beam that is refracted is called an extraordinary beam (e-ray) and has a refractive index n_e . The optic axis has a particular direction, and it is indicated by dashed lines in Figure 3.1a. Along that axis, $n_o = n_e$ means there is no extraordinary ray transmitted[2].

3.2 Design of A Position to Polarization Converter

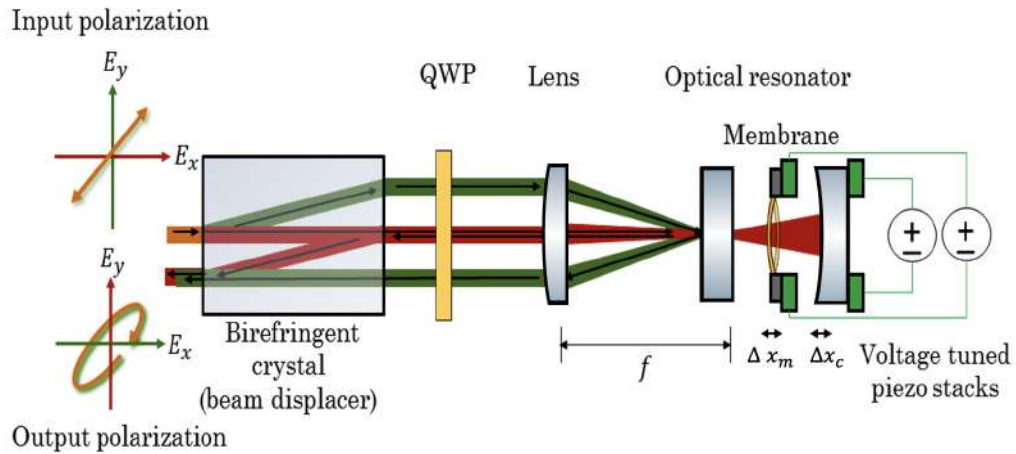


Figure 3.2: Design of the position-to-polarization converter. A stable polarization interferometer is formed between a beam displacer and an asymmetric, plano-convex optical cavity containing a transparent membrane. The input beam is split into the signal (red) and reference (green) beams of orthogonal polarization. The signal beam is mode-matched to a TEM_{00} mode of the cavity. Upon reflection from the entrance mirror, located in the focal plane of a lens, both beams are recombined by the displacer, thus closing the interferometer. A double-pass through a quarter-wave plate (QWP) provides the necessary exchange of horizontal and vertical polarization components for beam recombination. As a result, membrane motion causes phase shifts of the signal beam and thus variation of the output polarization. Resonator length and membrane position can be actively controlled.

The principle of a position-to-polarization converter design is shown in Figure 3.2. It is based on a polarizing beam displacer/combiner, which spatially splits a polarised input laser beam into two orthogonally polarized components. Both ordinary and extraordinary beams are focused by a single lens onto an asymmetric optical cavity. The extraordinary beam is not aligned along the optical axis of the cavity and is reflected off the first mirror under an angle and serves as an optical phase reference. The ordinary beam travels along the optical axis and is brought into resonance with a cavity mode by precisely tuning the position of the back mirror with a piezo element. The light that enters the cavity reflects back and forth multiple times and will interact with a transparent, micromechanical membrane that sits in the opti-

cal cavity. Each time it traverses a micromechanical membrane will cause a significant phase shift that depends on the membrane's position. The cavity mirrors have different reflectivity such that the ordinary signal beam leaves the cavity predominantly through the front mirror. The light leaving the cavity can be recombined with the imaged reference beam and form a single beam with modulated polarisation. Position changes and oscillations of the membrane are translated into modulation of the resulting polarization, which can be observed by polarimetry or used to couple to another polarisation-sensitive system such as dispersively coupled atomic ensembles. Back action onto the membrane motion arises from changes or fluctuations of the input polarization as well as overall power, which translates into varying signal beam intensity and radiation pressure inside the cavity.

3.3 Beam Alignment and Mode Overlap

To achieve optimum optomechanical coupling between membrane and beam polarization, the input laser beam has to be mode matched to a TEM_{00} mode of the optical cavity while at the same time ensuring mode-overlap between signal and reference beam paths. The control of beam size and divergence is needed for mode-matching to the cavity mode but these should not be adjusted using the lens depicted in Figure. 3.2, which ensures signal and reference beams are overlapped. The distance between the lens and the reflecting surface of the front mirror of the cavity must be equal to the focal length f because the beam displacer produces a parallel signal and reference beams. These should again be parallel when returning to the displacer. For a collimated beam of the correct diameter and a planar-concave cavity as used here, this condition may coincide with matching the beam divergence to the cavity mode (for vanishing Gaussian focal shift [62]). Any further mode-matching to the cavity mode should be performed by shaping the laser beam before entering the beam

displacer.

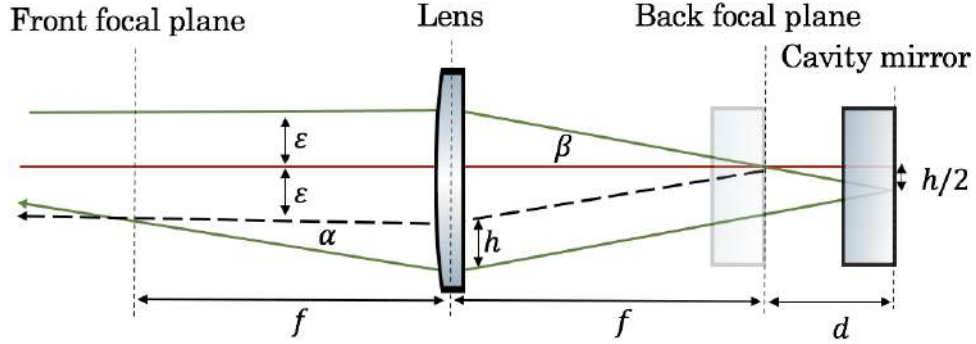


Figure 3.3: *Geometry of reference beam alignment. If the lens-cavity distance deviates from one focal length, the returning signal (red, along the optical axis) and reference beams (green) will not be parallel, leading to reduced mode overlap after recombination by the beam displacer (not shown). The dashed line shows the intended reference beam path. The depicted degree of typical misalignment is exaggerated here for clarity.*

The geometric precision that is required for sufficient beam overlap can be estimated, i.e. the tolerance to deviations of the correct lens-mirror distance. In the case of the distance between the lens and the reflecting surface of the front mirror of the cavity not equal to the focal length f , the reference beam will gain a small angle α as illustrated in Figure 3.3. For a distance error d between the reflecting surface and back focal plane of the lens, the focusing angle β is determined by beam separation ε and focal length f . Thus, the two triangles that have β as one angle give

$$\tan\beta = \frac{h}{d} = \frac{\varepsilon}{f} \quad (3.1)$$

where ε is the distance between the signal and reference beams of the birefringent crystal. From this, we find that the reflected reference beam will be parallel displaced from its intended path by a distance

$$h = \frac{\varepsilon d}{f} \quad (3.2)$$

The returning reference beam will deviate by an angle α and cross the intended beam path in the front focal plane. We use the small angle approximation, $\tan \alpha \approx \alpha$. If α is too large, it will result in the beams no longer overlapping and being able to recombine after passing back through the birefringent crystal. Consequently, the angular deviation from the geometry can be calculated as follows

$$\alpha = \frac{2h}{f} \quad (3.3)$$

substituting Equation 3.2 into 3.3 leads to

$$\alpha = \frac{2\varepsilon d}{f^2} \quad (3.4)$$

When signal and reference beam are recombined, a reduced mode overlap manifests as a spatial modulation of resulting beam polarisation in the near field and may lead to beam separation in the far field. The beam displacer introduces identical displacements ε during the splitting and recombination processes. Therefore, we can evaluate the transversal mode matching by the overlap between the actual and intended reference beam. For various distances between the lens and cavity mirror, the two returning beams intersect as shown in Figure 3.4 in the front focal plane of the imaging lens resulting interference pattern. Thus, α can be defined in term of fringe spacing Δz and laser wavelength λ as

$$\tan \alpha \approx \alpha = \frac{\lambda}{\Delta z} \quad (3.5)$$

comparing α in Equation 3.4 and 3.5 leads to

$$\Delta z = \frac{f^2 \lambda}{2\varepsilon d} \quad (3.6)$$

where Δz is the distance between light (or dark) fringes. The returning beams differ only in their transverse momentum which is given by the wave number

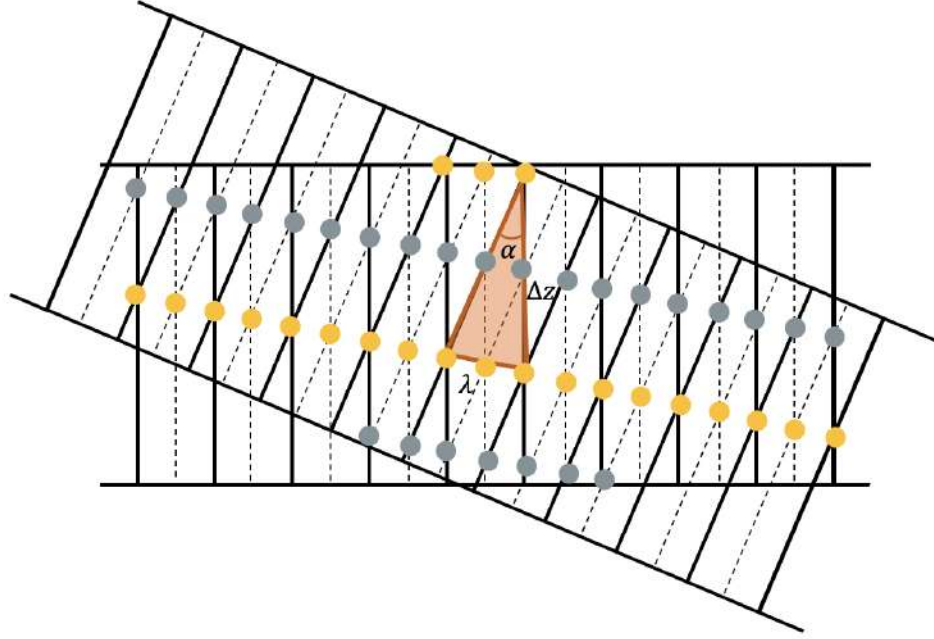


Figure 3.4: The reference beam has an angle α with respect to the signal beam, where the crest is indicated by the solid line and the dashed line marks the trough. The constructive interference is yellow highlighted and it occurs when the crest of one of the beams intersects with a crest of another beam or a trough meets another trough. The destructive interference is grey-highlighted and it appears where a crest meets a trough.

difference

$$\Delta k = \frac{2\pi}{\lambda} \sin\alpha \approx 2\pi \frac{2\varepsilon}{\lambda f^2} d \quad (3.7)$$

The interference fringes will vanish if the lens is placed a focal length away from the cavity mirror resulting in the optimum overlap between the signal and reference beams.

The overlap between the reference and signal beams can be estimated using Gaussian beam profiles (we mean the amplitude profile, which has phase, not the intensity). For the signal beam, we assume a two-dimensional Gaussian beam profile with the main axes aligned along x and y . Without considering its phase it is given by

$$E_{sig}(x, y) = E_0 e^{-\frac{(x-x_0)^2}{2\omega_x^2}} e^{-\frac{(y-y_0)^2}{2\omega_y^2}}, \quad (3.8)$$

here the coefficient E_0 is the amplitude, x_0 and y_0 are the position of the centre of the distribution (mean), whereas ω_x , and ω_y are the width of the Gaussian (standard deviation). The Gaussian beam profile for the deviating reference beam is given by

$$E_{ref}(x, y) = E_0 e^{-\frac{(x-x_0)^2}{2\omega_x^2}} e^{-\frac{(y-y_0)^2}{2\omega_y^2}} e^{-i(xk_x+yk_y)} e^{-ia(x^2+y^2)} \quad (3.9)$$

where $e^{-i(xk_x+yk_y)}$ refers to the relative beam tilting (it will have a relative phase that depends linearly on lateral distance) whereas $e^{-ia(x^2+y^2)}$ represents a different curvature of the beam (assuming circular symmetry). The normalized overlap of the two amplitude profiles is given by

$$\text{Overlap} = \int_{-\infty}^{\infty} \int_{-\infty}^{\infty} \frac{E_{ref}(x, y)E_{sig}(x, y)dxdy}{\sqrt{|E_{sig}(x, y)|^2 \cdot |E_{ref}(x, y)|^2}dxdy} \quad (3.10)$$

To simplify this, the mismatch in overlap can be calculated by assuming that the signal and reference beams are near-collimated Gaussian beams of sufficient diameter. It means that the radii of curvature of the beams approach infinity (and thus $a = 0$) and any changes in wavelength due to the Gouy phase shifts can be ignored. The overlap integral between the ideal and tilted reference beam becomes

$$\text{Overlap} = \int_{-\infty}^{\infty} \int_{-\infty}^{\infty} \frac{2}{\pi w^2} e^{-\frac{x^2+y^2}{w^2}} e^{-i\Delta kx} dxdy = e^{-\frac{\Delta k^2 w^2}{8}}, \quad (3.11)$$

where w is the beam waist which is constant along the collimated beam path.

The effect of displacing the lens away from the focal plane by distance d has to be investigated experimentally to check how the sensitivity of precision of the alignment of two beams overlaps. The output of the converter is sent to a camera instead of the balanced photo-detector and the MIM optical cavity is replaced with a plane mirror. In this configuration, the only contribution to a phase difference between the reference and signal cavity beams should

be any optical path length difference due to air fluctuations and from any misalignment of the optical system.

If a plane mirror or MIM cavity sits exactly at the front focal plane of the lens, the reflection of the reference and signal cavity beams will be quite overlapped with no interference. Displacing the lens away from the focal plane by distance d will cause interference fringes. The interference fringes occur because the reference beam is slightly inclined by a small angle α with respect to the signal cavity beam and it can be monitored by a camera for different values of d . At the separation of the two dark bands closest to the centre, one can measure the fringe spacing Δz . The six images in Figure 3.5 illustrate how lens displacement d affects the separation distance between two bright (or dark) fringes. Clearly, Δz is getting smaller as d increases.

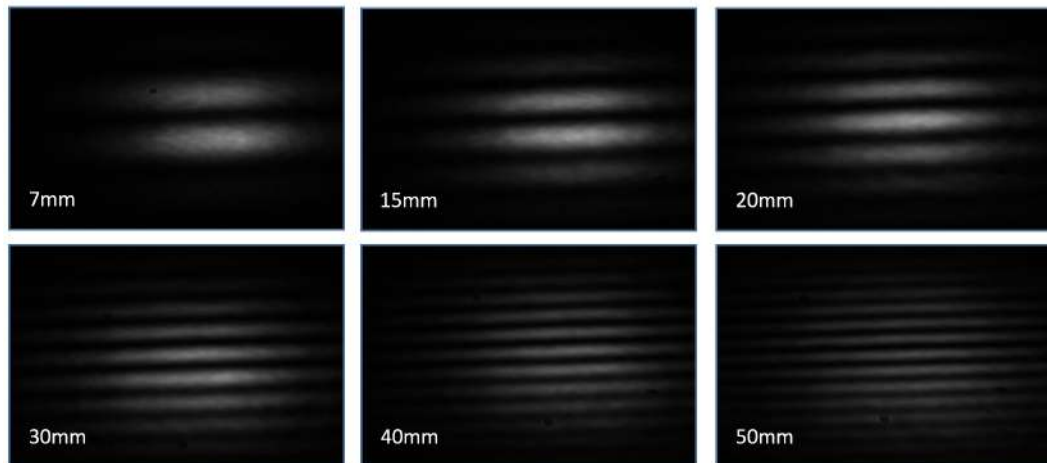


Figure 3.5: The six images illustrate how the spacing between fringes Δz varies with distance in mm. (Images are taken using ThorCam software (DCC1645C) with resolution $(1280 \times 1024 \text{ Pixels})$).

The spatial fringe frequency is proportional to the deviation of lens-cavity distance from one focal length and can be used to locate the correct lens position. It shows the interference becomes visible as we move away from the lens focal plane, see Figure 3.6 (top).

For a beam that is mode-matched to our MIM cavity with $\lambda = 780 \text{ nm}$,

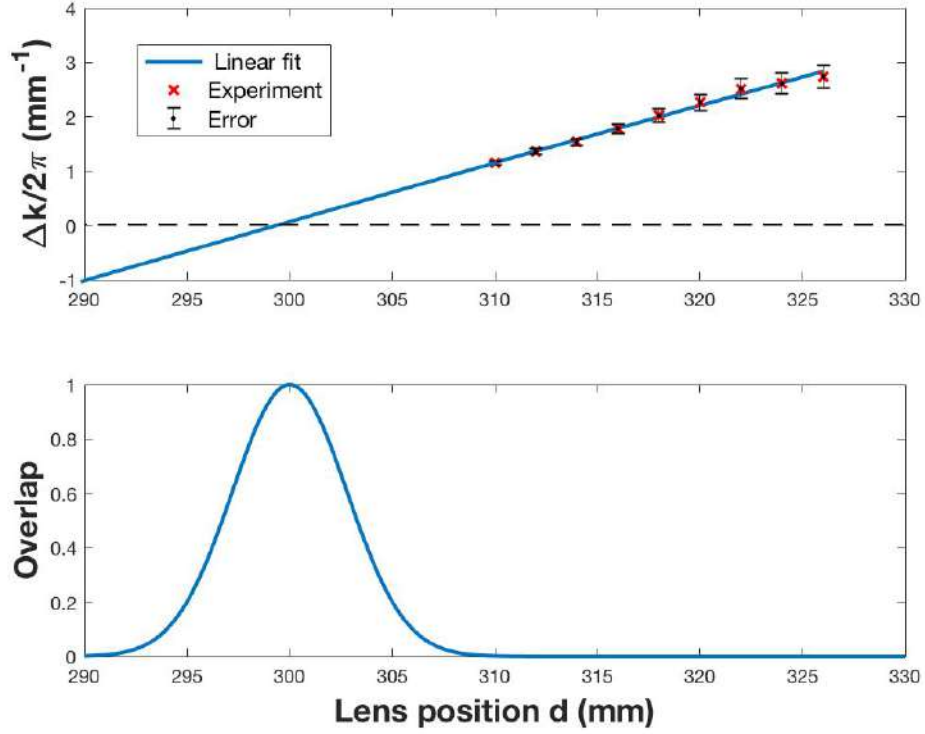


Figure 3.6: *The mismatch in the overlap between signal and reference beam. Alignment precision and mode overlap (bottom). The spatial fringe frequency is proportional to the deviation of lens-cavity distance from one focal length and can be used to locate the correct lens position (top). The expected mode overlap for deviations from that position shows the tolerance to misalignment. The estimated positioning accuracy of $\approx \pm 0.7$ mm allows for a mode overlap of better than 0.985. (bottom)*

a beam waist of $w = 0.7$ mm, a beam displacement of $\varepsilon = 4$ mm, and a focal length of $f = 300$ mm, we find that the lens position must be accurate to $\approx \pm 1.3$ mm to achieve an overlap of better than 95%. The overlap is shown in Figure 3.6 (Bottom) is plotted using Equation 3.11.

The robust polarization interferometer that is shown above can be implemented into the experimental setup which will be discussed in the next chapter.

Chapter 4

Opto-Mechanical Setup

The optomechanical system requires a constructed setup that has to be stable and vacuum-compatible. To enhance the coupling of the MIM system, we need an optical cavity to be short for easy alignment, a thermally stable holder of the optical cavity to avoid any thermal drift and is supported by vibration isolation. This chapter highlights the experimental setup with its main considerations for the optomechanical system. Lastly, the locking scheme, which requires keeping the cavity on resonance with the laser, is described as involving forward feedback.

4.1 Designing A Thermally Stable Cavity Holder

To achieve optimum stability of the optical cavity, the material of the holder of the optical cavity was chosen to be a combination of invar and aluminium as shown in Figure 4.1. Invar is known for its uniquely low thermal expansion coefficient $\alpha_{Invar} = 1.7 \times 10^{-6}/^{\circ}\text{C}$ and aluminium which is used to hold the concave mirror has a high thermal expansion coefficient $\alpha_{Aluminium} = 2.3 \times 10^{-5}/^{\circ}\text{C}$. In addition, the mirror is made of fused silica which has a low thermal expansion coefficient $\alpha_{Fusedsilica} = 0.55 \times 10^{-6}/^{\circ}\text{C}$ and the piezoelectric chip is a

standard piezo ceramic component with thermal expansion coefficient $\alpha_{PZT} = 20 \times 10^{-6}/^{\circ}\text{C}$.

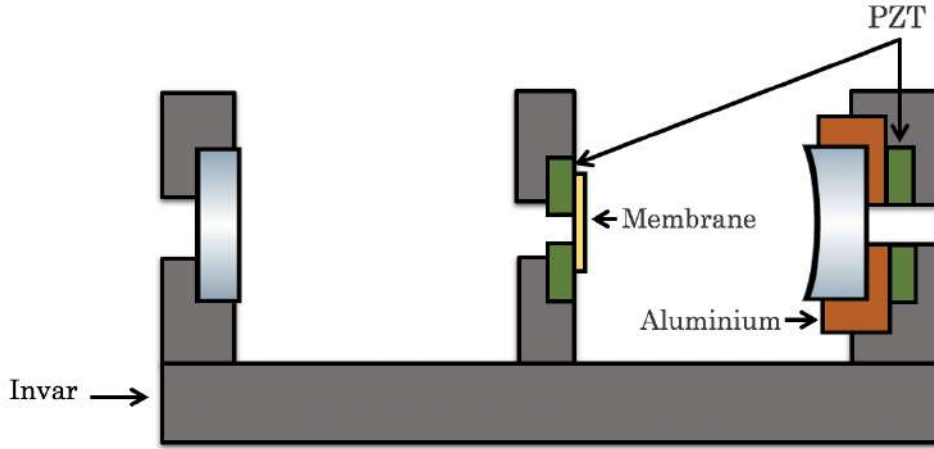


Figure 4.1: Holder design for a stable cavity.

Thermal expansion of the holder will expand or change the size of the material as the temperature varies. The essential advantage of using these two materials is that the Invar will expand outward whereas the mirror and aluminium expand inward causing the change in the length to be exactly zero. Thus, the length of the optical cavity is fixed. The initial length of the holder in Figure 4.2 between the two mirrors L_{cavity} is given by

$$L_{cavity} = L_1 - 2L_2 - L_3 - L_4 - L_5 - L_6 \quad (4.1)$$

where L_1, L_3 and L_6 are lengths of invar. The thickness of the mirror and PZT are labelled by L_2 and L_4 respectively. L_5 refers to the length of the aluminium holder see Figure. 4.2. The length after thermal expansion can be calculated as a function of the initial length L_i ($i = 1, 2, 3, 4, 5, 6$), temperature difference ΔT and linear thermal expansion coefficient $\alpha_{materiel}$. The length after the thermal expansion of each material is given as

$$L_{Invar} = (L_1 - L_3 - L_6)(1 + \alpha_{Invar}\Delta T) \quad (4.2)$$

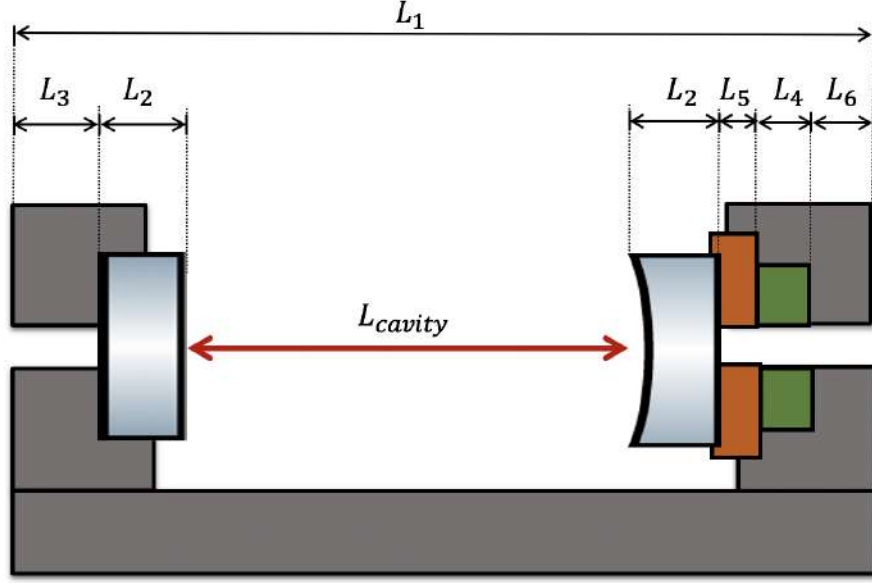


Figure 4.2: Illustration of the lengths of each material where ($\alpha_{Aluminum} > \alpha_{Invar}$).

$$L_{Fusedsilica} = L_2(1 + \alpha_{Fusedsilica}\Delta T) \quad (4.3)$$

$$L_{Aluminum} = L_5(1 + \alpha_{Aluminum}\Delta T) \quad (4.4)$$

$$L_{PZT} = L_4(1 + \alpha_{PZT}\Delta T) \quad (4.5)$$

The length of the cavity after the thermal expansion of the holder will vary slightly and it can be written as

$$\delta L_{cavity} = L_{Invar} - 2L_{FusedSilica} - L_{Aluminum} - L_{PZT} \quad (4.6)$$

Thus, the difference in length before and after thermal expansion of the holder D has to be zero to have a thermally stable cavity as

$$D = L_{cavity} - \delta L_{cavity} = 0 \quad (4.7)$$

By considering slightly variation in the temperature $\Delta T = 1^\circ C$, the length of the Invar $L_1 = 52\text{mm}$, $L_3 = 3.99\text{mm}$ and $L_6 = 2\text{mm}$. The thickness of the mirror and PZT are $L_2 = 6.35\text{mm}$ and $L_4 = 3\text{mm}$ respectively. Thus, the

length of aluminium can be obtained by

$$L_5 = \frac{(L_1 - L_3 - L_6)\alpha_{Invar} - 2L_2\alpha_{FusedSilica} - L_4\alpha_{PZT}}{\alpha_{Aluminum}} \quad (4.8)$$

To satisfy the condition in Equation 4.7, L_5 is calculated to be 0.5 mm.

4.2 Membrane Holder Design

The membrane is lying freely on the small invar holder that sits in a recessed location (groove) 5.5×5.5 mm in size and it is clamped into the holder securely by a thin clamping plate (sheet). The holder has three screws on the top, the middle screw is to fix the membrane holder into the optical cavity mount and the screws near the edges are used to align the membrane with respect to the cavity optical axis, see Figure 4.3. The PZT sits between a small holder and the big holder and it is screwed with a spring.



Figure 4.3: *The membrane holder.*

This holder is designed such that the membrane can be tilted in two directions such that it can be adjusted to be parallel to the front mirror and thus orthogonal to the optical axis. The membrane holder finally is integrated into the cavity mount as shown in Figure 4.4c. It is screwed on top of the cavity

holder which enables us to exchange the membrane without the need to disassemble the setup further. Details of the holder can be found in Appendix B.

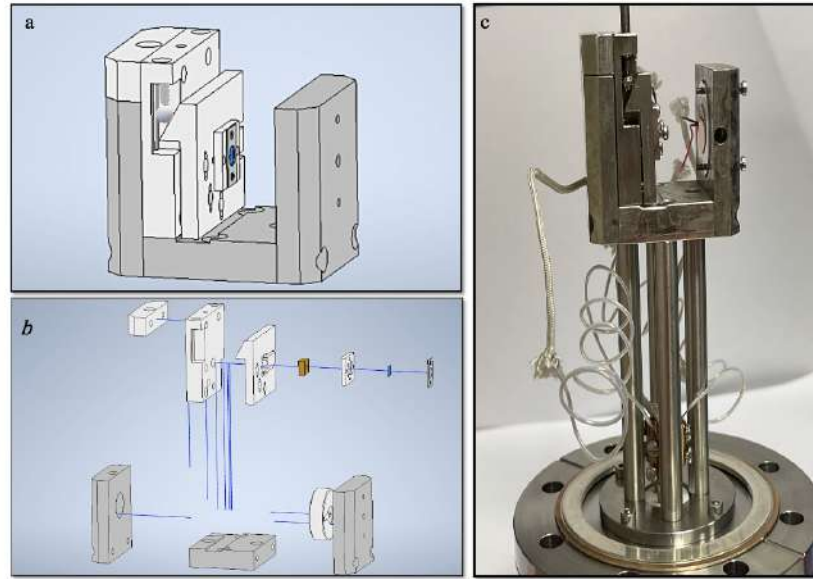


Figure 4.4: (a) Membrane holder fixed into optical cavity mount. (b) Assembly of all parts of the optomechanical holder which are attached to a flange that is provided with electrical feedthrough to power PZTs in (c).

4.3 Vacuum System

The optomechanical system is enclosed in a high vacuum at low pressure which is required to prevent damping of the mechanical quality factor of the membrane and fluctuation of air which affects the cavity stability. Our chamber is a 4-way standard cross, the optical access of the cavity is on the horizontal ways and has two parallel AR-coated viewports (Lewvac, 795nm). The vertical ways have a flange that has the holder with feedthrough and the gate valve on the opposite side. There is access to the membrane alignment with opened gate valve. The pumping system is connected to the gate valve and it involves a turbo (D-35614 Asslar) and roughing (MVP 040-2) pump. The roughing pump first turns on for 30min-1hr, then we turn the turbo pump on for 1-2hr and finally we close the valve with turn both pumps off for taking our measurements. Unfortunately, there is no space to have a pressure gauge to measure

the pressure but we estimate it to be low as clearly shown in our measurement, which is approximated 10^{-6} . Exchanging the membrane is effortless and can easily be done by unscrewing the attached window to the gate valve.

4.4 Experimental Setup

The experiment has two optical breadboard tables: the MIM vacuum chamber is placed on the optical breadboard table that has passive isolation mounts with an anti-vibration mat under each foot. The MIM system is inside a box that is enclosed by foam acoustic insulation see Figure 4.5. The laser beam is well coupled to an optical fibre from the second optical breadboard table that has the DLpro laser and the filter cavity.

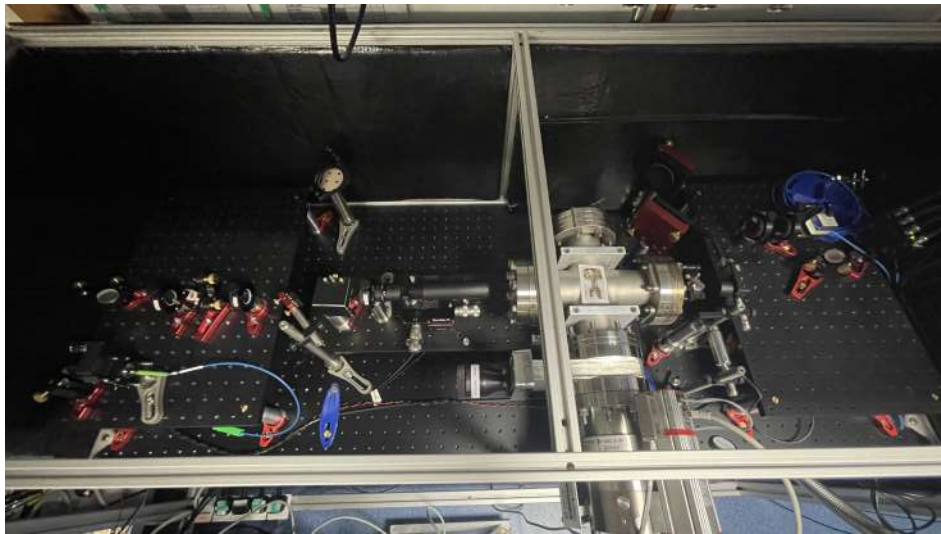


Figure 4.5: A photograph of MIM optical breadboard, showing the MIM vacuum chamber and optical elements.

The optical setup for the laser source is shown in Figure 4.6 shows DLpro laser beam splits by a polarizing beam splitter (PBS) and the intensity of the beam is adjusted by a half-wave plate (HWP). The transmitted beam of PBS is sent to the Rb spectroscopy to ensure that the laser is on the desired wavelength. The reflected beam of PBS is sent to the filter cavity with lens (f_1) to match the laser mode to the mode of the filter cavity. This cavity with a

linewidth of ≈ 160 kHz was introduced to reduce frequency fluctuations of the laser. That is well coupled and the reflected signal shows a strong dip in the intensity corresponding to TEM_{00} mode. The divergence of the transmitted beam will be adjusted to match the optical fibre mode by the lens (f_2). The reflected signal from the cavity is detected by a fast photo-detector (PD1) which is used to lock the filter cavity to the laser via PDH. The transmission of the filter cavity is coupled into an optical fibre to MIM setup.

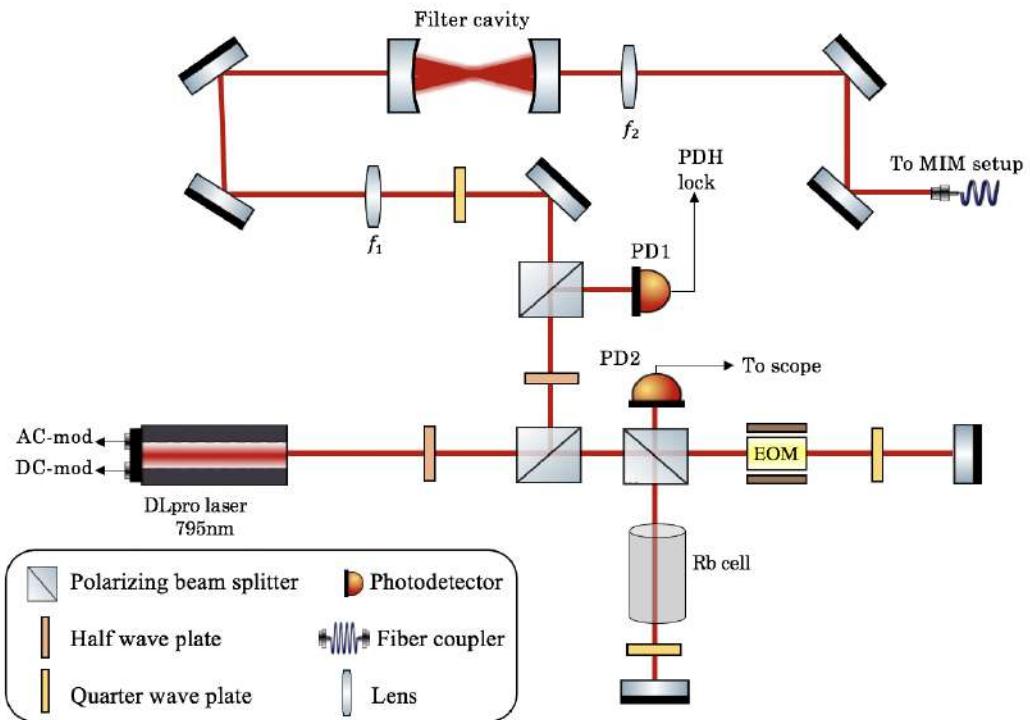


Figure 4.6: Setup for filter cavity experiment. Laser light is sent through a filter cavity to eliminate the laser frequency fluctuations.

The MIM cavity setup is shown in Figure 4.7. The output fibre coupler passes through HWP and PBS to adjust the laser power as needed which is a few microwatts. Then, the laser beam is split by the displacer and focused by a lens (f_3) to the MIM cavity. The displaced beams have to recombine as one beam after reflection from the MIM cavity and the polarization of that beam must be balanced by pair of HWP and QWP with PBS. The balanced signal or dispersive signal is detected by a balanced photodetector (BPD) which takes the difference between the two inputs. Even though the cavity length

is reasonably stable due to the thermally stable holder design, the dispersive signal is used to actively lock the MIM cavity. It also can be used to read out the thermal noise of the membrane as we will discuss in the next chapter.

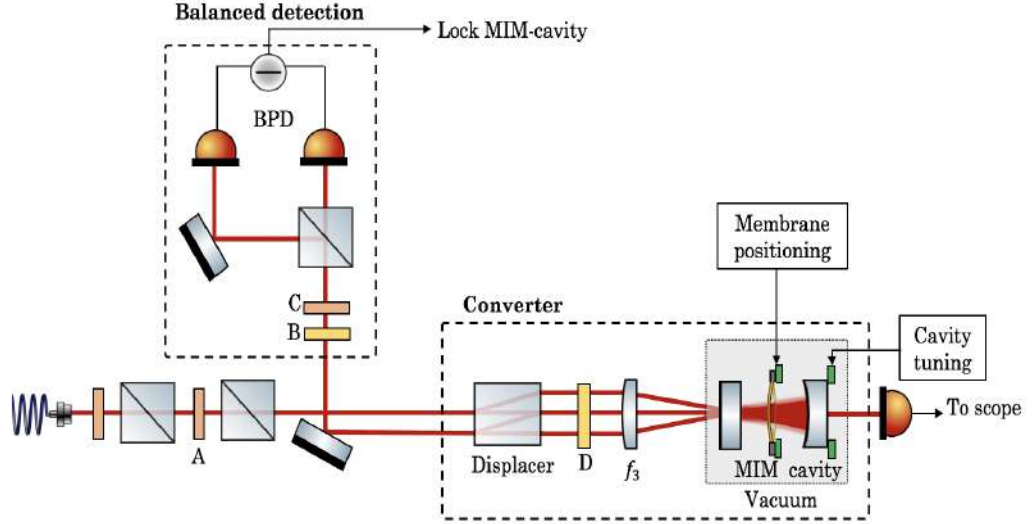


Figure 4.7: Experimental MIM setup including position to polarization converter detection. A-D are waveplates which are adjusted sequentially in order to optimise the polarization.

4.4.1 Mode Matching and Cavity Considerations

The laser beam mode has to be matched to the fundamental mode of the cavity TEM_{00} . The MIM cavity is constructed by a plano-concave mirror which leads to beam divergence. Thus, the input laser beam requires beam waist ω_0 at location z_R for optimized coupling and they are defined as

$$\omega_0 = \sqrt{\frac{\lambda z_R}{\pi}} \quad (4.9)$$

$$z_R = \sqrt{\frac{L_{cavity}(R_1 - L_{cavity})(R_2 - L_{cavity})(R_1 + R_2 - L_{cavity})}{(R_1 + R_2 - 2L_{cavity})^2}} \quad (4.10)$$

where $R_{1,2}$ is the radius of curvature and L_{cavity} is the length of the cavity.

The filter cavity is a symmetric cavity with reflectivity $r_{1,2} = 99.95\%$ and radius of curvature $R_{1,2} = 1000\text{mm}$. The length of the filter cavity is 180mm

and the cavity mode waist is $275.5\mu\text{m}$ at the centre cavity. In the case of symmetric cavity where $R_1 = R_2$, leads to $z_R = \sqrt{2RL_{\text{cavity}} - L_{\text{cavity}}^2}$.

The mode of the filter cavity has to be matched to the laser mode. The output of the DLpro laser has a spot size of 1.7mm and the needed lens for mode matching has a focal length of 750mm at a 550mm distance from the cavity centre. The power through the filter cavity is 4-5mW when the laser is locked. The power intensity of TEM₀₀ has a slight dependence on the laser frequency. The transmission of the filter cavity is coupled into an optical fibre by $f_2 = 500\text{mm}$ lens, which gives more than $200\mu\text{W}$ out of the fibre. We measured up to $270\mu\text{W}$.

The MIM cavity is an asymmetric cavity consisting of a flat mirror $R_1 = \infty$ and a Plano-Concave mirror with a radius of curvature $R_2 = 100\text{mm}$. The length of the MIM cavity is $L_{\text{cavity}} = 30\text{mm}$ and the cavity mode waist is $\omega_0 = 213.2\mu\text{m}$ at the flat mirror. In the case of asymmetric cavity where $R_1 \neq R_2$, leads to $z_R = \sqrt{R_2L_{\text{cavity}} - L_{\text{cavity}}^2}$. The output of the fibre coupler is collimated with a spot size of 1.5mm and from Equation 2.64 the needed lens for perfect mode matching is $f_3 = 300\text{mm}$. The mode matching begins with aligning the MIM cavity without the membrane to TEM₀₀ mode. Then, the membrane is carefully inserted without distorting the spatial mode.

4.4.2 Polarimetric measurement and phase adjustment

The converter performance works as a linear-birefringent and linear dichroic reflector. Dichroism arises from losses in the cavity, which also depends on the position of the membrane. The signal and reference beams that are produced and recombined by the beam displacer are referred to as (unbalanced) linearly polarized beams which have vertical (V) and horizontal (H) polarization. One of these beams will enter the MIM cavity and variable signal $\Delta\phi$ is carried

by their relative phase. Due to lens imperfection alignment or any spurious birefringence, one can consider a phase offset ϕ_0 . In our MIM setup, homodyne detection is shown in Figure 4.7. The resulting dispersive signal from the detection which is shown in Figure 4.8 is an output of BPD which represents the difference between the two inputs. It can be balanced and compensate for any phase offset by a pair of QWP and HWP. The output polarization can be visualized as a vector on the Poincaré-sphere as depicted in Figure 4.10. Both wave plates cause a rotation of the Poincaré-sphere such that any imbalance in the intensity between the resulting H and V components is maintained to be $\Delta\phi = 0$.

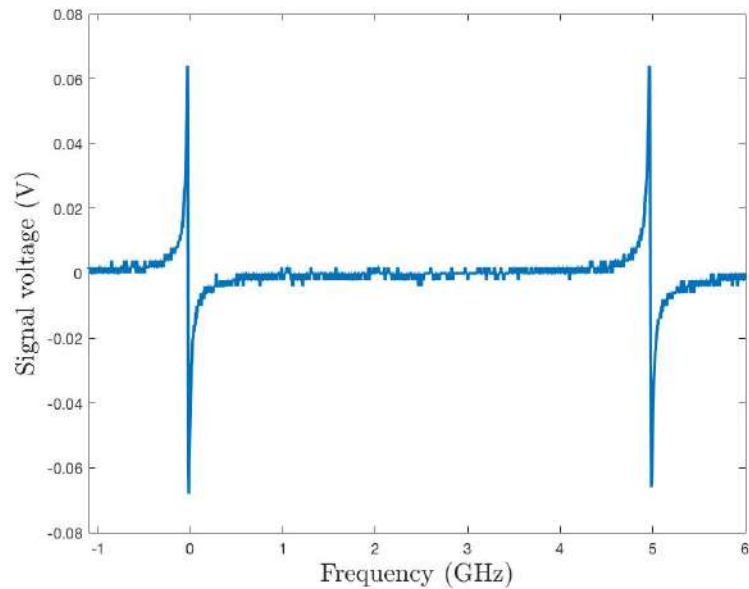


Figure 4.8: *The balanced signal as a function of detuning between cavity and laser beam.*

The polarization of the input laser beam until the balanced detection stage has to be adjusted by waveplates labelled A, B, C and D in Figure 4.7. It is essential to illustrate how to balance the dispersive signal in BPD which can be done in three steps:

1. Adjusting plate A to have the desired ratio of intensities for the signal and reference beams that are produced by the displacer and we balance them in the absence of plates B and C. We should note that rotating

- plate D may have two outputs and we have to ensure that the output is the recombination of the signal beam from the MIM cavity and the reference beam. The effect of rotating plate D is illustrated in Figure 4.9
2. Blocking one of the two beams of the displacer, simply an iris can block the reference beam, and then insert plate B and balance the signal on BPD. This ensures that the orthogonal linear polarisations of the signal and reference beam are converted into orthogonal circular polarisations. See part (b) of Figure 4.10.
 3. Finally, we should have both beams, add plate C in front of BPD, and balance it to compensate for any phase offset between the two beams, see part (c) of Figure 4.10.

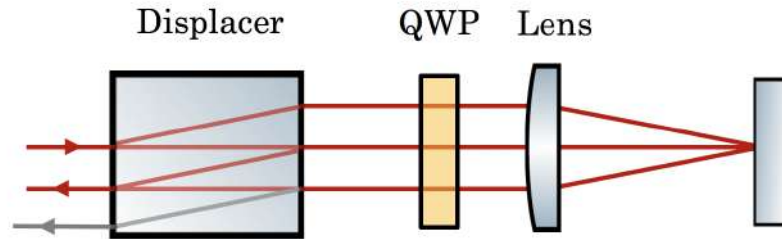


Figure 4.9: Rotating QWP will change the polarization of the recombined beam resulting in two beams. The grey beam is undesirable and QWP has to be rotated to eliminate it.

The action of the correctly adjusted waveplates is such that on the Poincaré sphere, the measurement of the detection is represented by Stokes vector component \hat{S}_z returning from the converter while the converter leads to rotations about the \hat{S}_x -axis if the cavity produces a phase shift (and changes in \hat{S}_x -component and overall power due to light absorption in the cavity). The quantum mechanical Stokes operators follow the definitions for photon flux differences and a right-handed coordinate system as discussed in Section 2.5.

Adjustment of polarimetric measurement basis on the Poincaré sphere is illustrated in Figure 4.10 which shows that the imbalanced signal and reference

beam returning from the cavity are combined in a horizontal/vertical(H/V) basis with some phase offset ϕ_0 and varying phase difference $\Delta\phi$. The combined polarisation is depicted in (a). A quarter-wave plate introduces a 90-degree rotation about the anti-/diagonal (A/D) axis, shown in (b), transforming signal and reference to orthogonal circular polarisations (L/R). Finally, a half-wave plate allows for the compensation of the phase offset by introducing opposite phase shifts to the circular components (and swapping L/R). The phase difference $\Delta\phi$ is mapped onto the imbalance between H and V polarisations.

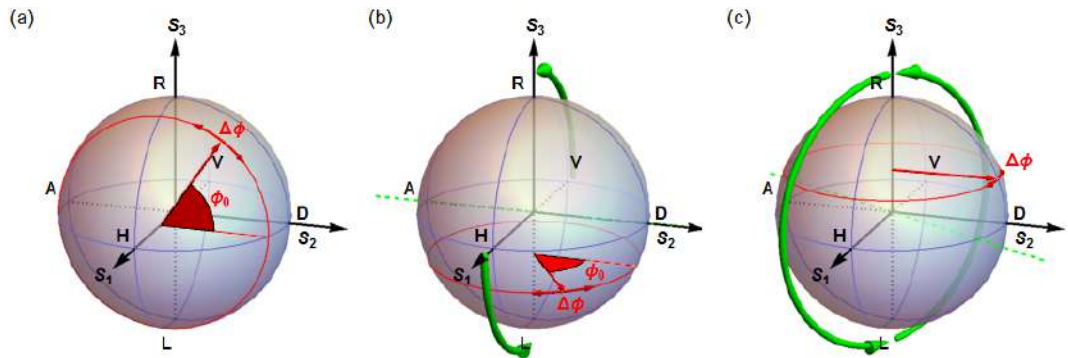


Figure 4.10: Adjustment of polarimetric measurement basis. The imbalanced signal and reference beam returning from the cavity are combined in a horizontal/vertical (H/V) basis with some phase offset ϕ_0 and varying phase difference $\Delta\phi$. The combined polarisation is depicted on the Poincaré sphere in (a). A quarter-wave plate introduces a 90-degree rotation about the anti-/diagonal (A/D) axis, shown in (b), transforming signal and reference to orthogonal circular polarisations (L/R). Finally, a half-wave plate allows for the compensation of the phase offset by introducing opposite phase shifts to the circular components (and swapping L/R). The phase difference $\Delta\phi$ is mapped onto the imbalance between H and V polarisations

4.5 Theory of Pound Drever Hall Locking System

Locking the fluctuating laser frequency to the narrow band filter cavity requires fast feedback, which we achieve using the PDH technique. By extracting an error signal proportional to the frequency difference between the filter cavity and the laser beam. The error signal will be feedback via some control actuator, e.g. a piezoelectric actuator, laser current or an electro-optic modulator. Enhancing the system with a closed feedback loop leads to the laser frequency will be locked to the cavity resonance when the proportional-integral-derivative (PID) controller modifies the beam frequency. Conversely, the cavity of resonance will be locked to the laser frequency when PID modifies the length of the cavity[63]. Let us introduce the mathematical description of the PDH

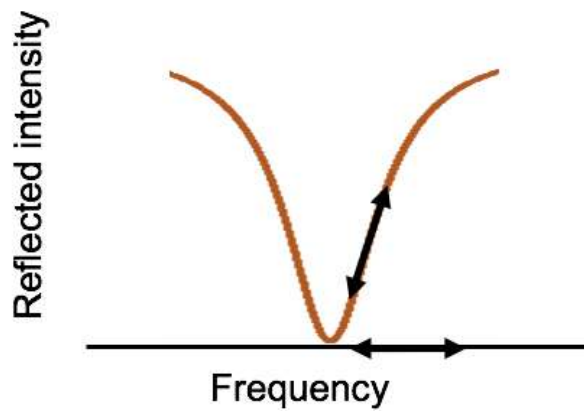


Figure 4.11: *The reflected signal from the cavity as a function of frequency. If the frequency is modulated with a small shift, one can tell from the slope which side of resonance the frequency is on.*

technique. The magnitude of the electric field of incident E_i and reflected E_r beam at one point outside of the filter cavity can be described as

$$E_i = E_0 e^{i\omega t} \quad (4.11)$$

$$E_r = E_1 e^{i\omega t} \quad (4.12)$$

Where E_0 and E_1 are complex relative phases between the two waves, ω is the angular frequency of the laser. For a lossless symmetric cavity, the reflection coefficient r_c defines as the ratio of E_i and E_r as

$$r_c = \frac{E_r}{E_i} = \frac{r [e^{i\frac{\omega}{FSR}} - 1]}{1 - r^2 e^{i\frac{\omega}{FSR}}} \quad (4.13)$$

Where r is the mirror reflectivity and $FSR = c/2L_{cavity}$ is the free spectral range of the cavity with a length of L_{cavity} .

The phase of the reflected beam can be measured by modulating the laser frequency (or phase). It will tell us if the laser frequency is above or below the cavity resonance. The electric field of the incident beam after passing through a phase modulator is given by

$$E_i = E_0 e^{i(\omega t + \beta \sin \Omega t)} \quad (4.14)$$

The modulation creates sideband frequencies which are different from the frequency of the incident and reflected beams. For small modulation depth ($\beta < 1$), the equation 4.14 can be expanded using Bessel function as follows[64]

$$E_i = E_0 [J_0(\beta) e^{i(\omega t)} + J_1(\beta) e^{i(\Omega + \omega)t} - J_1(\beta) e^{i(\omega - \Omega)t}] \quad (4.15)$$

Where Ω is the frequency of the phase modulation β is modulation depth, and J_0 and J_1 are the first kinds of Bessel function. Three components of the incident beam on the cavity appear with different frequencies: a carrier with ω frequency and sideband frequencies with $\omega \pm \Omega$ [65]. Thus the total electric

field of the reflected beam is given by

$$E_r = E_0 [r_c(\omega)J_0(\beta)e^{i(\omega t)} + r_c(\omega + \Omega)J_1(\beta)e^{i(\omega+\Omega)t} - r_c(\omega - \Omega)J_1(\beta)e^{i(\omega-\Omega)t}] \quad (4.16)$$

The modulation depth determines the relative power in the carrier P_c and in the sidebands P_s . If the total power of the reflected beam is $P_0 = |E_0|^2$, then $P_c = J_0^2(\beta)P_0$, and the sidebands' power in each first order is $P_s = J_1^2(\beta)P_0$. Most of the power will be in the carrier and the first order sidebands in the case of small modulation depth; $P_0 \approx P_c + 2P_s$.

The resultant beam is a wave with an envelope that shows the beat pattern between the two frequencies of sidebands as

$$\begin{aligned} P_r = |E_r|^2 = & P_c|r_c(\omega)|^2 + P_s \{|r_c(\omega + \Omega)|^2 + |r_c(\omega - \Omega)|^2\} \\ & + 2\sqrt{P_c P_s} \{ \text{Re} [r_c(\omega)r_c^*(\omega + \Omega) - r_c^*(\omega)r_c(\omega - \Omega)] \cos \Omega t \\ & + \text{Im} [r_c(\omega)r_c^*(\omega + \Omega) - r_c^*(\omega)r_c(\omega - \Omega)] \sin \Omega t \} + (2\Omega \text{ terms}) \end{aligned} \quad (4.17)$$

The Ω term appears as a result of the interference between the sidebands and the carrier and the 2Ω term originates from the interference of the sidebands with each other. In the experiment, the laser is modulated at a high frequency where the modulation is larger than cavity linewidth ($\Omega \gg \text{FWHM}$). Thus, the sidebands must be perfectly reflected preventing any cavity power to transfer into the sidebands as we see in Figure 4.12. The error signal is given by

$$[r_c(\omega)r_c^*(\omega + \Omega) - r_c^*(\omega)r_c(\omega - \Omega)] \approx -i2 \text{Im} \{r_c(\omega)\} \quad (4.18)$$

which is purely imaginary. The cosine term is ignored in Equation 4.17 and it is experimentally blocked by PD signal with a mixer and low pass filter. Thus, what ends up is the error signal (ϵ) which is nearly linear, asymmetric near

resonance and proportional to $\sin\Omega t$ as shown in Figure 4.12, it is given by

$$\epsilon = -2\sqrt{P_c P_s} \text{Im} \{r_c(\omega)r_c^*(\omega + \Omega) - r_c^*(\omega)r_c(\omega - \Omega)\} \quad (4.19)$$

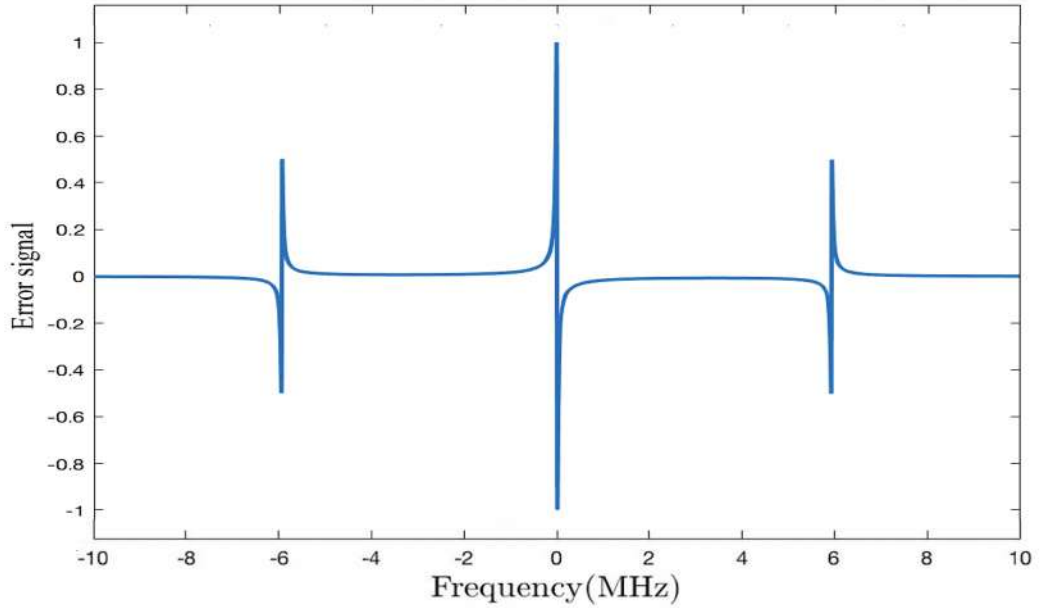


Figure 4.12: The PDH error signal and the sidebands at frequency modulation at $\Omega = 6\text{MHz}$.

In Figure 4.12, the error signal is zero when the laser is resonant with the cavity but it has a maximal slope and it scales by $\sqrt{P_c P_s}$ in Equation 4.19. The following section will show our locking scheme for the filter and MIM cavity.

In our filter cavity locking, the power of the sidebands is adjusted to obtain a suitable error signal while the most power is still contained in the carrier. When the cavity is locked, only the carrier is transmitted through the filter cavity and brought to the MIM cavity setup via the optical fibre while the sidebands are reflected, because they are far away from the filter cavity resonance. They are 6MHz away, while the linewidth of the filter is only 160kHz.

4.5.1 Locking Scheme

The stability of the laser and the optomechanical system is essential to pave the way for measuring the thermal noise of the membrane. There are two schemes for locking in our experiment: Active locking stabilisation of the MIM cavity using the dispersive signal and locking of the filter cavity by the PDH technique.



Figure 4.13: Locking setup to lock the MIM cavity via balanced signal.

The locking scheme for the optomechanical system is uncomplicated as shown in Figure 4.13. The converter's output polarization that results from BPD can be utilized directly for active stabilization of the MIM optical cavity. It is characterized as sufficiently stable due to the geometric robustness and nearly identical path lengths in the interferometer. The dispersive signal is our error signal and it is sent to the PI controller that is connected to the PZT controller to provide the required feedback to keep the MIM cavity in resonance with the laser.

The schematic of PDH to lock the filter cavity is shown in Figure 4.14. A dual-channel function generator is used where Ch1 modulates the AC-modulation input of the DLpro laser to produce sidebands onto the laser via current modulation and Ch2 provides an RF modulation signal at 6 MHz. The RF signal which is the reflected signal from the filter cavity is measured with a highly sensitive photodiode. It is mixed with a local oscillator (LO) which is in phase with laser modulation. The output of the mixer is phase shifted and it is split: One part passes through a low pass filter (LPF) to isolate low frequencies which serve as an input for the PI controller which is fed back to

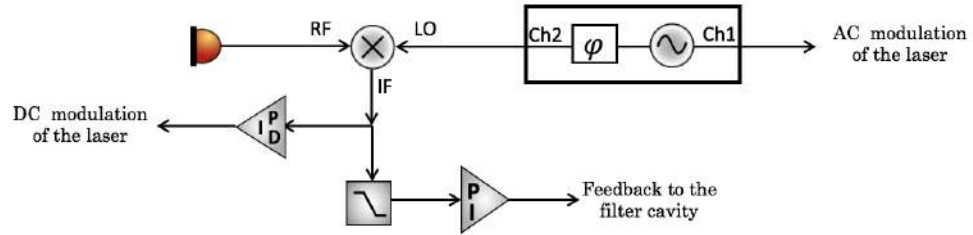


Figure 4.14: Active stabilization locking setup to lock the filter cavity using PDH technique.

the laser to keep it locked on resonance with the filter cavity. The second part is sent to the PID controller to provide fast feedback to the laser. The schematic of the PID card is provided in Appendix.C. Applying fast feedback to the laser current and slow feedback to the filter cavity piezo allows us to narrow the linewidth of the laser such that it enters the cavity and we are still able to lock the laser to an atomic transition for the next stage. All electronic components of the locking system are listed in Table. 4.1

Function generator	Siglent, SDG2122X
Photodiode	Thorlabs, PDA10A2
Mixer	MiniCircuits,
Low pass filter	Stanford Research System, RS570
Balanced photodiode	Thorlabs, PDB210A

Table 4.1: Electronics of locking system.

The error signal is shown in Figure 4.15 with generated sidebands at 6MHz. The feedback system is set up to resist changes in the laser frequency around the resonance. Therefore when the feedback is connected to the DC modulation laser, the error signal is flattened as the locking signal is attempting to correct the change in frequency caused by the PZT scanning.

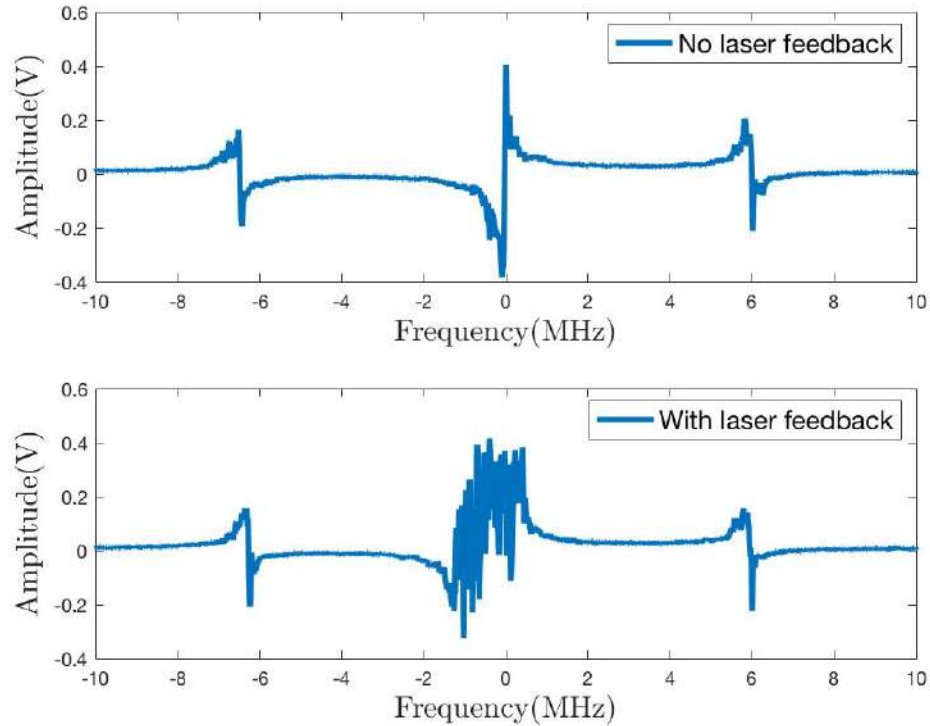


Figure 4.15: *The error signal with generated sidebands. Top: when there is no feedback to the DC modulation laser and the laser is scanned sufficiently fast over the cavity resonance. Bottom: When there is feedback to the DC modulation laser, the laser frequency is kept longer in the vicinity of the resonance and fast frequency fluctuations become visible in the error signal.*

4.6 Theory of Feedback

If we have a linear-time invariant system in a closed loop, the output will control the input that is applied to the system. The control of the output is achieved by comparing the output to the required input via the feedback path. As shown in Figure.4.16, the system can be mathematically described by a transfer function which relates the input to the output [66].

The input in our system is typically the dispersive signal and the error represents the detuning between laser frequency and cavity resonance which will add noise to the input signal. Thus, the output signal is defined as

$$\text{Output} = F(\omega) \times \text{error} \quad (4.20)$$

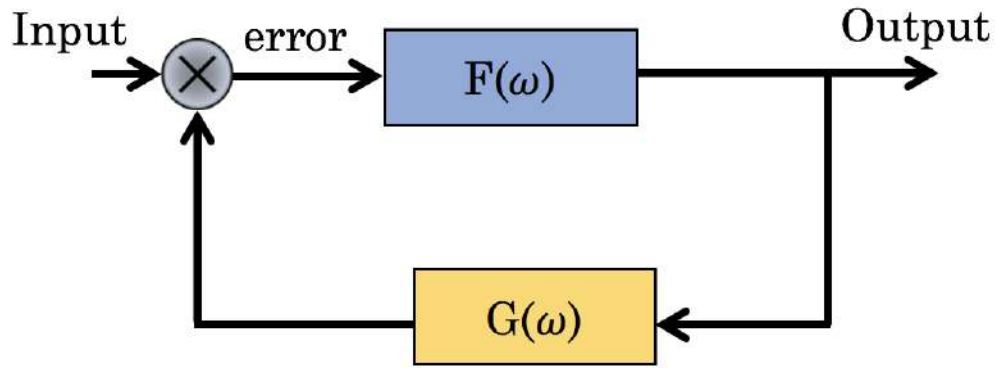


Figure 4.16: Feedback block system.

where $F(\omega)$ represents the open-loop gain of the system, and $G(\omega)$ represents the gain of the system in the feedback path. Both are functions of frequency. The detuning is given by (error = Input - $G(\omega)$ x Output) and it can be substituted in Equation.4.20 to construct the transfer function which is the ratio of the output to its input and it is defined as

$$S = \frac{\text{Output}}{\text{Input}} = \frac{F(\omega)}{1 + F(\omega)G(\omega)} \quad (4.21)$$

The overall gain of negative feedback closed-loop control system in Equation 4.21 may increase or decrease depending on the value of $(1 + F(\omega)G(\omega))$ and $F(\omega)G(\omega)$. If the value of $(1 + F(\omega)G(\omega)) > 1$, the overall gain will increase whereas the overall gain will decrease when $(1 + F(\omega)G(\omega)) < 1$. The value of $(F(\omega)G(\omega))$ may be negative or positive leading to a negative or positive gain of the feedback path respectively. In the presence of time delays of the feedback, one can define $F(\omega) = e^{i\omega(t+\tau)}$ where τ is the time delay. In the case of $\tau = 0$, there is no phase delay however $\tau \neq 0$ leads to phase delay and ω will increase that phase. Any closed loop system can be fully described by looking at three parameters: The gain (amplitude), phase and frequency. Also, the frequency response can be visualized by the Bode plot, Nyquist plot and Nichols plot [35]. All three plots display the amplitude and phase shift for every single frequency. The system has to be stable with no damping

oscillation by checking every frequency in the Bode plot that has a magnitude of 0dB and ensuring that the phase is not -180° [67]. These plots will be experimentally shown in the following section.

4.6.1 Feedback For Noise Suppression

As shown in Figure 4.17, the MIM cavity is locked to the laser via the dispersive signal which feeds as an error signal to the PI controller. The output of the PI is sent to the analogue interface of the DLpro laser to keep the laser locked to the cavity. The second copy of the dispersive signal passes through an

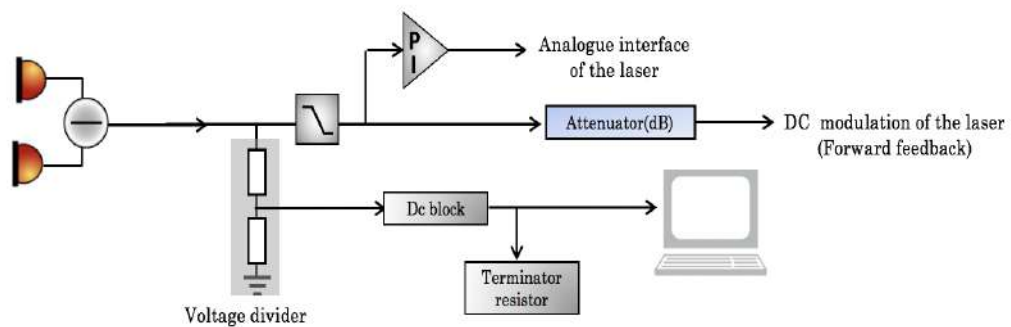


Figure 4.17: *Noise feedback using different attenuators.*

attenuator to the DC-modulation input of the DLpro laser. While locking, we notice a large noise on the error signal. Thus, we used different attenuators to eliminate that noise and compare the noise level. The noise level is measured by the voltage divider output and read out by taking the power spectral density of the dispersive signal.

The noise level of the signal can be seen with different attenuators in Figure 4.18. At ∞ dB, there is no feedback connected which shows the lowest noise on the green curve. In the blue curve at 0 dB, feedback is directly connected with no attenuator. The suppressed noise is seen better at 20 dB by one order of magnitude.

To ensure the feedback system is stable, we need to check the frequency

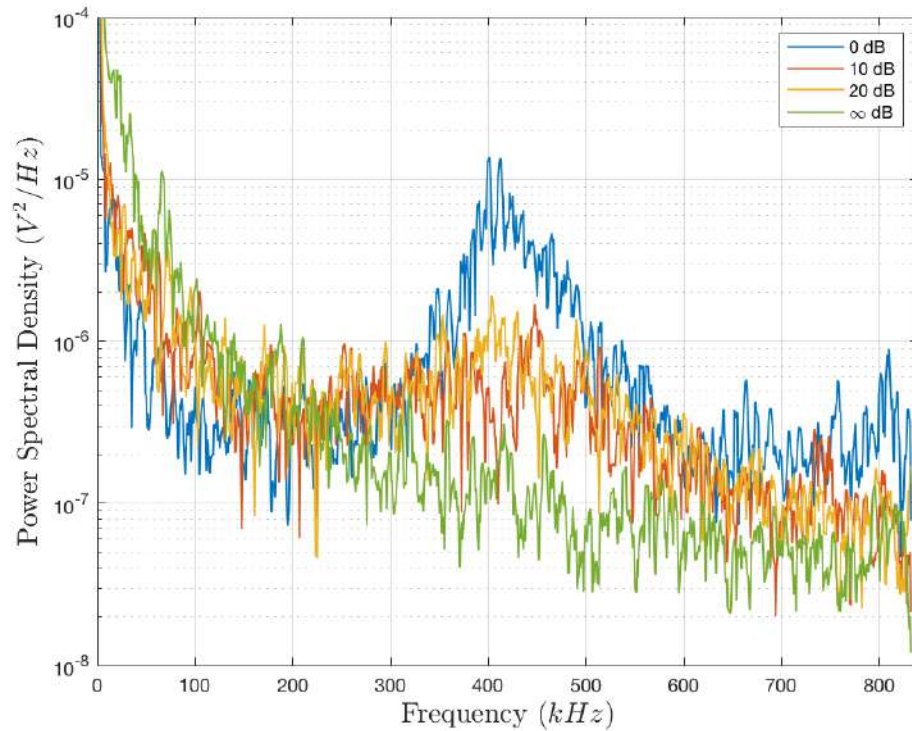


Figure 4.18: Feedback noise level with different attenuators. At ∞ dB, there is no feedback connected and at 0dB is direct feedback with no attenuator.

response of the system in terms of its amplitude (A) and its phase (ϕ) via a vector spectrum analyzer. By sweeping the frequency (f) from 20kHz to 2.1MHz with power bandwidth -40dBm , we read out the phase and amplitude at different single frequency values. Thus, the frequency response of the feedback loop can be visualized by the Bode plot as seen in Figure 4.19. Every frequency on the Bode plot should have an amplitude of 0dB and the phase is not -180° to be specified as a stable system. Figure 4.19 shows that the gain is high with phase 0° at a low frequency while the amplitude drops with -180° phase at a high frequency which tends toward the origin in Nyquist plot, see Figure.4.20.

To check the stability of a system with feedback, Nyquist plot is shown in Figure 4.20 where the real part of the transfer function is plotted on the x-axis and the imaginary part on the y-axis. Stability is determined by achieving loop gain that is smaller than 1 before we reach -180° . In another word,

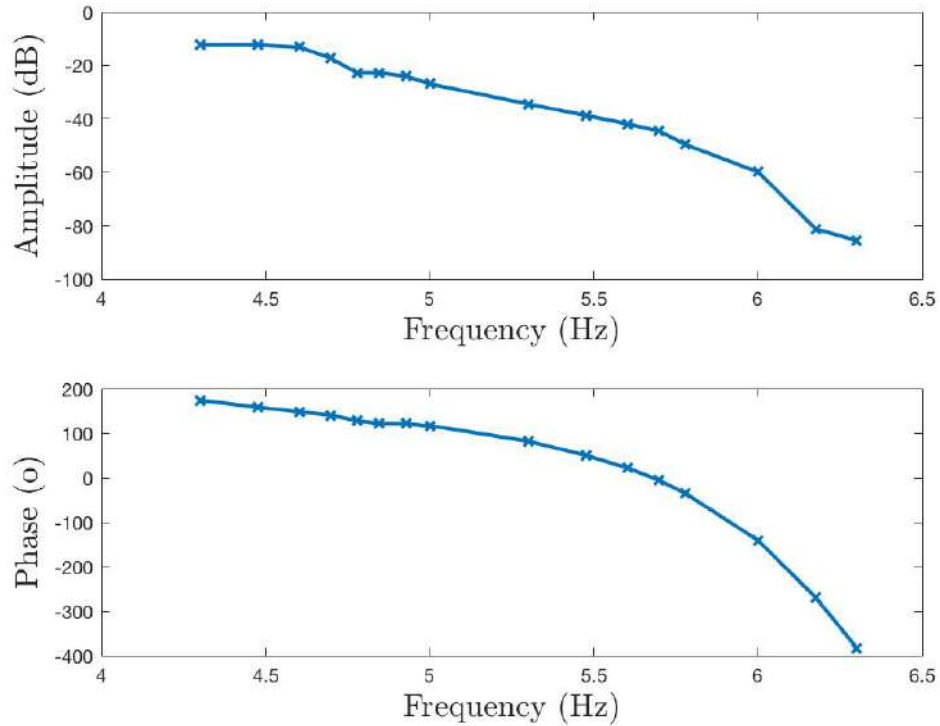


Figure 4.19: Bode plot for frequency response of the feedback system. Top: The amplitude $20\log(A)$ versus the frequency $\log(f)$. The high gain corresponds to low frequency whereas the low gain corresponds to high frequency. Bottom: The phase changes sharply at a higher frequency and it is zero around 5.5 Hz but increases to 180 degrees for lower frequency

the feedback system will be stable as long as the curve on the Nyquist plot does not cross over the critical point $(-1, 0)$ otherwise the system will undergo an oscillation. In addition, locking the filter cavity to the DLpro laser with forward feedback has a time delay. To find how much delay we have, we send the dispersive signal to the vector spectrum analyzer as input and its output is sent to DC-modulation input with a 20dB attenuator. From sweeping the frequency, the time delay simply can be calculated by $\tau = \frac{\Delta\phi}{\Delta f} \frac{1}{2\pi}$. It is found to be $\approx 0.73\mu s$.

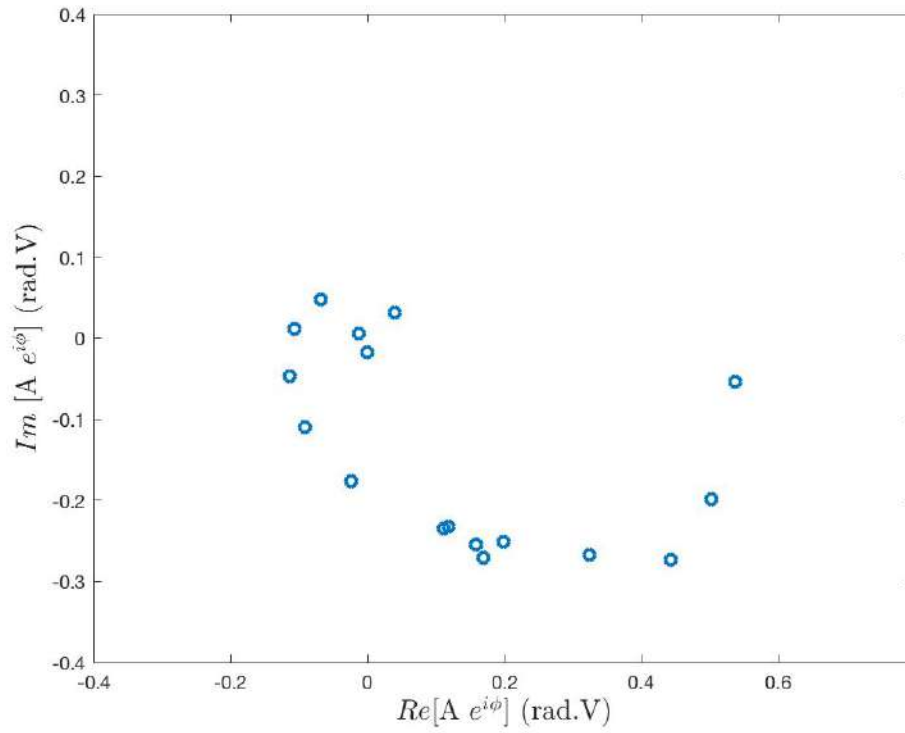


Figure 4.20: Nyquist plot shows the system stability within the amplitude range which should not exceed the critical point.

This chapter has described our special design of the MIM holder that has to be thermally stable. It shows the experimental aspect of the optomechanical setup with its locking scheme. Also, the feedback for noise suppression is discussed. The next chapter will characterize our optomechanical and present the measurement of quantum noises.

Chapter 5

Measurement

In this chapter, we present the measurement results that characterize our optomechanical system. The imaging of the output of the position-to-polarization converter is investigated experimentally to achieve optimum overlap between the signal and reference beams. Our experiment reads out the thermal noise of the membrane and compares it to the shot noise level to reach the quantum regime to see the quantum effects of the membrane. Finally, we will discuss the improvement of our measurement of thermal noise by eliminating laser noise with a filter cavity.

5.1 Characterization of MIM optical Cavity

The MIM optical cavity is an asymmetric cavity in several senses. It consists of a planar front mirror and a concave back mirror with different reflectivities $r_1 = 99\%$ and $r_2 = 99.95\%$ respectively. In the ideal case when there are no losses considered, a theoretical finesse for the empty optical cavity is $\mathcal{F} = 595$. The total cavity length $L_{cavity} \approx 30$ mm corresponds to free spectral range of ≈ 5 GHz. Experimentally, the finesse can be found by measuring the ratio between FSR and FWHM of the TEM_{00} . As shown in Figure 5.1, the

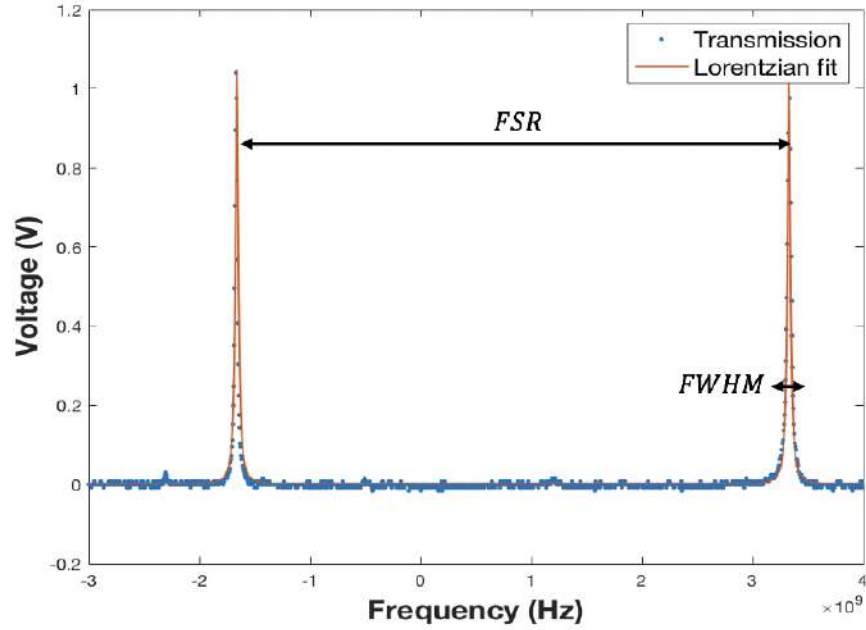


Figure 5.1: Cavity transmission which shows the fundamental mode TEM_{00} .

finesse is found to be $\mathcal{F} = 311.8$ which is reduced due to the optical losses with $FSR = 5$ GHz and $\kappa = 16$ MHz.

The membrane alignment is very sensitive so the mode matching has to be optimized before placing the membrane in the middle of the cavity. Then, the membrane can be attached to the mount of the optical cavity and has to be aligned with respect to TEM_{00} mode. Otherwise, any misalignment or tilting of the membrane will distort the TEM_{00} and it will couple to higher modes. Theoretical intensity distributions for transverse modes of the cavity is corresponding to their imaged MIM cavity which is shown in Figure 5.2.

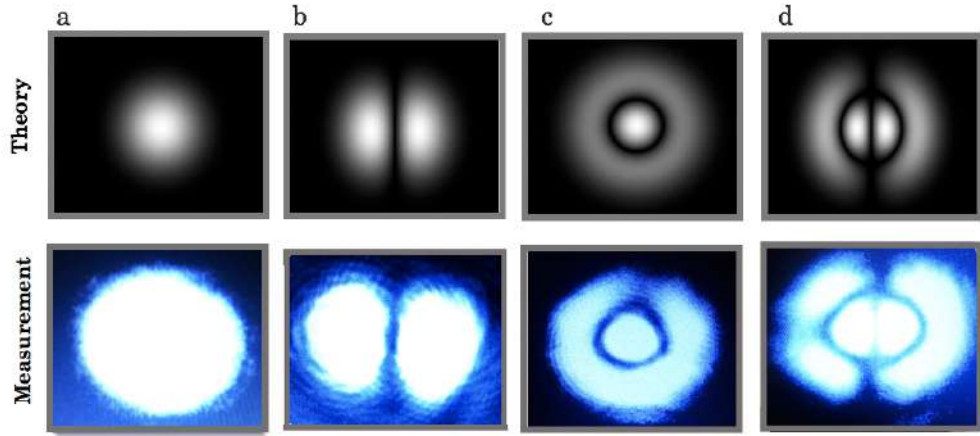


Figure 5.2: Transverse mode of the cavity. Theoretical intensity profiles are shown in the top row and the lower row refers to experimental images for cavity transmission. Column $a \rightarrow (l=0, m=0)$ and $b \rightarrow (l=0, m=1)$ are profile for Hermite-Gaussian mode whereas $c \rightarrow (p=0, m=1)$ and $d \rightarrow (p=1, m=1)$ are profile for Laguerre-Gaussian mode.

We also estimate the signal beam overlap with the TEM_{00} mode of the present cavity by imaging the reflected signal beam for both resonant and off-resonant conditions. Off resonance, both intensity beams are reflected and it is shown in Figure 5.3(a). The reflected intensity on resonance in Figure 5.3(b) will show a drop in the intensity due to the destructive interference between the amplitude of the beam that leaks inside the cavity and the beam that we send in (both beams have opposite phases). Fitting two-dimensional Gaussian beam model functions including beam tilt and relative divergence (see Equation 3.9) to match the two profiles results in a mode overlap of ≈ 0.93 .

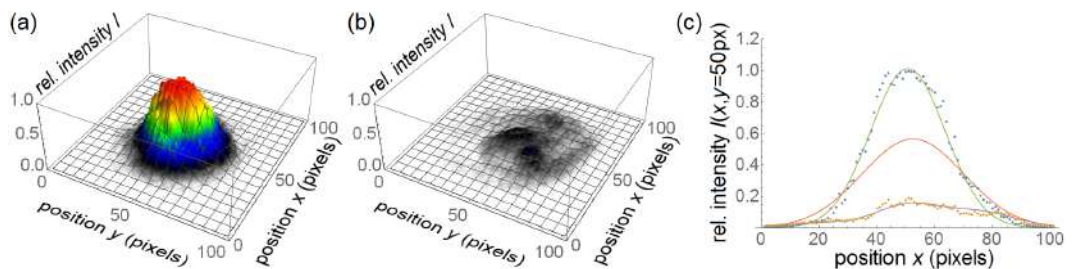


Figure 5.3: Intensity profiles of the reflected beam. The near-Gaussian intensity profile of the signal beam is shown in (a) and the residual reflected intensity for the resonant cavity is shown in (b). Cuts through the data and modelled intensity distributions for those profiles as well as the assumed intensity profile of the cavity are shown in (c).

The details of the membrane will be discussed in the following section.

5.2 Characterization Of the Membrane

The membrane that is used in the experiment is a stoichiometric Si_3N_4 membrane and it has a naturally large tensile stress of $\mathcal{T} \approx 1GPa$ with a size of (1mm x 1mm x 50nm) dimensions [1]. The membrane reflectivity is related to its thickness by

$$|r_m| = \left| \frac{(n_m^2 - 1)\sin kn_m d_m}{2in_m \cos kn_m d_m + (n_m^2 + 1)\sin kn_m d_m} \right| \quad (5.1)$$

where n_m is the refractive index of the membrane which is estimated to be $|n_m| = 2$ in the near-infrared wavelengths with low absorption per pass $\approx 10^{-5} - 10^{-7}$ [7, 68, 69]. The reflectivity of the membrane theoretically can

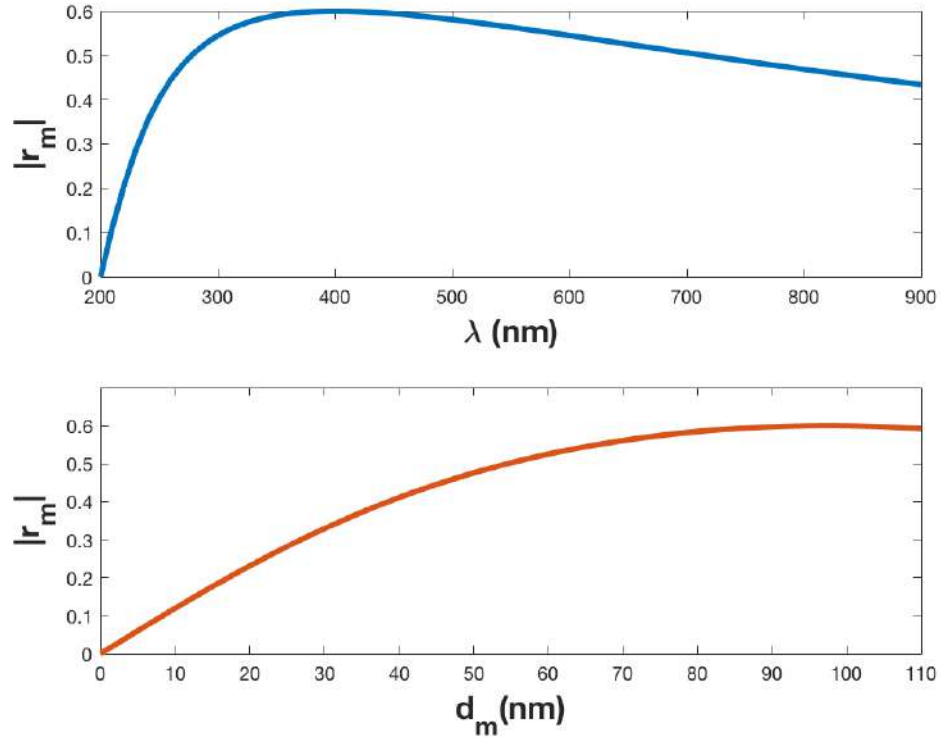


Figure 5.4: The amplitude reflectivity is plotted versus laser wavelengths (top) and versus the membrane thickness (bottom). At $\lambda = 795nm$ and $d_m = 50nm$, the amplitude reflection coefficient is estimated to be 0.47.

be estimated by plotting Equation. 5.1 as a function of the laser wavelengths or membrane thickness which gives $|r_m| = 0.47$ at wavelength 795nm or at thickness 50nm. Experimentally, we send a 1.25 mW laser beam to the membrane to measure the transmitted and reflected power of the membrane as $t_m = 0.866mW$ and $r_m = 0.281mW$ respectively. Thus, membrane reflectivity is found to be $|r_m|^2 = 0.22$ with 0.01 losses which agreed with our estimation.

5.3 Calibration of the Cavity and Membrane PZTs

To measure the gain of the PZT that is used to change the length of the cavity and the position of the membrane by applying DC voltage and reading the amplification on the PZT controller display. The open-loop piezo controller (MDT693B) is used to amplify the voltage that is derived to PZT. The input signal (AC or DC) voltage has to be between 0 V and 10 V. The output signal will follow the input voltage with a gain of 10 V/V depending upon the output voltage limit which is 100 V.

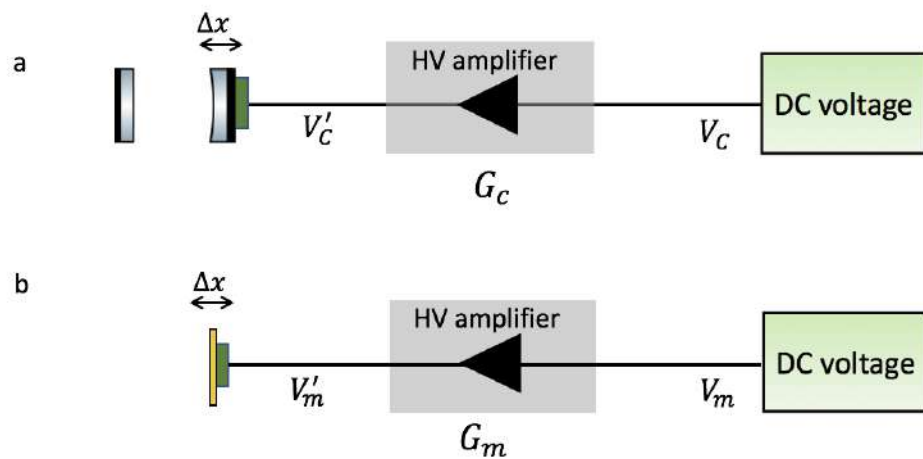


Figure 5.5: Setup for measuring the gain of the PZT a) cavity b) membrane.

To calibrate the cavity and membrane PZTs, the gain has to be measured.

As shown in Figure. 5.5, DC voltage applied to PZT of the cavity V_c to change its length in (a) and the output voltage V'_c can be read on the display of PZT controller. Similar in (b) DC voltage applied to PZT of the membrane V_m to change its position and the output voltage V'_m can be read also in the display of the PZT controller. The output voltage is related to the gain by

$$V'_c = V_c G_c \quad (5.2)$$

$$V'_m = V_m G_m \quad (5.3)$$

where G_c and G_m are the gain of the cavity and membrane PZTs respectively.

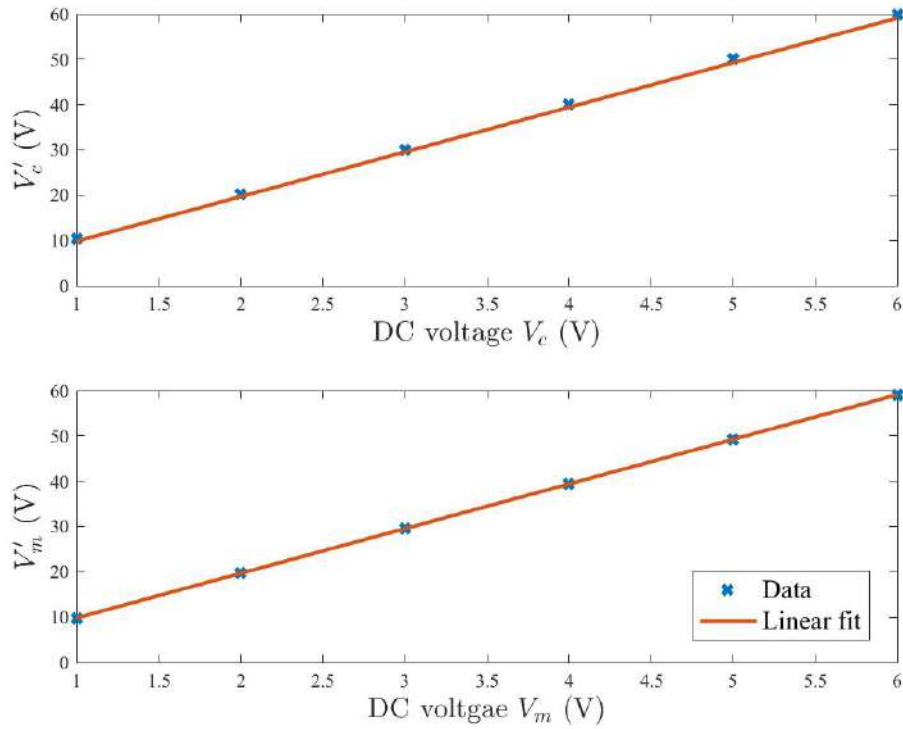


Figure 5.6: The slope of the two plots estimates the gain of the PZT of the cavity G_c (top) and of the membrane G_m (bottom).

The Gain of the cavity and membrane PZTs in Figure 5.6 are $G_c = 9.94$ and $G_m = 9.86$ respectively, which are as expected from the datasheet. The mirror PZT expansion coefficient has a maximum displacement of $\Delta x_c = 2.6 \mu m$

at 150V and experimentally it can be found by

$$\alpha_c = \frac{d(\Delta x_c)}{d(V'_c)} = \frac{\lambda/2}{\Delta V'_c} \quad (5.4)$$

where $\Delta V'_c$ is the distance between two longitudinal modes in volt which is equal to 35V. This leads to α_c to be $8.92 \times 10^{-9} \text{m/V}$. Similarly, the membrane PZT expansion coefficient has a maximum displacement of $\Delta x_m = 3 \mu\text{m}$ and it can be found by

$$\alpha_m = \frac{d(\Delta x_m)}{d(V'_m)} = \frac{\lambda/4}{\Delta V'_m} \quad (5.5)$$

$\Delta V'_m$ is the difference between the maximum and minimum of the location of the resonance in volt as shown in Figure 5.8. It is found to be 29.5V resulting α_m to be equal $6.7 \times 10^{-9} \text{m/V}$.

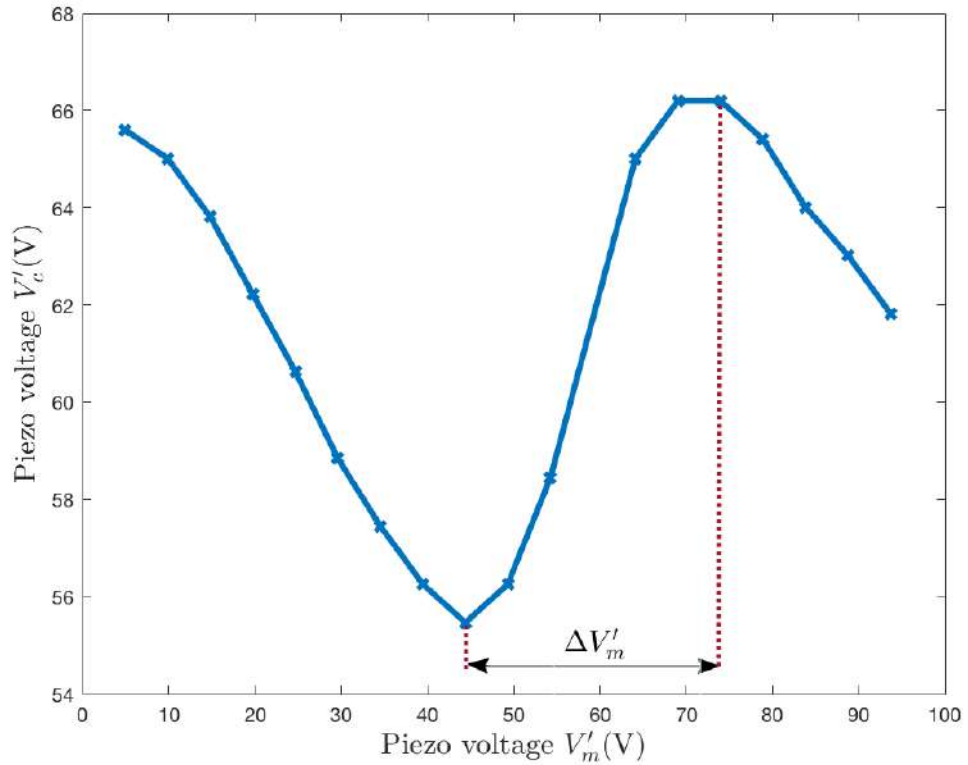


Figure 5.7: This plot shows the difference between the maximum and minimum of the location of the resonance which can be used to estimate α_m .

5.4 Estimating the Position Sensitivity

The dispersive signal will accordingly be shifted as the membrane changes its position. The reading of the location of the dispersive signal or MIM cavity resonance is recorded in small steps and plotted versus the membrane position as shown in Figure 5.8. This membrane effect was calibrated by converting the voltages in Figure 5.7 into frequency versus membrane position. This was done using the cavity mirror voltage that is required to span one free spectral range and the fact that the effect of the mirror position repeats every half wavelength. Then, the maximum slope can be found, which determines the frequency shift per membrane displacement. It is found to be $\beta = 1.2 \times 10^{10}$ Hz/m which is taken from the linear fit. In order to find the sensitivity of the

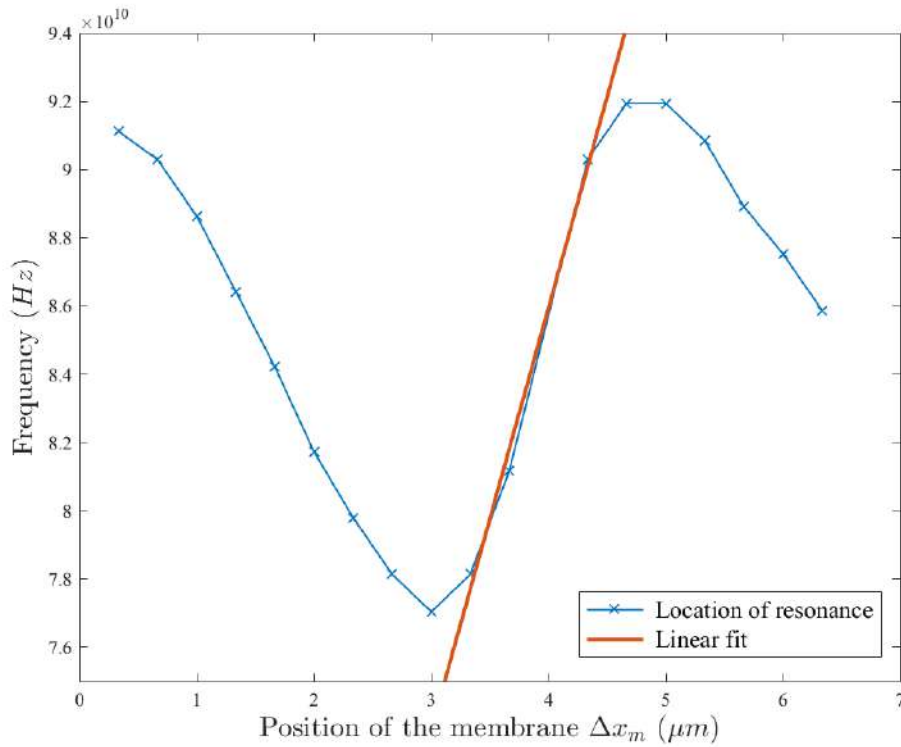


Figure 5.8: The plot shows the position of the dispersive signal versus the membrane position. The slope is fitted between MIM cavity resonance maxima and minima. The x and y axis is calibrated by $\Delta x_m = \alpha_m V'_m$ and $f = V'_c FSR / \Delta V'_c$ respectively.

output signal to position, the maximum slope σ of the dispersive signal has to be found which allows us to estimate the frequency sensitivity which is given

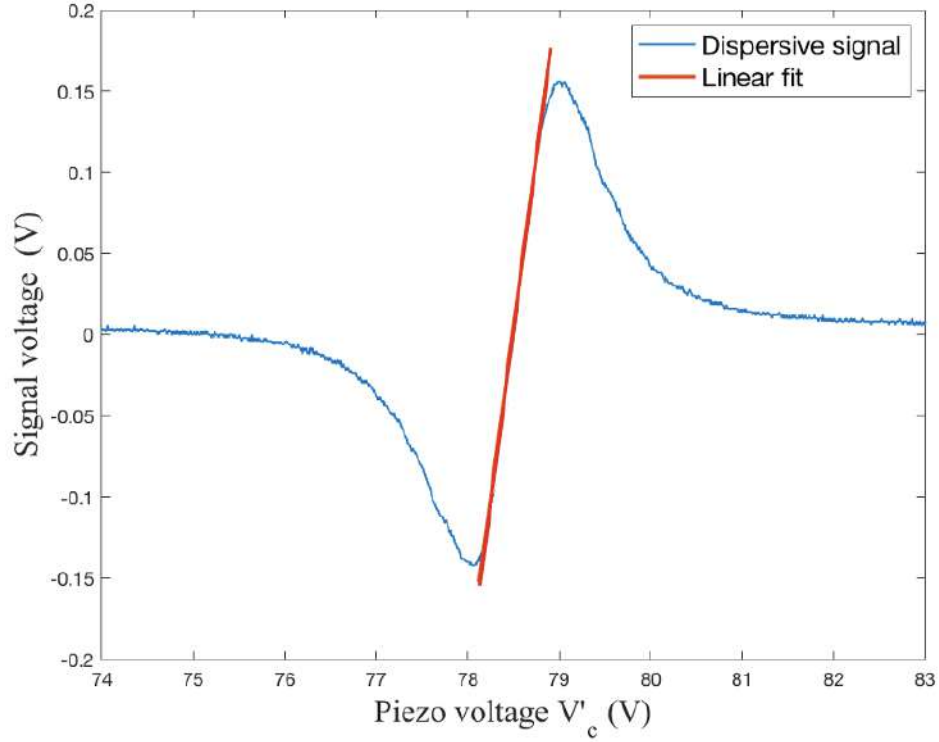


Figure 5.9: *The dispersive signal with the linear fit to estimate σ .*

by $\sigma_f = \sigma \Delta V'_c / FSR$. From the linear fit to the dispersive signal in Figure 5.9, σ is found to be 4.20 V/V. Thus, the maximum position sensitivity can be found by

$$\sigma_x = \sigma_f \beta \quad (5.6)$$

For $\sigma_f = 3.02 \times 10^{-9} \text{V/Hz}$, the maximum position sensitivity is $\sigma_x = 3.7 \times 10^7 \text{V/m}$. Therefore, we expect signal amplitudes on the order of microvolts for membrane displacement as small as picometers. This will be the typical size of thermal membrane motion.

It is important to note that position sensitivity depends on a number of varying parameters such as the changing finesse as well as signal and reference beam powers.

5.5 Finesses of the optomechanical system

The finesse of the MIM cavity depends strongly on the parallel alignment of the membrane and front mirror. The membrane changes its location by applying DC voltage to the PZT of the membrane V_m . Thus, MIM cavity resonance shifted in small steps as shown at the top of Figure 5.10 with its phase at the bottom. The shift of the cavity resonance experimentally shows different

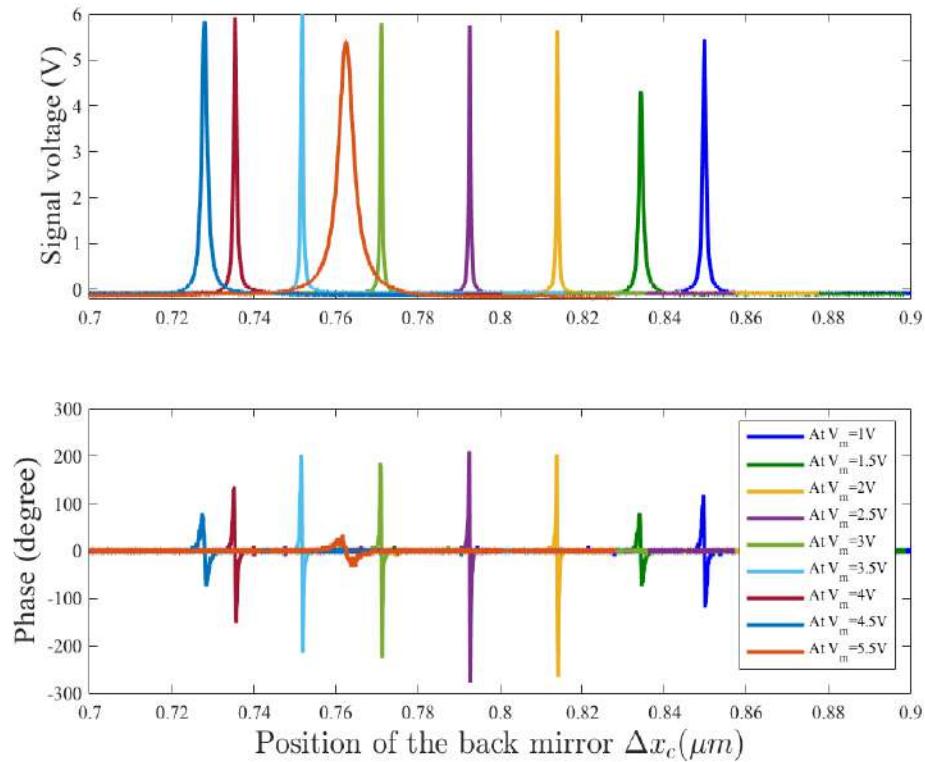


Figure 5.10: MIM cavity resonance as a function of the back mirror position. a) The MIM transmitted resonance at different membrane locations shows low finesse at $V_m = 5.5V$ and high finesse at $V_m = 2.5V$. b) It shows the phase of each resonance. The x-axis is calibrated by $\Delta V_c \alpha_c / \Delta t$.

finesse when the membrane changes its location resulting different losses at every value of Δx_m as shown in Figure. 5.10. The finesse is found by fitting all MIM cavity resonances at different membrane locations by Lorentzian to measure the width of each peak. The relative widths of cavity resonance are plotted as a function of the membrane position as shown in Figure 5.11 (top) and the finesse will be high for sharp resonance (narrow width) and low for

broad resonance (wide width). Figure 5.11(bottom) shows the experimental cavity response according to this model as a function of membrane position Δx_m for tuned back mirror position Δx_c . The former might be intuitively understood in terms of decreasing and increasing mode energies of the two sub-cavities with different finesse. Their coupling by transmission through the

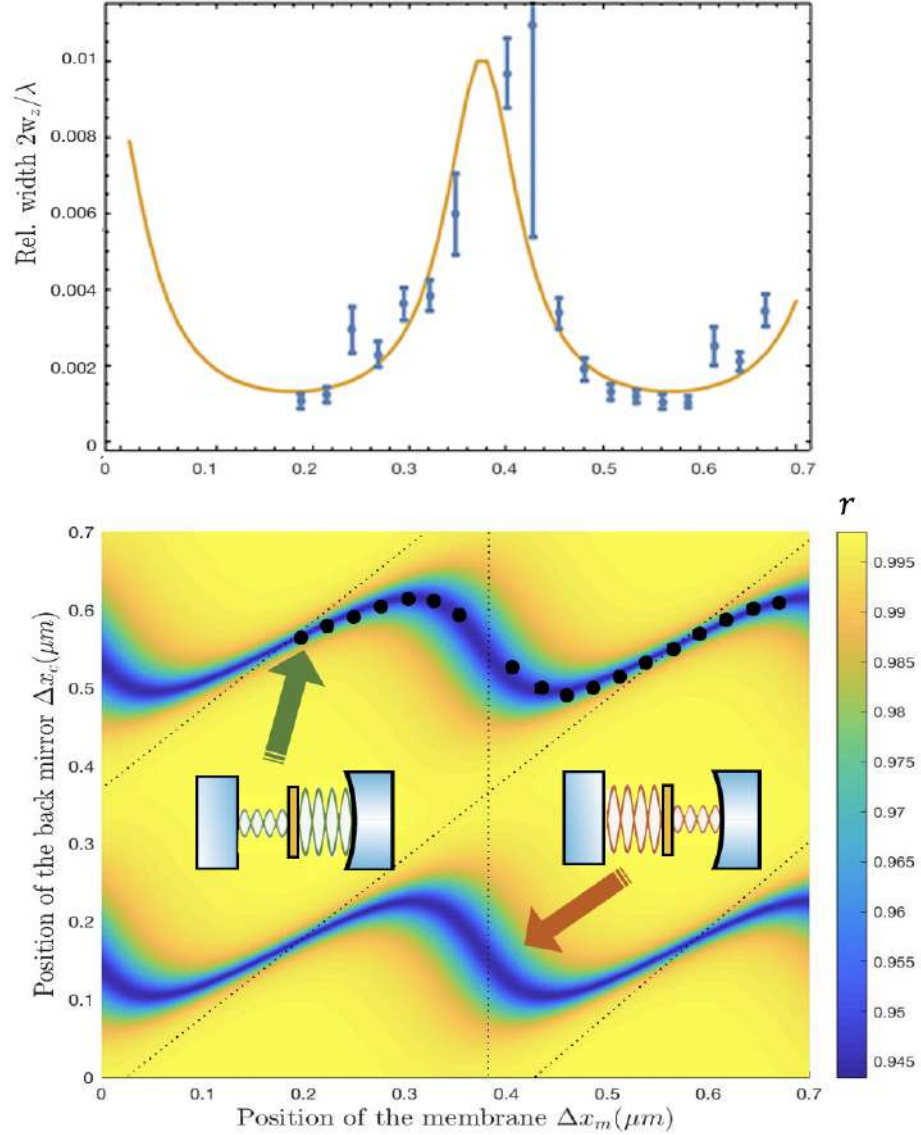


Figure 5.11: *Experimental data for resonance locations has been overlaid (black dots). Corresponding full linewidths, measured as mirror displacement w_z , are shown together with the theoretical expectation for an estimated $\eta_1 \approx 0.994$. We attribute deviations to spurious coupling to higher-order, transversal cavity modes.*

membrane leads to avoided crossings. As a result, resonant frequencies as well as cavity finesse oscillate as a function of membrane displacement Δx_m . This behaviour corresponds to the maximum field intensity alternating be-

tween both sub-cavities. As we discuss in Section 2.4, the theoretical model of the case of tuned mirror position, the mirror position does not influence the length of the front sub-cavity. Thus, the apparent linewidth of resonance is determined by a mixture of cavity decay rate and tuning behaviour. This case is used for comparison with experimental data also shown in Figure 5.11, where we used a fixed laser frequency referenced to an atomic transition within the ^{87}Rb D_1 -line manifold.

The strongest dispersive coupling to the membrane occurs when the back sub-cavity is resonant, while the front sub-cavity is anti-resonant ($L_{front} = \lambda/4 + m\lambda/2$ and $L_{back} + \Delta x_c = n\lambda/2$ with an integer m, n , see indicating arrow in Figure. 5.11 (bottom)).

For fixed loss, cavity response reaches its maximum exactly for the impedance matching condition in Equation 2.129. If maximal response is required, the front mirror reflectivity should thus be chosen for impedance matching [70]. The response then increases monotonously with η_1 and first-order expansion of the effective reflection coefficient 2.127 reduces to

$$Z_1 \approx i\chi\Delta x_m = 8\pi i \frac{\eta_1}{1 - \eta_1^2} \frac{r_2}{1 - r_2} \frac{\Delta x_m}{\lambda} \quad (5.7)$$

for $r_3 \approx 1$. This expression diverges for $\eta_1 \rightarrow 1$ or $r_2 \rightarrow 1$, which would both correspond to infinitely sharp resonance width. In scenarios where the interaction with the membrane should ideally be lossless, in particular, to retain the quantum properties of the input beam, the resonator should be undercoupled with a front mirror reflectivity much lower than the internal loss factor. For zero loss with $\eta_1 = r_3 = 1$, the response would be given by

$$Z_1 \approx -1 + 8\pi i \frac{1 + r_1}{1 - r_1} \frac{r_2}{1 - r_2} \frac{\Delta x_m}{\lambda} \quad (5.8)$$

From fitting the theoretical model to the experimentally obtained linewidths, (see Figure 5.11), we find an optical instability loss with $\eta_1 \approx 0.994$ in our present system that leads to operating close to the impedance matching condition because $\eta_1^2 \approx 0.988$ which is almost equal to the reflectivity of the front mirror of 0.99.

5.6 Mechanical Motion of the Membrane

To read out the mechanical motion of the membrane, the dispersive signal out of the voltage divider in Figure 4.17 is sent to the vector analyzer. By sweeping the frequency of the vector analyzer from 100 kHz-1MHz, we excite the membrane to different modes (mechanical modes) via Bias-T, see appendix D.1. The frequency of the mechanical modes can be calculated by Equation 2.75, they are shown in Table 5.1. In this measurement, the MIM cavity is locked

Mode number (i, j)	ω_{ij}
(1, 1)	$\omega_{11} = 2\pi \times 397.1 \text{ kHz}$
(1, 2)	$\omega_{12} = 2\pi \times 627.8 \text{ kHz}$
(2, 2)	$\omega_{22} = 2\pi \times 794.2 \text{ kHz}$
(3, 1)	$\omega_{31} = 2\pi \times 887.9 \text{ kHz}$

Table 5.1: Frequency of the membrane for different mode numbers (i, j).

on resonance to the laser. We shake the PZT of the membrane and read out the corresponding peaks to each mode as shown in Figure 5.16

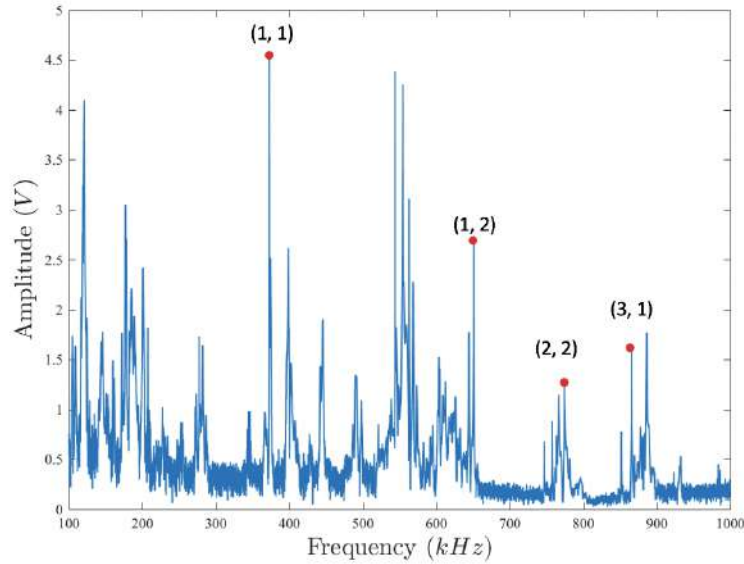


Figure 5.12: Mechanical modes of membrane for different frequencies. The modes of the membrane in Table 5.1 are indicated

5.7 Noise Measurements

To assess the suitability of our setup for quantum optical experiments, we observe and evaluate levels of measurement noise. The shot noise level should be measured which allows for calibration of the detection gain G_e , i.e. signal voltage per photon flux imbalance. In particular, we can observe thermal membrane motion, and compare it against laser frequency noise.

5.7.1 Measuring Photon Shot Noise

Photon shot noise is related to the light quantization that limits how precisely we can measure. photon shot noise has to be measured for allowing us to calibrate our signals, which is represented in the second term of Equation 2.171.

For signal detection, the BPD pair (Thorlabs model PDB210A) takes the difference between the two inputs' light intensities to produce a radio-frequency (RF) signal. The RF signal is measured with a frequency-dependent electronic gain G_e such that $U(t) = G_e S_z(t)$. To measure the shot noise level, the

reference beam is blocked by an iris and the laser is off-resonance which means there is no light that can be seen on the camera through cavity transmission. The balanced signal or RF signal is sent to a spectrum analyzer which takes the Fast Fourier Transformation (FFT) of that signal. The one-sided power spectral density is measured at different power with a with 500 Hz effective bandwidth (100 averages of 2 ms data). As shown in Figure. 5.13, the response below ≈ 80 kHz is limited by an additional high-pass filter. We typically observe spurious narrowband signals in the region below 100 kHz. Above 1 MHz, excess noise due to aliasing of higher frequencies at 2.5 MHz sampling rate becomes visible. The blue signal in Figure 5.13 shows the electrical noises only with no laser shin on the BPD.

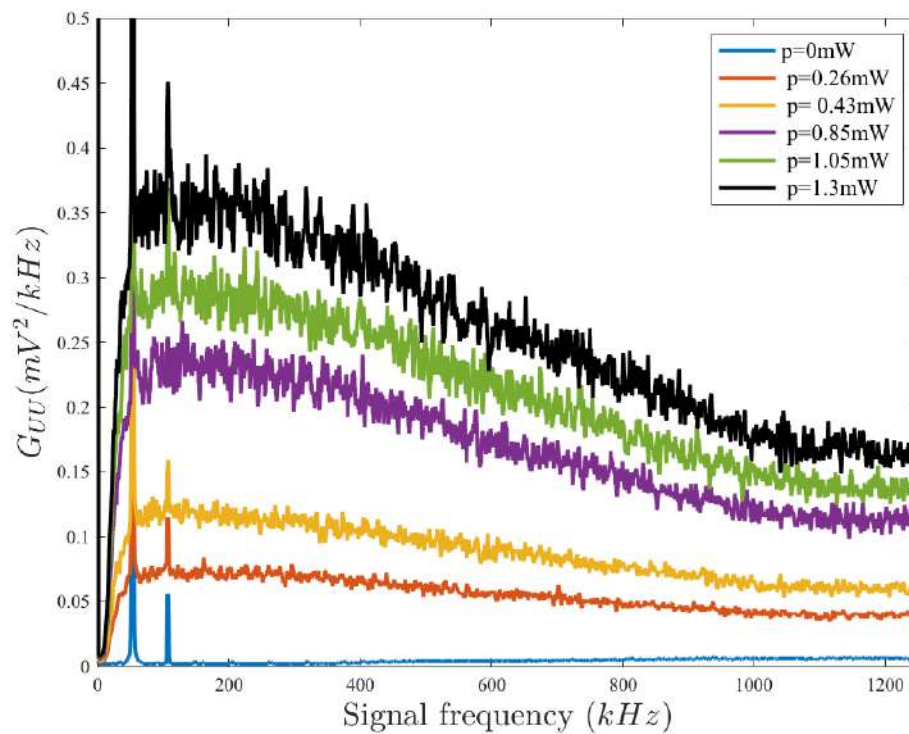


Figure 5.13: Shot noise limited detector response. The spectral response of our 1 MHz-bandwidth balanced detector to photon shot noise is plotted for different power. One-sided power spectral density $G_{UU}(|f|) = 2S_{UU}(f)$ was measured with a 100 Hz effective bandwidth.

The linear scaling with laser power (photon flux) is shown in Figure 5.14 for a single frequency of 125, 365, 395, 425 kHz of all these curves. The data

shows a linear increase in the noise power with the optical power. Thus, the BPD is photon shot noise-limited performance over its ≈ 1 MHz bandwidth assured by the noise power spectral density of the RF signal which must linearly grow with laser power.

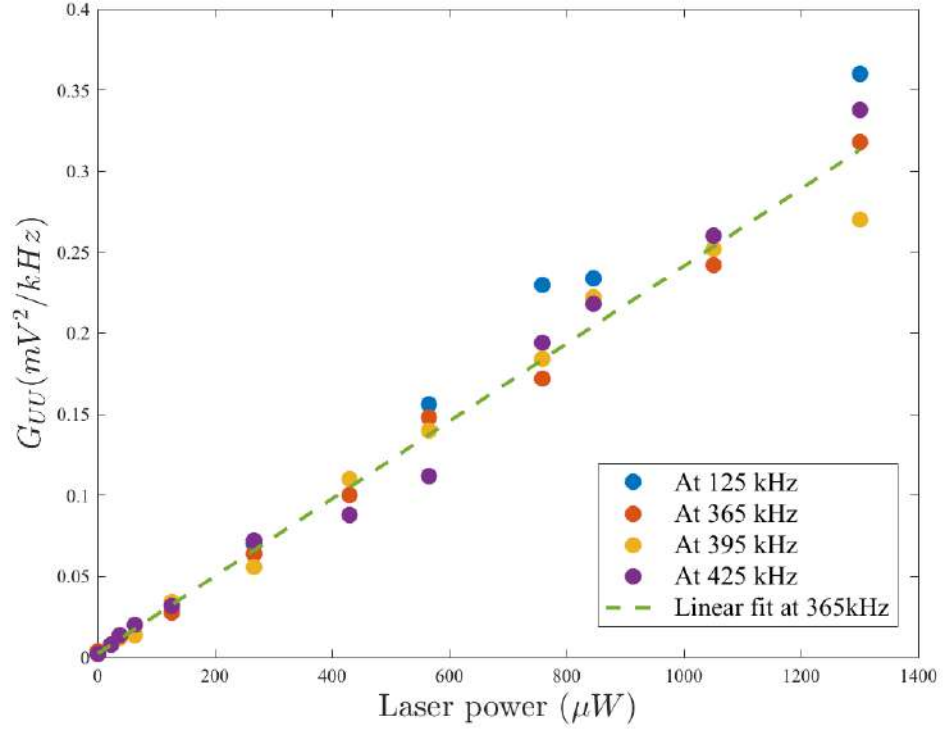


Figure 5.14: Noise power dependence of amplified photo-current noise at different frequency values. It is plotted versus light power which shows that the noise power will increase linearly with optical power.

The shot noise level allows for calibration of the electronic gain G_e , using Equation 2.171 and the photon flux arriving at the detector $\Phi_d = 2 \cos^2 \alpha \langle \hat{S}_0 \rangle = P_d \lambda / hc$ measured as light power P_d . The pure shot noise from the input light of power P_d with a quantum efficiency of the detector $\eta_d < 1$ leads to the electronic gain G_e and can be defined as

$$G_e = \sqrt{\frac{4S_{UU}}{\eta_d \Phi_d}} \quad (5.9)$$

As the quantum efficiency is $\eta_d = r_d hc / e \lambda$, the electronic gain becomes

$$G_e = \sqrt{\frac{4eS_{UU}}{r_d P_d}} \quad (5.10)$$

where $r_d = I/P_d$ is the detector responsivity which is defined as photo-current per incident optical power. For considering single-sided power spectral density $2S_{UU} = G_{UU}$ leads to

$$G_e = \sqrt{\frac{2eG_{UU}}{r_d P_d}} \quad (5.11)$$

From the linear scaling with laser power (photon flux) in Figure. 5.14, we find a slope of $G_{UU}/P_d = 2.4 \times 10^{-7} \text{ V}^2\text{Hz}^{-1}\text{W}^{-1}$ with an offset of $4.6 \times 10^{-12} \text{ V}^2\text{Hz}^{-1}$ due to electronic noise. The slope corresponds to a detection gain (voltage per photon flux) of $G_e \approx 3.70 \times 10^{-13} \text{ V/Hz}$, assuming a quantum efficiency of $\eta_d = 0.88$ corresponding to a detector responsivity of $r_d = 0.56 \text{ A/W}$ at $\lambda = 795 \text{ nm}$ which is taken from the photodetector data sheet.

5.7.2 Measuring the Thermal Noise of the Membrane

To observe the thermal noise, the laser power that is sent to the MIM cavity is in a few microwatts to avoid membrane over-oscillation and the reference beam has more power than the signal beam. Then, the MIM cavity is locked on resonance (here done by stabilizing the cavity length) and the thermal noise can be read out on the BPD.

The power spectral density of the BPD output or the polarimeter S_z -signal exhibits distinct features that we can identify with thermally excited modes of oscillation of the square membrane (Brownian motion), see Figure 5.15. The frequencies are consistent with the modes of an almost square membrane, matching the expected fundamental frequency $\omega_m = 2\pi \times 397 \text{ kHz}$ as shown in Figure 5.16 with membrane under a tensile stress of $\mathcal{T} \approx 1 \text{ GPa}$ and with a density $\rho_m \approx 3.17 \text{ g/cm}^3$.

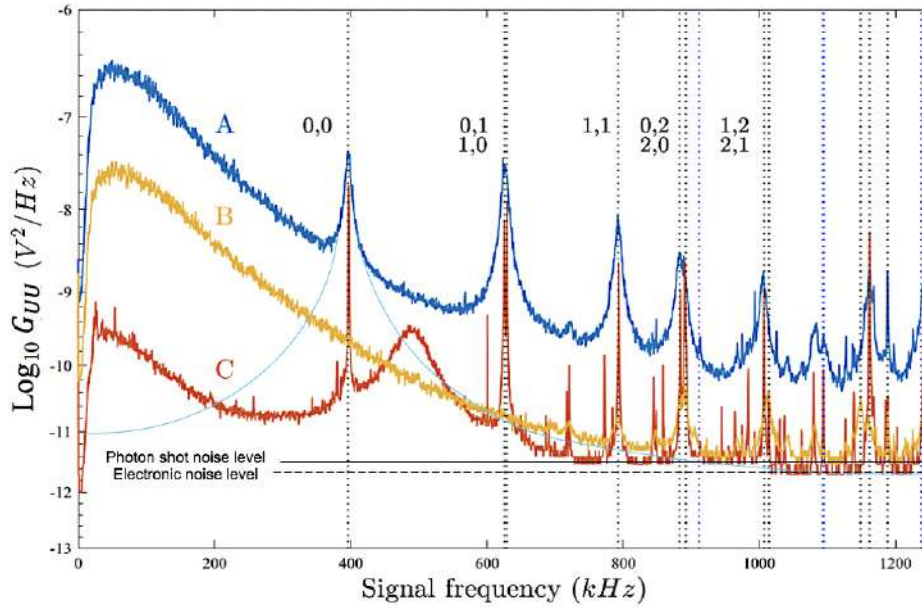


Figure 5.15: Thermal noise of the membrane is detected for dispersive coupling (trace A). For membrane positions near minimal dispersive coupling (trace B), only higher-order membrane modes remain visible. Here, the combined level (black line) of photon shot noise ($\approx 1.0 \times 10^{-12} \text{ V}^2/\text{Hz}$) and electronic noise ($\approx 2.3 \times 10^{-12} \text{ V}^2/\text{Hz}$) near 400 kHz at a total light power of $8.3 \mu\text{W}$ is just above the electronic noise (dashed line). For improved conditions (trace C) with lower membrane damping (lower vacuum pressure) and reduced laser frequency noise, signal-to-noise-ratio improves and near-degenerate modes can be resolved. For comparison, (aliased) expected mode frequencies for an almost square membrane (1.01 side ratio) with a fundamental frequency of 397.5 kHz are indicated.

Due to relatively high residual vacuum pressure, the damping rate of the membrane oscillations is relatively high in this measurement, with a full-width half maximum (FWHM) $\gamma_m \approx 2\pi \times 10.3 \text{ kHz}$. From a model fit to the experimental data, we find a contribution of the membrane's fundamental mode to the variance of the signal voltage of $\sigma^2 = 1.25 \times 10^{-3} \text{ V}^2$. It compares very well with the expected thermal variance of

$$\sigma_{f_m}^2 = \frac{G_e^2 \eta_d^2 \sin 2\alpha \langle \hat{S}_{0,\text{in}} \rangle^2 \chi^2 k_B T}{M(2\pi f_m)^2} \quad (5.12)$$

is approximated to be $1.4 \times 10^{-3} \text{ V}^2$ for $T = 300\text{K}$ an input power of $P \approx 11.1 \mu\text{W}$ with a measured polarisation angle of $\alpha \approx 37.5^\circ$. The observed variance is lower than theoretically estimated as we did not include reduced

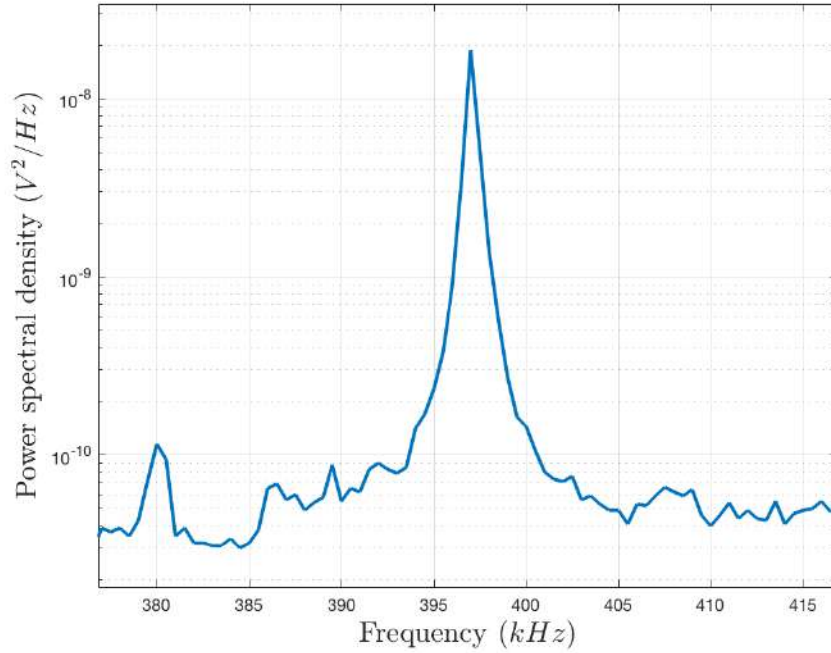


Figure 5.16: *Fundamental mode of membrane ω_{11} at 397 kHz at lowered vacuum pressure.*

mode overlap and transversal misalignment of the membrane with respect to the optical TEM_{00} mode. The membrane features mostly vanish when the membrane is positioned at points of minimal dispersive coupling. Some higher-order membrane modes remain visible, which is likely due to weakly coupled transversal cavity modes.

Compared to room-temperature thermal noise, the variance of the membrane's quantum fluctuations will be approximately 6 orders of magnitude smaller. In the present setup, these are masked by coloured broadband noise, well above the photon shot noise level. It results from frequency fluctuations of the illuminating laser.

To show that the thermal noise of the membrane is proportional to the signal and reference power, the thermal noise is measured by fixing the total power at $150\mu\text{W}$ and $300\mu\text{W}$ but varying the power ratio between the reference and signal beams. In this measurement, the reference power is reduced and the signal power is increased, it is clearly seen that the technical noise

is increased which arises from the technical components of the laser system, such as fluctuations in the power supply, temperature changes, and mechanical vibrations. That means the technical noise is also proportional to the signal and reference power and that is shown in Figure. 5.17 where the blue signal noise shows less noise than the purple signal.

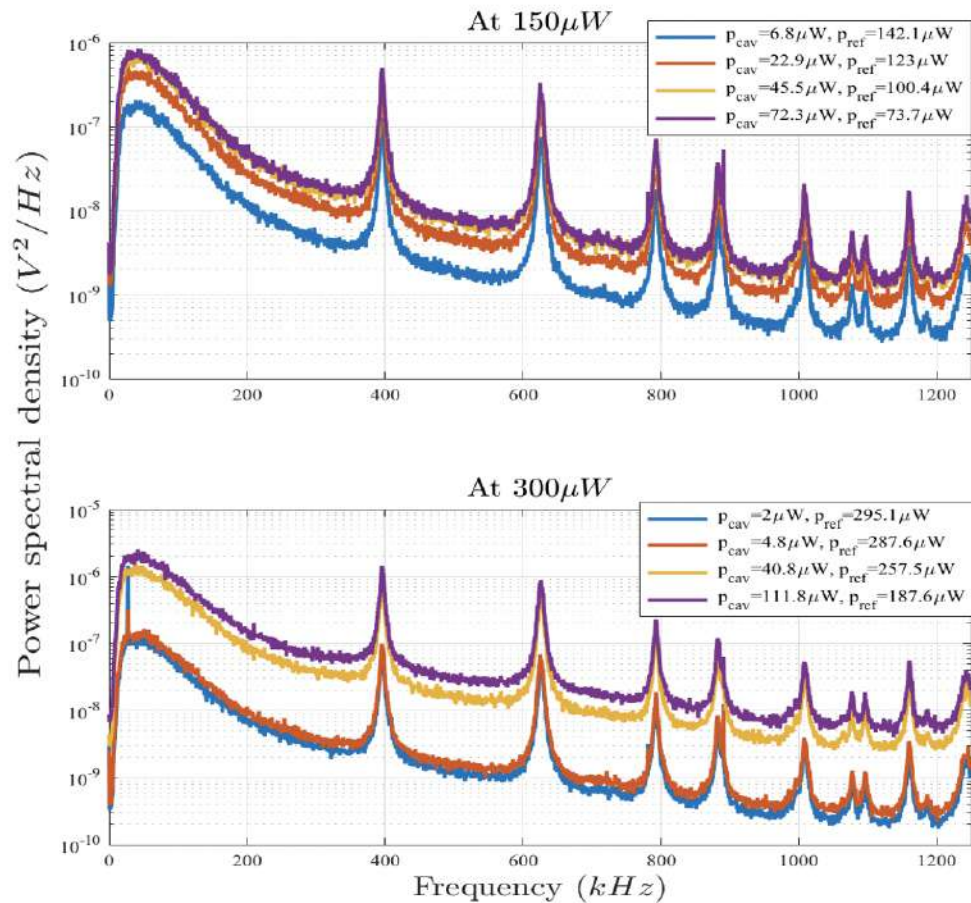


Figure 5.17: Thermal noise measurement at 150 μW and 300 μW. The measurement is taken by fixing the total power and changing the ratio between the signal beam power and reference beam power.

The membrane noise power divided by reference power versus the signal power must be linear as shown in Figure 5.18. At the total power 150 μW, the membrane noise near 379 kHz is linear which means it is proportional to the signal and reference power. However, the membrane noise near 379 kHz (yellow signal) at the total power 300 μW seems to be saturating our RF electronics

and it is not linear any more. It concludes that we should measure at power well below $300 \mu\text{W}$.

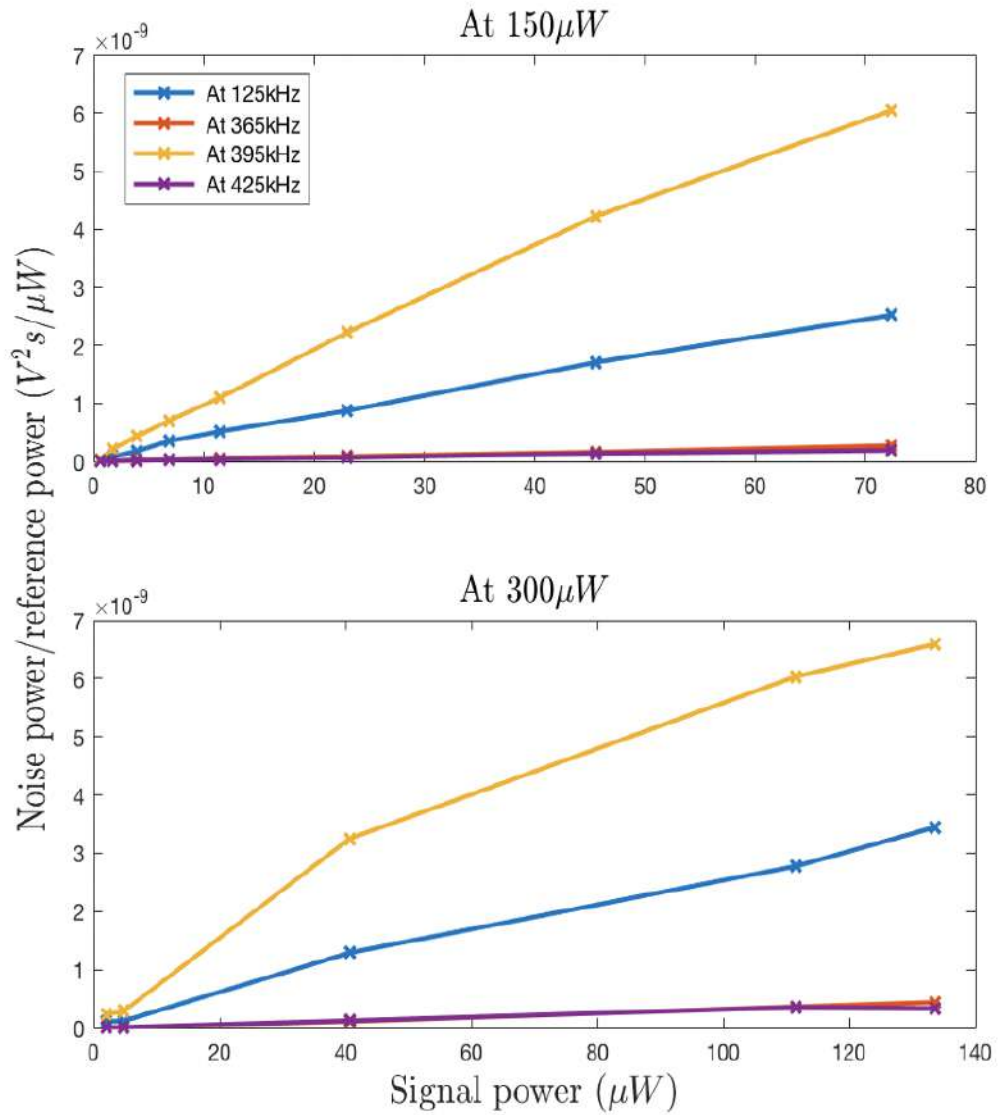


Figure 5.18: The ratio of the noise power and reference power at $150 \mu\text{W}$ and $300 \mu\text{W}$ which is proportional to the cavity signal power.

5.8 Discussion of laser noise and improvement with filter cavity

The laser noise adds an additional noise when the cavity is off-resonance and only the light reflected from the cavity is sent to the detector. This noise is beyond the shot noise and it originates from the laser frequency fluctuations. To improve the thermal noise measurement, the laser beam is sent through a filter cavity to get rid of all high frequencies. The filter cavity has to be sharper than 397kHz because we want to see the fundamental membrane oscillation. Thus, the linewidth of the filter cavity has to be less than 397kHz . The filter cavity is chosen to be a symmetric cavity with high reflectivity 99.95% . The finesse of the filter cavity is calculated to be 3140 with $L_{cavity} = 180\text{mm}$, and $\text{FSR} = 833\text{MHz}$. The transmission of the filter cavity is sent to the MIM optical cavity which provides us with improved measurements. Figure 5.15 (trace C) shows a signal trace for reduced frequency noise as the laser was passed through a filter cavity of $\approx 160\text{kHz}$ linewidth. Excess noise in the region of $\approx 500\text{kHz}$ arises from the active stabilisation loop (servo bump). In addition, the vacuum pressure was reduced, which decreased membrane damping to $\gamma_m \approx 2\pi \times 480\text{Hz}$ and thus contributes a factor of ≈ 20 to the improvement in signal-to-noise ratio (SNR).

An analysis is similar to Section. 2.4 shows that the first-order response to laser frequency fluctuations for maximal dispersive coupling matched impedance and $r_3 \approx 1$ is given by

$$i\chi_f = \frac{\partial Z_1}{\partial \Delta f} \approx -\frac{4\pi i}{c} \frac{(1-r_2)L_1 + (1+r_2)L_2}{1-r_2} \frac{\eta_1}{1-\eta_1^2}, \quad (5.13)$$

and will be suppressed for shorter resonator lengths. The decrease of this noise for minimal dispersive coupling is consistent with the increase in cavity linewidth and thus reduced frequency response.

To have a strong coupling regime the quantum noise of the membrane has to be larger than the photon shot noise level whereas it will be weak if the quantum noise of the membrane is smaller than the photon shot noise level. Also, the coupling will be equal to 1 if both are equal and that is the starting point toward a strong coupling regime.

Our measurement is still in the weak coupling regime, but since signal power scales quadratically with laser power while photon shot noise increases linearly, the optomechanical coupling strength increases with power. Technical frequency noise power also scales quadratically, such that it will be possible to observe quantum noise more easily for a higher-order mode of the membrane's vibrations at higher signal frequencies where the technical noise will drop below the shot-noise level, see Figure 5.15. However, increased light power also leads to back-action noise and cooling or heating of the membrane via radiation pressure. Lastly, the interaction strength has to be maximized to have a strong coupling regime which requires more laser power and an additional cooling laser.

Chapter 6

Conclusion and future work

In conclusion, this thesis has presented the development and demonstration of an interferometrically stable polarisation interferometer that converts the phase shift from an optical resonator into beam polarization. This device can be directly used to stabilise the laser-resonator detuning without the need for laser modulation. Here, we applied it to detecting the microscopic motion of a micro-mechanical membrane. The potential for light-membrane interaction at the quantum level was explored with sufficiently reduced laser frequency noise or reduced frequency response from a shorter cavity, making this arrangement a powerful tool for hybrid quantum systems development. Depending on the intended protocol, the cavity design should consider whether a maximally coupled read-out of membrane motion or minimal optical loss is required. The current cavity design uses a plane parallel entrance mirror, which leads to diffraction loss between that mirror and the membrane and results in impedance-matched coupling.

To extend this optomechanical system, the optical loss has to be minimized by replacing the front mirror of the optical cavity with a concave mirror to make the sub-cavity optically stable when operating in the under-coupled regime. For a mode-matched input beam, alignment to the reference beam will

remain the same as the mirror will act as a field lens in the focal plane of the imaging lens for beam displacement. The membrane modes can also be cooled down directly using the dispersive signal but with a carefully adjusted phase. combined with cold atoms experiments such as a polarisation interferometer shows the potential to form a strong spin-membrane coupling. This paves the way for mutual cooling between the membrane and neutral atoms.

Concluding this dissertation, I have presented both the theoretical and experimental aspects of a stable polarisation interferometer. This work is expected to be useful in future studies and may guide exciting future discoveries and commercial products in the field of optomechanics.

Bibliography

- [1] “Stoichiometric silicon nitride membranes.” [Online]. Available: <https://www.norcada.com/products/high-q-si3n4-membrane/>
- [2] J. D. Wilson and A. J. Buffa, *Física*. Pearson Educación, 2002.
- [3] G. Kurizki, P. Bertet, Y. Kubo, and J. Schmiedmayer, “Quantum technologies with hybrid systems,” *PNAS*, vol. 112, no. 13, pp. 3866–3873, 2015.
- [4] P.-L. Yu, “Quantum optomechanics with engineered membrane resonators,” Ph.D. dissertation, University of Colorado, 2016.
- [5] M. J. Underwood III, “Cryogenic optomechanics with a silicon nitride membrane,” Ph.D. dissertation, Yale University, 2016.
- [6] J. Thompson, B. Zwickl, A. Jayich, F. Marquardt, S. Girvin, and J. Harris, “Strong dispersive coupling of a high-finesse cavity to a micromechanical membrane,” *Nature*, vol. 452, no. 7183, pp. 72–75, 2008.
- [7] D. J. Wilson, C. A. Regal, S. B. Papp, and H. Kimble, “Cavity optomechanics with stoichiometric sin films,” *Physical review letters*, vol. 103, no. 20, p. 207204, 2009.
- [8] R. A. Norte, J. P. Moura, and S. Gröblacher, “Mechanical resonators for quantum optomechanics experiments at room temperature,” *Physical review letters*, vol. 116, no. 14, p. 147202, 2016.
- [9] C. Reinhardt, T. Müller, A. Bourassa, and J. C. Sankey, “Ultralow-noise sin trampoline resonators for sensing and optomechanics,” *Physical Review X*, vol. 6, no. 2, p. 021001, 2016.
- [10] Y. Tsaturyan, A. Barg, E. S. Polzik, and A. Schliesser, “Ultracoherent nanomechanical resonators via soft clamping and dissipation dilution,” *Nature nanotechnology*, vol. 12, no. 8, pp. 776–783, 2017.
- [11] A. H. Ghadimi, S. A. Fedorov, N. J. Engelsen, M. J. Breyhi, R. Schilling, D. J. Wilson, and T. J. Kippenberg, “Elastic strain engineering for ultralow mechanical dissipation,” *Science*, vol. 360, no. 6390, pp. 764–768, 2018.
- [12] M. Bhattacharya, H. Uys, and P. Meystre, “Optomechanical trapping and cooling of partially reflective mirrors,” *Physical Review A*, vol. 77, no. 3, p. 033819, 2008.

- [13] T. Bagci, “Cavity optomechanics with high q mechanical resonators,” 2010.
- [14] K. Hammerer, A. S. Sørensen, and E. S. Polzik, “Quantum interface between light and atomic ensembles,” *Reviews of Modern Physics*, vol. 82, p. 1041, 2010.
- [15] C. A. Muschik, K. Hammerer, E. S. Polzik, , and J. I. Cirac, “Quantum teleportation of dynamics and effective interactions between remote systems,” *Physical Review Letters*, vol. 111, p. 020501, 2013.
- [16] H. Krauter, C. A. Muschik, K. Jensen, W. Wasilewski, J. M. Petersen, J. I. Cirac, and E. S. Polzik, “Entanglement generated by dissipation and steady state entanglement of two macroscopic objects,” *Physical Review Letters*, vol. 107, p. 080503, 2011.
- [17] H. Krauter, D. Salart, C. A. Muschik, J. M. Petersen, H. Shen, T. Fernholz, , and E. S. Polzik, “Deterministic quantum teleportation between distant atomic objects,” *Nature Physics*, vol. 9, pp. 400–404, 2013.
- [18] C. B. Møller, R. A. Thomas, G. Vasilakis, E. Zeuthen, Y. Tsaturyan, M. Balabas, K. Jensen, A. Schliesser, K. Hammerer, and E. S. Polzik, “Quantum back-action-evading measurement of motion in a negative mass reference frame,” *Nature*, vol. 547, no. 7662, pp. 191–195, 2017.
- [19] R. A. Thomas, M. Parniak, C. Østfeldt, C. B. Møller, C. Bærentsen, Y. Tsaturyan, A. Schliesser, J. Appel, E. Zeuthen, and E. S. Polzik, “Entanglement between distant macroscopic mechanical and spin systems,” *Nature Physics*, vol. 17, pp. 228–233, 2021.
- [20] T. M. Karg, B. Gouraud, C. T. Ngai, G.-L. Schmid, K. Hammerer, and P. Treutlein, “Light-mediated strong coupling between a mechanical oscillator and atomic spins 1 meter apart,” *Science*, vol. 369, no. 6500, pp. 174–179, 2020.
- [21] G.-L. Schmid, C. T. Ngai, M. Ernzer, M. Bosch Aguilera, T. M. Karg, and P. Treutlein, “Coherent feedback cooling of a nanomechanical membrane with atomic spins,” *Physical Review X*, vol. 12, p. 011020, 2011.
- [22] M. Korppi, A. Jöckel, M. T. Rakher, S. Camerer, D. Hunger, T. W. Hänsch, and P. Treutlein, “Hybrid atom-membrane optomechanics,” in *EPJ Web of Conferences*, vol. 57. EDP Sciences, 2013, p. 03006.
- [23] F. L. Pedrotti, L. M. Pedrotti, and L. S. Pedrotti, *Introduction to optics*. Cambridge University Press, 2017.
- [24] P. W. Milonni and J. H. Eberly, *Laser physics*. John Wiley & Sons, 2010.
- [25] C. A. Bennett, *Principles of physical optics*. John Wiley & Sons, 2022.
- [26] H. Kogelnik and T. Li, “Laser beams and resonators,” *Applied optics*, vol. 5, no. 10, pp. 1550–1567, 1966.
- [27] A. E. Siegman, *Lasers*. University science books, 1986.

- [28] R. Hodajerdi, “Production cavity and central optics for a light shining through a wall experiment,” Deutsches Elektronen-Synchrotron (DESY), Tech. Rep., 2015.
- [29] A. Gerrard and J. M. Burch, *Introduction to matrix methods in optics*. Courier Corporation, 1994.
- [30] D. Meschede, *Optics, light and lasers: the practical approach to modern aspects of photonics and laser physics*. John Wiley & Sons, 2017.
- [31] A. Lipson, S. G. Lipson, and H. Lipson, *Optical physics*. Cambridge University Press, 2010.
- [32] X. Mercier, P. Desgroux, G. Berden, and R. Engeln, *Cavity ring-down spectroscopy for combustion studies*. Wiley-Blackwell Chichester, UK, 2009.
- [33] H. Labuhn, “Laser frequency stabilization on an ultra-stable fabry-perot cavity for rydberg atom experiments,” Ph.D. dissertation, Diploma thesis handed into Department of Physics and Astronomy, University . . . , 2013.
- [34] U. A. Bakshi and L. A. V. Bakshi, *Transmission Lines & Waveguides*. Technical Publications, 2020.
- [35] J. Bird, *Electrical circuit theory and technology*. Routledge, 2017.
- [36] W. Nagourney, *Quantum electronics for atomic physics and telecommunication*. OUP Oxford, 2014.
- [37] S. L. Garrett, *Understanding Acoustics: An Experimentalist’s View of Acoustics and Vibration*. Springer, 2017.
- [38] L. D. Landau and E. M. Lifshitz, *Mechanics: Volume 1*. Butterworth-Heinemann, 1976, vol. 1.
- [39] M. Aspelmeyer, T. J. Kippenberg, and F. Marquardt, “Cavity optomechanics,” *Reviews of Modern Physics*, vol. 86, no. 4, p. 1391, 2014.
- [40] P. R. Saulson, “Thermal noise in mechanical experiments,” *Physical Review D*, vol. 42, no. 8, p. 2437, 1990.
- [41] J. J. Sakurai and E. D. Commins, “Modern quantum mechanics, revised edition,” 1995.
- [42] N. Zettili, “Quantum mechanics: concepts and applications,” 2003.
- [43] A. D. O’Connell, M. Hofheinz, M. Ansmann, R. C. Bialczak, M. Lenander, E. Lucero, M. Neeley, D. Sank, H. Wang, M. Weides *et al.*, “Quantum ground state and single-phonon control of a mechanical resonator,” *Nature*, vol. 464, no. 7289, pp. 697–703, 2010.
- [44] J. Chan, T. Alegre, A. H. Safavi-Naeini, J. T. Hill, A. Krause, S. Gröblacher, M. Aspelmeyer, and O. Painter, “Laser cooling of a nanomechanical oscillator into its quantum ground state,” *Nature*, vol. 478, no. 7367, pp. 89–92, 2011.

- [45] J. D. Teufel, T. Donner, D. Li, J. W. Harlow, M. Allman, K. Cicak, A. J. Sirois, J. D. Whittaker, K. W. Lehnert, and R. W. Simmonds, “Sideband cooling of micromechanical motion to the quantum ground state,” *Nature*, vol. 475, no. 7356, pp. 359–363, 2011.
- [46] A. Weinstein, C. Lei, E. Wollman, J. Suh, A. Metelmann, A. Clerk, and K. Schwab, “Observation and interpretation of motional sideband asymmetry in a quantum electromechanical device,” *Physical Review X*, vol. 4, no. 4, p. 041003, 2014.
- [47] T. Purdy, P.-L. Yu, N. Kampel, R. Peterson, K. Cicak, R. Simmonds, and C. Regal, “Optomechanical raman-ratio thermometry,” *Physical Review A*, vol. 92, no. 3, p. 031802, 2015.
- [48] M. Yuan, V. Singh, Y. M. Blanter, and G. A. Steele, “Large cooperativity and microkelvin cooling with a three-dimensional optomechanical cavity,” *Nature communications*, vol. 6, no. 1, pp. 1–6, 2015.
- [49] M. Underwood, D. Mason, D. Lee, H. Xu, L. Jiang, A. Shkarin, K. Børkje, S. Girvin, and J. Harris, “Measurement of the motional sidebands of a nanogram-scale oscillator in the quantum regime,” *Physical Review A*, vol. 92, no. 6, p. 061801, 2015.
- [50] F. Lecocq, J. B. Clark, R. W. Simmonds, J. Aumentado, and J. D. Teufel, “Quantum nondemolition measurement of a nonclassical state of a massive object,” *Physical Review X*, vol. 5, no. 4, p. 041037, 2015.
- [51] E. E. Wollman, C. Lei, A. Weinstein, J. Suh, A. Kronwald, F. Marquardt, A. A. Clerk, and K. Schwab, “Quantum squeezing of motion in a mechanical resonator,” *Science*, vol. 349, no. 6251, pp. 952–955, 2015.
- [52] M. Aspelmeyer, T. J. Kippenberg, and F. Marquardt, “Cavity optomechanics,” *Reviews of Modern Physics*, vol. 86, no. 4, p. 1391, 2014.
- [53] M. Korppi, “Optomechanical coupling between ultracold atoms and a membrane oscillator,” Ph.D. dissertation, University_of_Basel, 2014.
- [54] E. Verhagen, S. Deléglise, S. Weis, A. Schliesser, and T. J. Kippenberg, “Quantum-coherent coupling of a mechanical oscillator to an optical cavity mode,” *Nature*, vol. 482, no. 7383, pp. 63–67, 2012.
- [55] B. Kraus, K. Hammerer, G. Giedke, and J. I. Cirac, “Entanglement generation and hamiltonian simulation in continuous-variable systems,” *Physical Review A*, vol. 67, no. 4, p. 042314, 2003.
- [56] J. D. Teufel, T. Donner, M. Castellanos-Beltran, J. W. Harlow, and K. W. Lehnert, “Nanomechanical motion measured with an imprecision below that at the standard quantum limit,” *Nature nanotechnology*, vol. 4, no. 12, pp. 820–823, 2009.
- [57] T. P. Purdy, P.-L. Yu, R. W. Peterson, N. S. Kampel, and C. A. Regal, “Strong optomechanical squeezing of light,” *Physical Review X*, vol. 3, no. 3, p. 031012, 2013.

- [58] K. W. Murch, K. L. Moore, S. Gupta, and D. M. Stamper-Kurn, “Observation of quantum-measurement backaction with an ultracold atomic gas,” *Nature Physics*, vol. 4, no. 7, pp. 561–564, 2008.
- [59] F. Brennecke, S. Ritter, T. Donner, and T. Esslinger, “Cavity optomechanics with a bose-einstein condensate,” *Science*, vol. 322, no. 5899, pp. 235–238, 2008.
- [60] G. S. Agarwal, *Quantum optics*. Cambridge University Press, 2012.
- [61] A. M. Fox, M. Fox *et al.*, *Quantum optics: an introduction*. Oxford university press, 2006, vol. 15.
- [62] G. D. Sucha and W. H. Carter, “Focal shift for a gaussian beam: an experimental study,” *Applied Optics*, vol. 23, no. 23, pp. 4345–4347, 1984.
- [63] P. Antonio, “Stabilized optomechanical systems for quantum optics,” Ph.D. dissertation, University of Trento, 2014.
- [64] L. Chen, “A pound-drever-hall based repetition rate stabilization technique for mode-locked lasers,” Ph.D. dissertation, University of Colorado, 2017.
- [65] R. Drever, J. L. Hall, F. Kowalski, J. Hough, G. Ford, A. Munley, and H. Ward, “Laser phase and frequency stabilization using an optical resonator,” *Applied Physics B*, vol. 31, no. 2, pp. 97–105, 1983.
- [66] K. Warwick, *An introduction to control systems*. World Scientific, 1996, vol. 8.
- [67] M. A. Haidekker, *Linear Feedback Controls (Second Edition)12 - Frequency-domain analysis and design methods*. Elsevier, 2020.
- [68] P. E. Barclay, K. Srinivasan, O. Painter, B. Lev, and H. Mabuchi, “Integration of fiber-coupled high-q silicon microdisks with atom chips,” *Applied physics letters*, vol. 89, no. 13, p. 131108, 2006.
- [69] B. Zwickl, W. Shanks, A. Jayich, C. Yang, A. Bleszynski Jayich, J. Thompson, and J. Harris, “High quality mechanical and optical properties of commercial silicon nitride membranes,” *Applied Physics Letters*, vol. 92, no. 10, p. 103125, 2008.
- [70] J. H. Chow, I. C. M. Littler, D. S. Rabeling, D. E. McClelland, and M. B. Gray, “Using active resonator impedance matching for shot-noise limited, cavity enhanced amplitude modulated laser absorption spectroscopy,” *Optics Express*, vol. 16, no. 11, pp. 7726–7738, 2008.
- [71] J. Sólnes, *Stochastic processes and random vibrations: theory and practice*. John Wiley & Sons, 1997.
- [72] H. Haus, “Waves and fields in optoelectronics.” PRENTICE-HALL, INC., ENGLEWOOD CLIFFS, NJ 07632, USA, 1984, 402, 1984.
- [73] W. B. Davenport, W. L. Root *et al.*, *An introduction to the theory of random signals and noise*. McGraw-Hill New York, 1958, vol. 159.

Appendix A

Mathematical Tools

A.1 Fast Fourier Transformation

The fast Fourier transform (FFT) is an efficient algorithm for calculating a sequence's discrete Fourier transform (DFT) or its inverse. The FFT is extensively utilised in a variety of applications, including signal processing, data analysis, and scientific computing because of its ability to compute the DFT of an enormous body of data. Useful references can be found in [71, 72]

This chapter discusses the definition of the transform and begins introducing some of the ways it is useful. Let's assume that we have a complex function of time $x(t)$ represents a physical process. The Fourier transform (FT) is defined as [73]

$$x(w) = \int_{-\infty}^{\infty} x(t)e^{-iwt} dt \quad (\text{A.1})$$

and inverse Fourier transform (IFT) can be expressed as

$$x(t) = \int_{-\infty}^{\infty} x(w)e^{-iwt} dw/2\pi \quad (\text{A.2})$$

where $w = 2\pi f$ is the angular frequency The signal should have finite energy (i.e. $E < \infty$) and the total energy of the signal is given by

$$E = \int_{-\infty}^{\infty} |x(t)|^2 dt \quad (\text{A.3})$$

Thus, the power of the signal should be zero but most useful functions have no zero power

$$P = \langle x(t)^2 \rangle = \lim_{T \rightarrow \infty} \frac{1}{T} \int_{-T/2}^{T/2} |x(t)|^2 dt = 0 \quad (\text{A.4})$$

Using Parseval's theorem allows us to compute the total energy in the frequency domain with units of $[x]/Hz$ as

$$E = \int_{-\infty}^{\infty} |x(w)|^2 dw / 2\pi \quad (\text{A.5})$$

The quantity $|x(w)|^2$ has units of $[x]^2/Hz^2$ and it represents the double-sided energy spectral density. Double-sided means there are positive and negative frequencies which are involved in the normalization of the density function.

A random function $x(t)$ is an example of a function that has no zero power. Thus, it can be described by any noisy process like electrons flow in a resistor or Brownian motion in a cantilever. In this case, $x(t)$ is illustrated by one of its statistical measures. let's $x(t)$ be real function with time-shifted value as $x(t + \tau)$. The Fourier transform of statistical measure is the auto-correlation of $x(t)$ defined as double-sided power spectral density as

$$S_{UU} = \int_{-\infty}^{\infty} \langle x(t)x(t + \tau) \rangle e^{-i\omega\tau} d\tau \quad (\text{A.6})$$

$$\langle x^2(t) \rangle = \int_{-\infty}^{\infty} S_{UU}(w) dw / 2\pi \quad (\text{A.7})$$

from this property, we can define the single-sided power spectral density as

$$G_{UU}(w) = 2S_{UU}(w) \quad (\text{A.8})$$

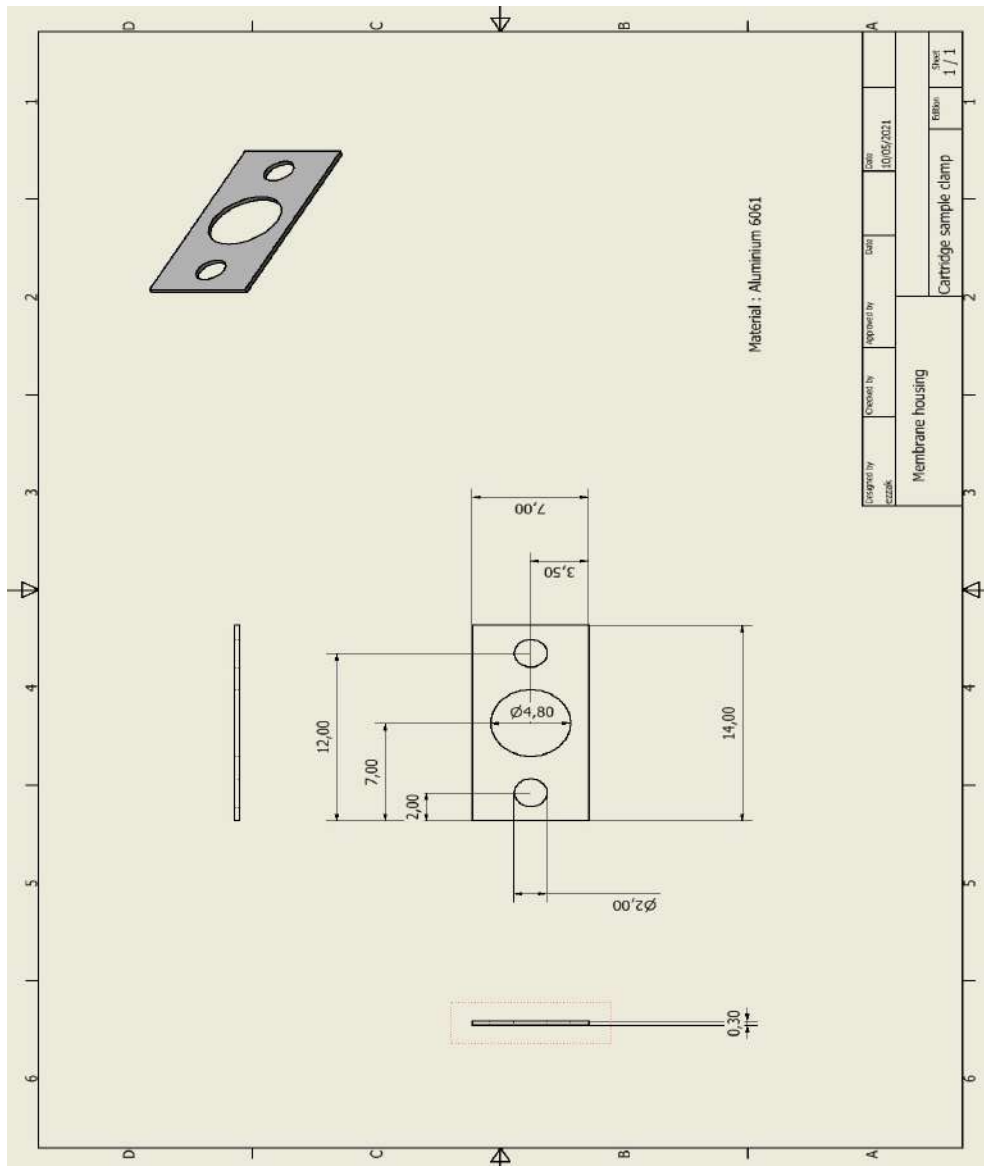
thus

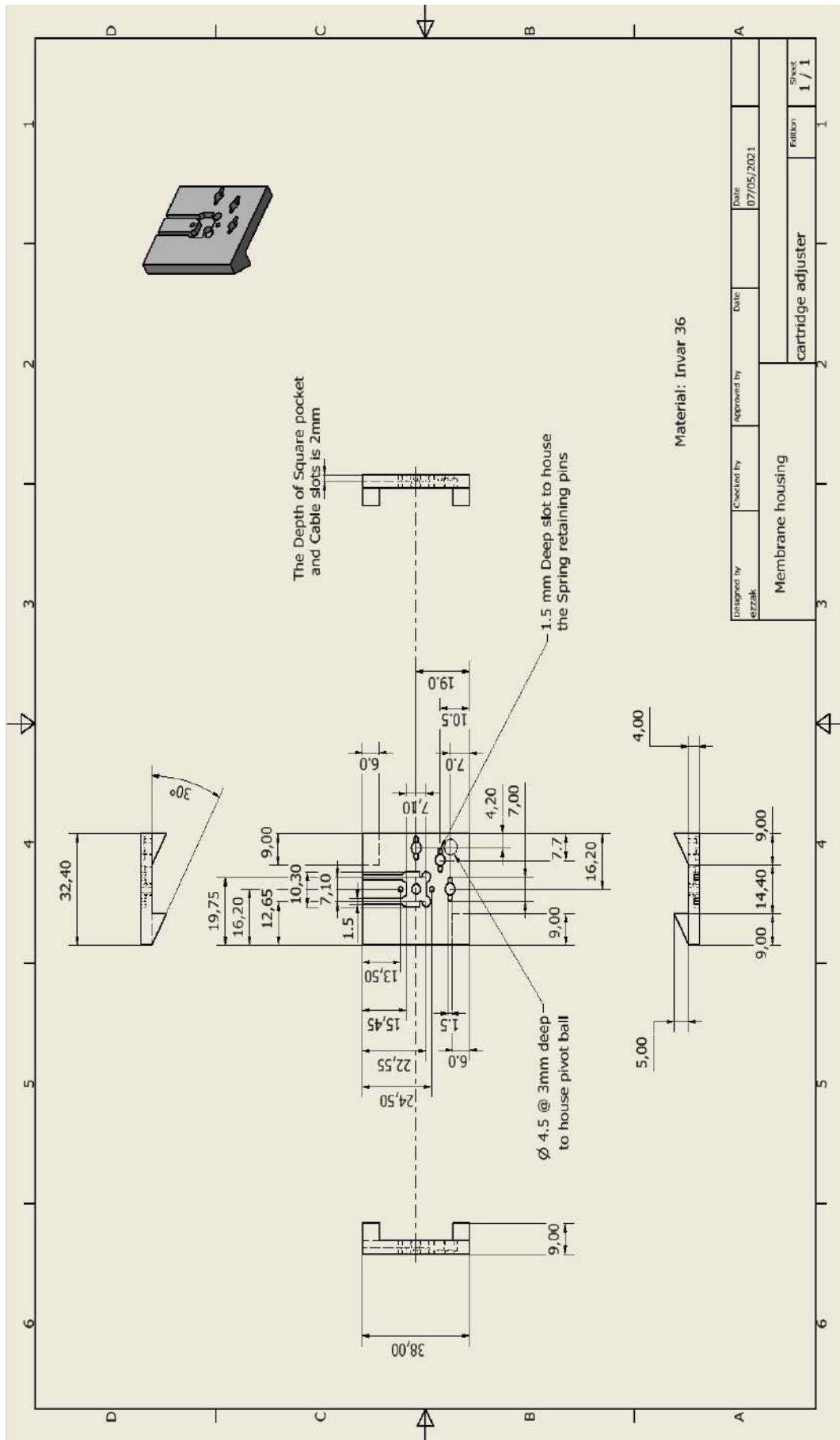
$$\langle x^2(t) \rangle = \int_0^{\infty} G_{UU}(w) dw / 2\pi \quad (\text{A.9})$$

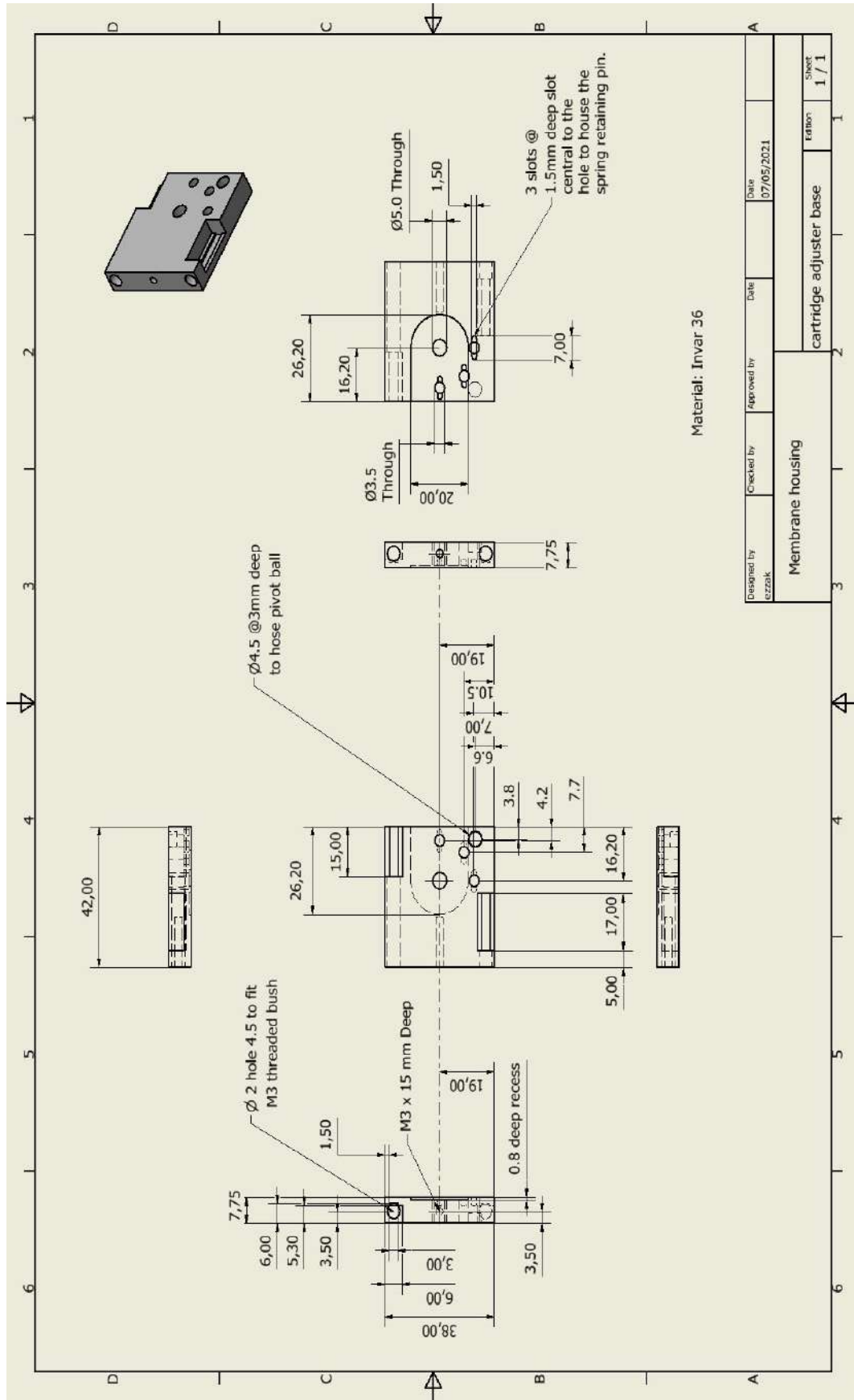
The ability to forecast the results of transmitting a noisy signal through a linear system is a key application of the power spectral density.

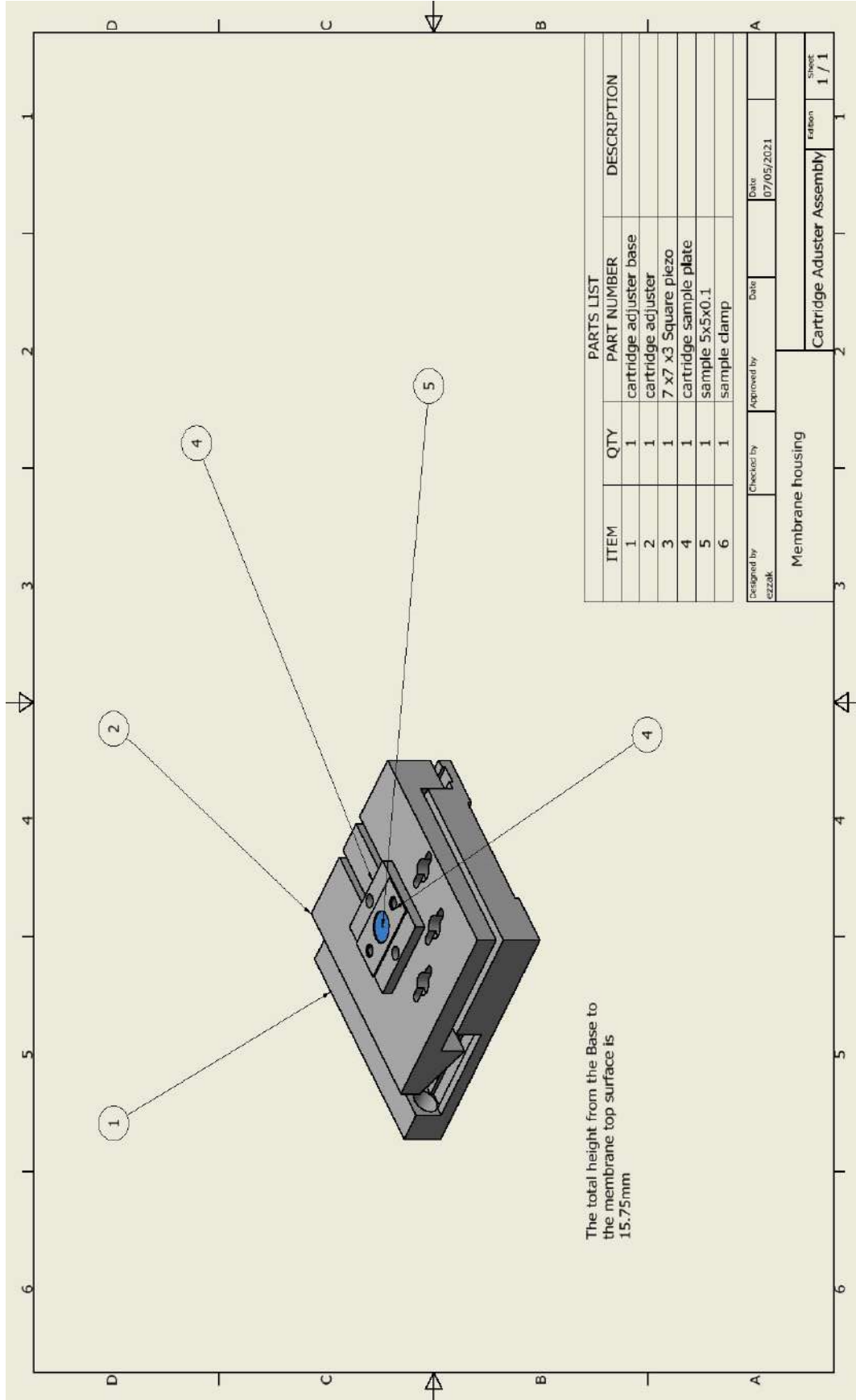
Appendix B

Assembly Drawing of the Membrane Holder







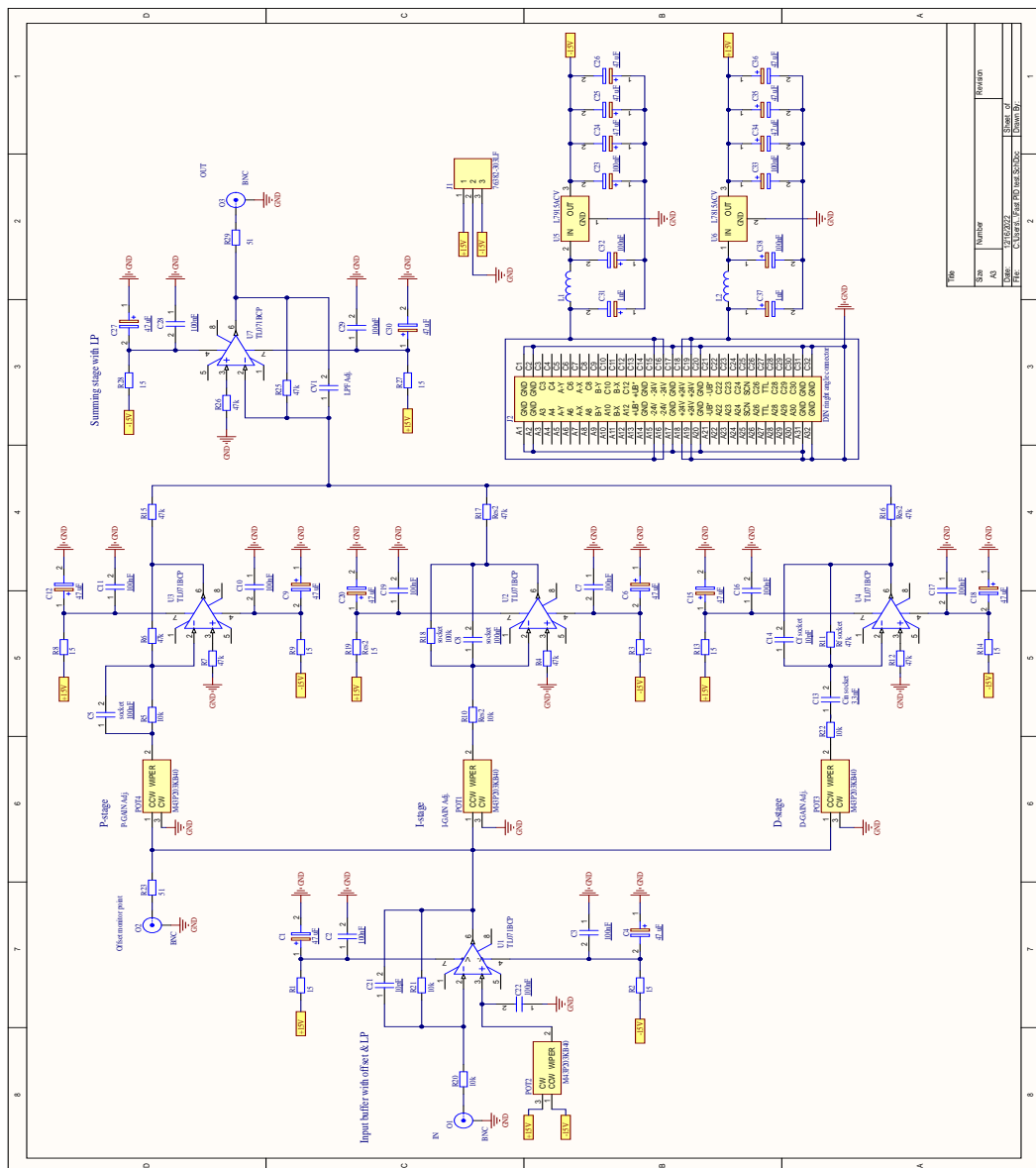


PARTS LIST			
ITEM	QTY	PART NUMBER	DESCRIPTION
1	1	cartridge adjuster base	
2	1	cartridge adjuster	
3	1	7 x7 x3 Square piezo	
4	1	cartridge sample plate	
5	1	sample 5x5x0.1	
6	1	sample clamp	

Designed by czzak	Checked by	Approved by	Date
			07/05/2021
Membrane housing		Cartridge Adjuster Assembly	
		Revision	Sheet
			1 / 1

Appendix C

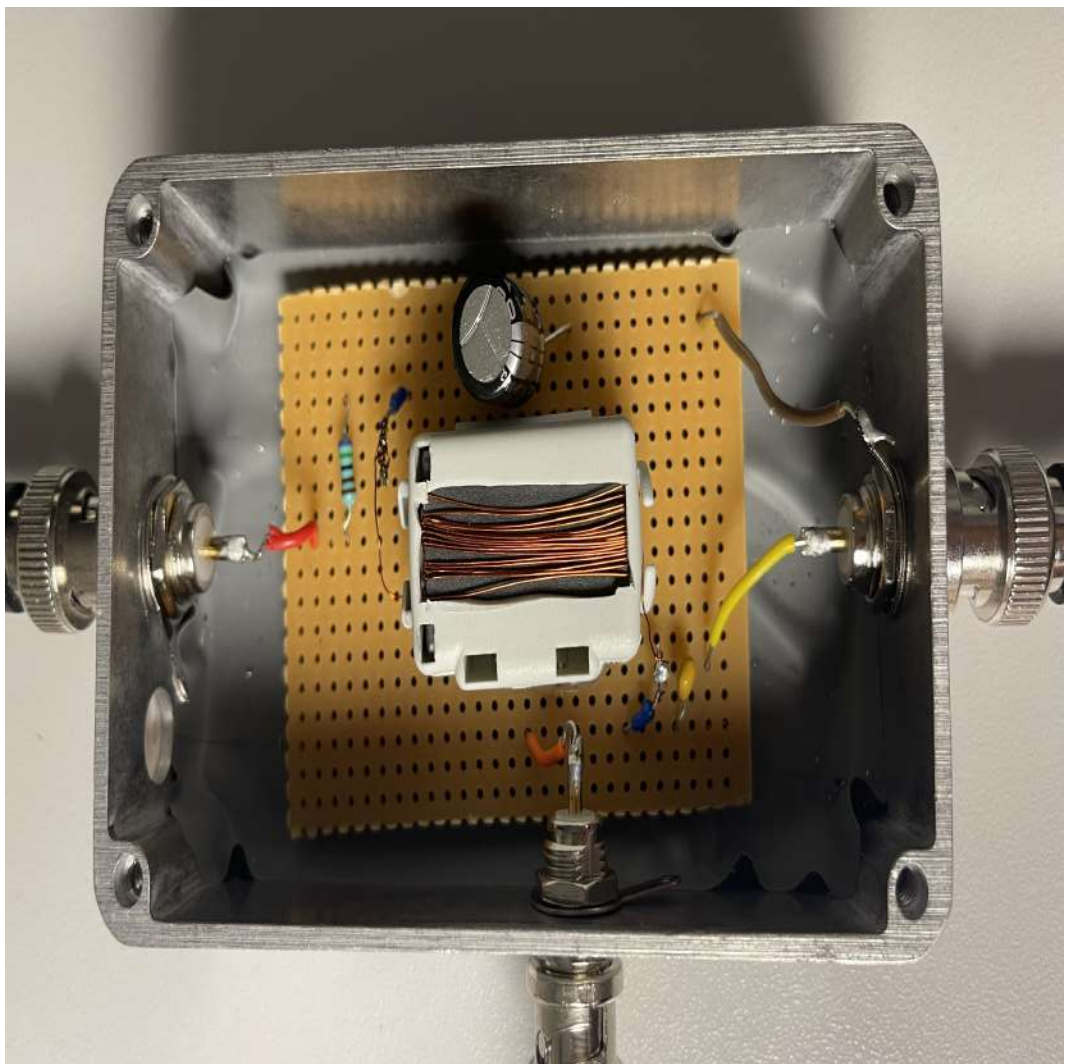
Schematic Of Fast PID Card



Appendix D

Electronic circuits

D.1 Bias-T



D.2 Low Pass Filter

